

Statistical Modelling and Performance Evaluation of TOA for Localization inside the Human Body using Computational Techniques

A Thesis submitted to the Faculty of
WORCESTER POLYTECHNIC INSTITUTE
in partial fulfillment of the requirements for the degree of
Doctorate of Philosophy
in
Electrical and Computer Engineering
By



Umair I. Khan

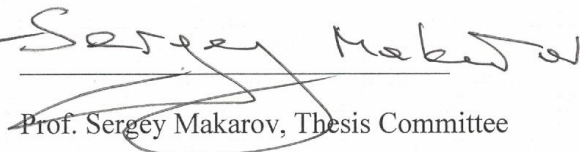
(uikhan@wpi.edu)

April 2018

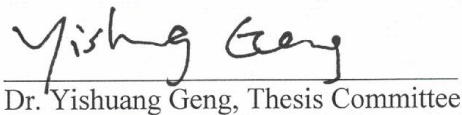
APPROVED:



Prof. Kaveh Pahlavan, Thesis Advisor



Prof. Sergey Makarov, Thesis Committee



Dr. Yishuang Geng, Thesis Committee



Prof. John McNeil, Department Head

Abstract

Localization inside the human body using radio frequency (RF) transmission is gaining importance in a number of applications such as Wireless Video Capsule Endoscopy. The accuracy of RF localization depends on the technology adopted for this purpose. The two most common RF localization technologies use received signal strength (RSS) and time-of-arrival (TOA). This research presents a comparison of the accuracy of TOA and RSS based localization inside human tissue using computational techniques for simulation of radio propagation inside human tissues. Computer simulation of the propagation of radio waves inside the human body is extremely challenging and computationally intensive. We designed a basic, MATLAB coded, finite difference time-domain (FDTD) for the radio propagation in and around the human body and compared the results obtained from this software with the commonly used and commercially available Finite Element Method (FEM) modeling in ANSYS HFSS. We first show that the FDTD analysis yields comparable results. Then we use the software to simulate the RSS and TOA of the wideband signals propagated inside the human body for RF localization to compare the accuracies of the two methods. We then develop a statistical TOA model using empirical data gathered from these simulations; and, in conjunction with pre-established mathematical models for RSS, we compare the accuracy of each technique with the Cramer-Rao Lower Bound (CRLB) commonly used for calculation of bounds for the performance of localization techniques and the effects of human body movements.

Table of Contents

Abstract	2
Table of Contents	3
List of Figures	5
Glossary	7
Acknowledgements	8
Chapter 1: Introduction	9
1.1 Background of Research	9
1.2 Motivation of the Research	15
1.3 Contributions of the Thesis	20
1.4 Summary of Chapters in this Thesis:	21
Chapter 2: Body Area Networks and Localization	22
2.1 Challenges in localization techniques	22
2.2 Earlier work in Body Area Network channel modeling	34
2.2.1 Antenna Effect	35
2.2.2 Electrical Properties of Body Tissues	36
2.2.3 Shadowing	36
2.2.4 Power Delay Profile	36
2.2.5 Model Summary	37
2.2.6 Channel Implementation	39
2.2.7 Evaluation Procedure:	40
2.3 Analytical Techniques used in literature	41
2.3.1 Applications for Analytical Techniques	41
2.3.2 Performance Evaluation Methodology	44
2.3.3 Results and Discussions	47
Chapter 3: Computational Techniques for Radio Propagation Inside the Human Body ..	53
3.1 Analysis of Path-Loss Models	53
3.1.1 Circuit Model of Path-loss	54
3.1.2 Transfer Functions in Frequency Domain	55
3.1.3 Transfer Functions in Time Domain	57
3.1.4 Comparison Between FDTD and FEM in Free Space	59
3.1.5 Comparison between FDTD and FEM for Human Body Model	61
3.1.6 Preliminary Results	63
Chapter 4: Wideband Characteristics of Radio Propagation Inside the Human Body	65
4.1 Simulation of Wideband Characteristics using ANSYS HFSS	68
4.1.1 An Overview of ANSYS HFSS	69
4.1.2 Experimental Procedure using the ANSYS HFSS suite	70
4.2 Comparison of TOA and RSS for Localization inside the Body	73
4.2.1 Comparison between TOA Results and Published Path-Loss Models	76
4.2.1 CRLB and Ranging Accuracy of TOA vs. RSS	78
4.2.3 Sources of Error in Localization	81
Chapter 5: Precision of EM Simulation based Wireless Location Estimation in Multi-Sensor Capsule Endoscopy	83
5.1 Functionality and Assessment Approach	84
5.1.1 Functionality Assessment Setup	84

5.1.2 TOA Model for the Digestive System	86
5.1.3 Unpredictability of Impulse Time Arrival	88
5.2 TOA Simulations and Observations	88
5.3 CRB for TOA Based Spatial Endoscopy Pill Positioning	93
5.3.1 CRB for Multi-sensor Collaborative Positioning	93
5.3.2 CRB for TOA Positioning with Sensor with Highest RSS (Path of Least Resistance)	97
Chapter 6: Conclusions and Future Work.....	105
References.....	108
Appendix 1: MATLAB Code for FDTD in XZ Plane.....	117
Appendix 2: MATLAB Code for FDTD in YZ Plane.....	122

List of Figures

Figure 1: Two-dimensional traverse magnetic to Z-field	28
Figure 2: Scatter grids for TM to Z mode.....	30
Figure 3: Parameters involved in wideband TOA measurement using arrival of the first path directly connecting the transmitter and the receiver.	33
Figure 4: The UDP multipath condition from results of Ray tracing simulation and a channel profile with 200MHz	34
Figure 5: Human Body Model with (a) Map of Digestive System, and (b) Side View of External Sensor Array.....	44
Figure 6: Human Organs.....	47
Figure 7: Geometrical Distribution of Location Error in Stomach.....	49
Figure 8: Geometrical Distribution of Location Error in Small Intestine.....	50
Figure 9: CDF of location error in stomach, small intestine and large intestine	51
Figure 10: Circuit model of antenna-to-antenna TX/RX link.....	55
Figure 11: Network transformations of the antenna-to-antenna link; a) original TX/RX network; b) microwave impedance matrix approach; and c) equivalent T-network of lumped impedances.....	56
Figure 12: FDTD port model corresponding to the excitation source in Figure 10.	58
Figure 13: Top: FDTD simulations of the dipole-to-dipole link in free space; Bottom: corresponding ANSYS HFSS simulations with resulting impedance matrix. The transition region of the FDTD solution is clearly seen; it averages about 4 ns	60
Figure 14: Antenna locations positioned around the human body. The antenna separation distance is fixed at 41.3cm. Top: FEM ANSYS mesh; Bottom: FDTD mesh; simulation results corresponding to the first case, and electric field distributions. The electric field is	63
Figure 15: Measurement setup (a) without body (b) with body	66
Figure 16: Impulse response obtained from measurements with human subjects of different weights	66
Figure 17: Channel impulse response in four different orientations of the body at Ultra Wideband (UWB) Frequencies – (a) LOS – Body-to-Body, (b) NLOS – Body-to-Body	67
Figure 18: ANSYS HFSS TM simulation setup (a) without body (b) with body and electric field plot. The two horizontal black lines represent the dipoles	72
Figure 19: Impulse response obtained from the two simulated and measured channels ..	72
Figure 20: Left: Map of where the sensors were placed; Right: Transmitted (top) and received (bottom) voltages vs. time	75
Figure 21: Received pulse (V) with transmitter and receiver sensors at positions d and e respectively	76
Figure 22: Time of Arrival vs. distance for various sensor positions.....	77
Figure 23: Plot obtained from the path-loss model in [57].....	77
Figure 24: Distance Measurement Error from TOA for each sensor position.....	78
Figure 25: RSS vs. Distance plot for each sensor position.....	80
Figure 26: Distance Measurement Error from RSS for each sensor position.....	81
Figure 27: Change in distance of two sensors due to the movement of the body.....	82
Figure 28 An illustration of the human digestive system – the typical path of an endoscopy pill	85

Figure 29 Positions of one internal and one external sensor as seen from (a) slightly turned outside the body (b) side of the stomach and intestines (c) slightly turned stomach and intestine 86

Figure 30 External Sensor Distribution (note: an equal number of sensors would be placed on the opposite side of the model)..... 87

Figure 31 An example of surface-surface communication 87

Figure 32 Impulse response between pill inside intestine and sensor on the surface of the belly..... 90

Figure 33 Impulse response between pill inside intestine and sensor on the back 90

Figure 34 Time of Arrival vs. distance for various sensor positions 91

Figure 35 Distance Measurement Error from TOA for each sensor position..... 92

Figure 36 PDF of the Distance Measurement Error from TOA for each sensor position 92

Figure 37 RSS vs. Distance plot for each sensor position 98

Figure 38 Distance Measurement Error from RSS for each sensor position 99

Figure 39 PDF of the Absolute Values of Distance Measurement Error from RSS for each sensor position 100

Glossary

ALPS	Adaptive Lanczos-Pade Sweep
AP	Access Point
BAN	Body Area Networks
BPSK	Binary Phase Shift Keying
CDF	Cumulative Distribution Function
DOA	Direction of Arrival
EOTD	Enhanced Observed Time Difference
FDTD	Finite Difference Time Domain
FEM	Finite Element Method
GPS	Global Positioning System
ITS	International Telecommunication Standard
KVL	Kirchhoff's Voltage Law
LOS	Line of Sight
MIMO	Multiple Input Multiple Output
MICS	Medical Implant Communication Service
MoM	Method of Moments
NIST	National Institute of Standards and Technology
NLOS	Non-Line of Sight
OLOS	Obstructed Line of Sight
PML	Perfectly Matched Layer
POA	Phase of Arrival
RMS	Root Mean Square
RSS	Received Signal Strength
RT	Ray Tracing
SAR	Specific Absorption Rate
TOA	Time of Arrival
UDP	Undetected Direct Path
UWB	Ultra Wideband
VNA	Vector Network Analyzer
WCE	Wireless Capsule Endoscopy

Acknowledgements

I would like to express my profound gratitude to my thesis advisor, Dr. Kaveh Pahlavan, and co-advisor, Dr. Sergey Makarov; whose continuous guidance, support and wisdom helped me focus and attain the objectives of this research.

I would specifically like to thank Dr. Allen Levesque for his valuable time and comments on my research.

I would also like to thank my former lab peers, Ferit Akgul, Yunxing Ye, Yi Wang, Ruijun Fu, Yishuang Geng, Kaveh Ghaboosi and M. Monirul Islam for providing continuous guidance and support over the course of the research. They also motivated me towards achieving my research goals by maintaining a healthy learning environment in the CWINS lab.

In addition, I would like to thank my former roommates Saad Ahmad and Kashif Azeem and my colleagues at Intel Thomas MacDonald, John Critchlow, Timothy Wig, Christiaan Bil, and Vishnu Gunasekaran, for the intellectual, thought provoking and often challenging conversations about our respective research areas.

I would like to dedicate this work to my mother, Salma Khan, my father, and my siblings whose prayers, love and support was the ultimate motivation during my academics. I would also like to dedicate this work to my wife, Ain-ul-Aisha, as without her technical and moral support, I would never have been able to finish my PhD while working full time at Intel. For that, and for so many reasons, I will forever be thankful for her partnership.

Finally, but foremost, I am always indebted to God, for keeping me in a state of wellbeing and for helping me attain all the knowledge and appreciation throughout my studies.

Chapter 1: Introduction

The effective design, assessment, and installation of a radio network require accurate characterization of the channel. The channel characteristics vary from one environment to another, and the particular characteristics determine the feasibility of using a proposed communication technique in a given operating environment [1]. Having an accurate channel characterization for each frequency band, including key parameters and a detailed mathematical model of the channel, enables the designer or user of a wireless system to predict signal coverage, achievable data rate, accuracy of localization techniques and the specific performance attributes of alternative signaling and reception schemes from wireless access and localization. Channel models are also used to determine the optimum location for installation of antennas and to analyze interference between different systems.

1.1 Background of Research

Body Area Networks (BAN) are defined to consist of a set of portable sensors that communicate wirelessly with each other. These sensors are either worn on, or implanted in, the human body to monitor essential parameters or movements of the body. Since the human body is non-homogenous in nature, there will be a lot of reflection, refraction and diffraction of rays traveling through it. This will cause the waveform to take many different paths from the transmitter to the receiver, a scenario already observed in indoor localization. The unpredictability of existing paths between transmitter and receiver in an

indoor environment is very similar to the situation with outdoor channels, and in fact the work that has been done in characterization of mobile radio channels offers a useful guideline for modeling indoor channels. In an indoor environment, the multipath is caused by reflection from the walls, ceiling, floor, and objects within an office; in outdoor radio channels, multipath is caused by reflections from the ground as well as the buildings and vehicles in the vicinity of the mobile terminal.

There are two basic approaches to simulating wideband radio propagation characteristics: (1) measurement-based statistical modeling and (2) direct analytical solution of the radio propagation equations (computational techniques). Measurement-based statistical models are based on a mathematical description using several parameters. The parameter values are evaluated for each individual measurement of the wideband channel characteristics, and the statistics of the parameters over a large database are used to complete the model for a given coverage area. Statistics gathered from measurements in typical areas are extended to develop a more generalized model for all coverage areas. Statistical models generally do not incorporate details of the buildings in an outdoor coverage area or the layout of rooms within a building. Instead they classify all areas into a limited number of broadly designated environments and all buildings into a few classes of buildings.

In modem performance evaluations, the system designer is usually concerned with the overall performance over typical areas or typical buildings, and statistical models usually serve the purpose reasonably well. In other applications such as microcellular or indoor installations, where proper siting of antennas is an important issue, building-specific

radio propagation models offer a more precise tool for determining optimum antenna locations. Building-specific radio propagation models are based on direct solution of the radio propagation equations with boundaries defined by a map of a coverage area or the layout plan of a building. The technique known as *ray tracing* provides a simple approximation for analysis of radio wave propagation. Another approach is numerical solution of the Maxwell equations using the *finite-difference time-domain* (FDTD) technique. Ray tracing algorithms are also very useful for analysis of the angle of arrival of the paths for MIMO applications and the Time of Arrival (TOA) of the direct Line of Sight (LOS) path needed for the popular TOA based geolocation systems.

To compare the results of various computer simulation techniques, several approaches might be adopted. The most obvious approach is to compare the measured and simulated channel responses in typical locations. This method is not well suited for the evaluation of statistical models, because statistical models do not relate the channel response to a specific location. However, for assessing building-specific radio propagation models, this method is very useful. Another approach to evaluating the results of a simulation method is to compare empirical data with the cumulative distribution functions (CDFs) of the rms delay spread and multipath power produced by the simulation. Yet another approach for comparing radio propagation models is to evaluate the performance of a particular modem over the measured and modeled channels. Standard modulation techniques such as Binary Phase Shift Keying (BPSK) and wideband techniques such as direct-sequence spread-spectrum or non-spread signaling with adaptive equalization can be used as benchmarks in these evaluation approaches [2], [3], [4].

The 2D ray tracing simulation technique was originally developed to analyze the behavior of wireless channels in small indoor areas using the two dimensional reflection and transmission model to trace rays by means of the ray shooting technique [1], [5]. This model offered a low-cost means of propagation analysis for small indoor areas used for wireless local area network (WLAN) applications. Diffraction did not play a major role in most indoor radio propagation scenarios since the diffraction effect would influence propagation significantly only in locations such as corridors when the LOS path is blocked and the received signal involves multiple reflections and transmissions. However, this is not a likely situation for indoor WLAN applications, where terminals are typically used in reasonably open work areas.

Later, a 3D ray tracing simulation based on a typical residential area was developed to again analyze the behavior of wireless channel in macrocellular high-rise urban canyons with antennas installed above roof level [6]. This simulation was based on the model that reflections and sharp edge diffraction were the main mechanism for simulation of signal propagation.

Although ray-tracing models can efficiently predict radio propagation characteristics for indoor and outdoor applications, these techniques are only approximations to the direct solution of electromagnetic wave propagation equations. The ideal method of simulating radio propagation is to solve Maxwell's equations numerically. The numerical solution of

these differential equations over a designated area requires selection of a number of points at which the solution is to be determined iteratively.

The FDTD method is probably the most straightforward and widely used method for numerical solution of Maxwell's equations. With this method, Maxwell's equations are approximated by a set of finite-difference equations. By placing the electric and magnetic fields on a staggered grid and defining appropriate initial conditions, the FDTD algorithm employs the central differences to approximate both spatial and temporal derivatives, and it solves Maxwell's equations directly. The distribution of electric and magnetic fields over the whole grid is calculated incrementally in time; and when the simulation is finished, the propagation characteristics are known at every location in the area under study.

A more computationally efficient form of traditional FDTD method (for communication applications) has also been applied previously to indoor areas, showing significant improvement in accuracy over the rectangular FDTD algorithm. The computational time needed for this method was comparable to that of a three-dimensional ray-tracing algorithm. A point-to-point comparison between predicted and measured power in all locations for two-dimensional and three-dimensional ray-tracing and for the FDTD models showed that both ray-tracing models and the FDTD model were all in good agreement with the measurements. However, ray-tracing provides a more accurate estimate of the power based on the standard deviation calculated against the measurements [1].

In general, the indoor localization problem is considered a challenging and difficult problem to formulate and model due mainly to the ever-changing characteristics of the wireless channel [1]. Results of a multitude of research studies have reported that time-of-arrival (TOA)-based techniques exhibit superior performance in line-of-sight (LOS) conditions when compared with received signal strength (RSS) and Direction-of-arrival (DOA) techniques [1]. This is due to the fact that location bearing metrics obtained from LOS measurement are more accurate than RSS and DOA metrics. The TOA of the direct path can then be related to the separation of the antenna pair. In 2-D scenarios three accurate distance measurements from known reference points (RPs) are enough to precisely determine the location of the mobile terminal.

However, the accuracy of the TOA-based technique degrades drastically when LOS conditions are not met [1], as confirmed in various measurement campaigns [1]. In such scenarios, mitigation of the ranging error plays a vital role in improving the accuracy of the system. This necessitates the use of modeling and estimation of ranging error in non-line-of-sight (NLOS) conditions. The first natural solution is the use of existing multipath models developed for telecommunication applications. However, these multipath models are based mainly on the delay spread of the channel and have not paid specific attention to the arrival time of the direct path. In all these models the first path is assumed to be the direct path. This assumption neglects the existence of the Undetected Direct Path conditions, which are one of the major causes of unpredicted large errors in TOA-based positioning systems; we will discuss this in greater detail in the next section.

1.2 Motivation of the Research

Measurement and modeling of radio propagation for high speed wireless communications and localization is a challenging field of science and engineering. This is due to the fact that the radio channel suffers from temporal, spatial and direction of arrival fading caused by very complex random variations of the multipath components carrying radio signal from one location to another.

The human body channel suffers from severe multipath propagation and heavy shadow fading conditions so that measurements for localization are far from accurate in many instances. Previous literature on BAN like [14] have mainly concentrated on narrowband measurements and simulations for RSS for communication applications that can also be used for localization applications; hence there was a need to explore the possibility to use TOA ranging techniques for the human body channel. TOA and RSS estimation are therefore susceptible to large errors due to undesirable multipath conditions. To accurately estimate TOA in indoor areas, we need to resort to different frequencies of operation and more complex signaling formats and signal processing techniques that can resolve the problems. The behavior of a TOA sensor in human body multipath propagation is highly sensitive to the bandwidth of the sensor [15].

In practice, bandwidth is limited, and the received signal comprise a number of peaks whose amplitudes and arrival times are the same as pulses but they look more like a continuous waveform. The superposition of all these pulse shapes forms the received signal, which we refer to as the channel profile. A common practice is to estimate the

location of the direct path (DP) as the location of the peak of the first path that is the estimated TOA. In a single path environment, the actual expected and the estimated direct paths are the same. In multipath conditions, however, the peak of the channel profile gets shifted from the expected TOA, resulting in a TOA estimation error caused by the multipath condition. We refer to the distance error caused by erroneous estimate of the TOA as the *distance measurement error*. For a given multipath condition we expect that as we increase the bandwidth the distance measurement error becomes smaller. [16]

Lately, wireless capsule endoscopy (WCE) has garnered plenty of interest owing to its non-intrusive characteristic. Assessment of the gastro-intestinal (GI) region is essential to recognize any colorectal cancer inside the digestive system tract. It has been discovered that colorectal cancer is the second foremost source of cancer associated fatalities in the United States. Additionally, WCE permits the doctor to depict the whole GI region exclusive of scope trauma and air insufflations. Conventional practices like gastroscopy and colonoscopy can barely get to the first couple of or final few feet of the GI region. The WCE obtained its endorsement from the U.S. Food and Drug Administration (FDA) in 2001, and in excess of 200,000 patients have taken advantage of the benefits of this innovative skill. WCE begins with the subject ingesting the pill. The normal motion of muscles transports the pill effortlessly and simply all through the GI tract, which is sending out color picture taken by the camera in the pill as it goes through. The process is mobile, permitting the subjects to carry on with their everyday activity all through the endoscopic assessment. In spite of the benefits WCE has, it is reported that a doctor takes a couple hours to review the snapshots taken through every WCE assessment, given that roughly fifty thousand pictures are taken throughout the eight hour timeframe of the test

[65], [66]. This reduces the speed of this method of assessment and makes the process considerably more expensive. Besides, after the assessment by WCE, the doctor might have a desire to re-examine a location of concern for additional analysis or management. Precise position data of the pill can assist in both quickening up the review of the snapshots and supporting the doctor for eventual treatment.

A variety of methods for positioning of the pill have been researched in viability analyses. The initial plan was to employ a spatial examining scheme to establish the position of the points with the highest received signal strength (RSS). This method is unmarketable and unmanageable. Frisch et al. [67],[68] examined a wireless triangulation scheme by means of an exterior antenna arrangement that gauges the signal power of the pill's communications at several positions and applies this data to approximate the space between the pill and external sensors. The mean investigational inaccuracy is described to be 37.7 mm [69], [90]. A technique put forth by Kuth et al. [70], [91] to estimate the location and direction of the pill using X-ray emission photography. The method results in the pill to be seen explicitly because it possesses a number of energy impervious features that are typically made of metal or synthetic material and exhibit a an extremely distinct photograph. Hence, it is conceivable to function with a very little amount of energy helping in decreasing medical hazards on the subjects. Another process was suggested by Kawasaki [71] to pinpoint the position of biological implants by means of TOA established waveform recovery technique. Initially, the transmission velocity of the waveform propagating in the patient's body is approximated by collecting the photographs from CAT or MRI machines. After that, a dynamic pattern fusion technique

is used to compute the transmission period established by the result of the comparator in the middle of the Tx and the Rx. Additional methods established for the positioning of camera pills comprise magnetic field detection [72], [92]. A tiny permanent magnet is encased into the pill. With the detection information of a magnetic antenna arrangement on the exterior the subject's body, the 3D positioning and 2D direction of the pill are approximated. Accelerometer based techniques have also been employed in camera pill positioning [73], [93]. In this research, a 39.3 mm electronic inertial meter with three axes, operating at 20 Hz, was inserted inside the pill and information was propagated using Zigbee protocol to an outside workstation. Because the inertia is quantitatively obtained, velocity can be calculated more precisely than location as it needs only one integral solution. Therefore, classifying the actual position of each image obtained from the pill is important in both analytic and remedial purposes of pill based endoscopy.

Out of these methodologies, RSS based positioning techniques have the benefit of versatility and a comparatively small price of execution. Consequently, it has been selected to be employed for the Smartpill device [74], [94] in USA and the M2A device [75], [95] in Israel. Usually, wireless positioning methods use results obtained from TOA, angle of arrival (AOA) or RSS experiments. Even though, the RSS method is less sensitive to a restricted frequency spectrum and inhospitable wireless channels, a commonly acknowledged advantage of the TOA method is better precision relative to the RSS and AOA methods. Nonetheless, the high refractive index of the body results in sizable inaccuracies in TOA approximation and the restricted frequency band (402–405 MHz) of Medical Implant Communication Services (MICS) makes it difficult to perform precise TOA measurements. This issue is worsened by the motion of the GI tract, and the

drainage and replenishing sequence, resultant in irregular errors in distance measurements [76], [96]. Hence, the location data from TOA approximation is not optimal in the existing literature; and this paper attempts to remedy this problem.

There are essentially two methods to employ TOA data for positioning, triangulation and waveform identification. In this study, we limit our focus on the problems concerned with TOA triangulation methods. The TOA Triangulation method is derived from the impulse response model from organs containing the devices to the exterior of the body. The technique is employed to compute the space between every surface antenna and the pill. After that, at least four of the measured distances are employed to compute the position of the pill in 3D space.

The most difficult issue in the positioning of the pill arises from the complicated nature of the surroundings of the pill as it goes down the human body. Because the GI tract is of an extended cylindrical formation that doubles up on its own at multiple instances and has the freedom to shift inside the abdomen, it is very challenging to precisely determine the position of the pill. Adding to that, because of the subject moving about and resting activities like breathing, the actual position of the antennas on the exterior of the patient and their comparative location to the pill within the GI tract keeps changing, deeming the meaning of positioning dissimilar from conventional definitions. At present, the majority of studies have concentrated on coming up with algorithms and mathematical models to find the solution of the triangulation issue [3.11]. In this paper, we take a separate route. Basing our approach on the statistical medical device impulse response model derived in

[77] and [97], we concentrate on the precision of pills traveling inside the body using TOA based triangulation methods; Ye et al. have derived the positioning bound computation for a solitary capsule scenario in [60],[100]. The Cramer-Rao bounds (CRB) developed in this study measure the restrictions of positioning precision with multiple external sensor protocol, medical device impulse response method and multiple capsules inside the body. Our end goal is to investigate the precision attainable at different tissues and decide whether this precision is sufficient for WCE. Related papers have been published for indoor personnel localization [79], [100] and robot positioning [80], [101].

1.3 Contributions of the Thesis

The two most common RF localization technologies use received signal strength (RSS) and time-of-arrival (TOA). This research presents a comparison of the accuracy of TOA and RSS based localization inside human tissue using computational techniques for simulation of radio propagation inside human tissues. Computer simulation of the propagation of radio waves inside the human body is extremely challenging and computationally intensive. We designed a basic, MATLAB coded, finite difference time-domain (FDTD) [59] for the radio propagation in and around the human body and compared the results obtained from this software with the commonly used and commercially available Finite Element Method (FEM) modeling in ANSYS HFSS. We first show that the FDTD analysis yields comparable results. Then we use the software to simulate the RSS and TOA of the wideband signals (shown in Figure 20) [60] propagated inside the human body for RF localization to compare the accuracies of the two methods. The accuracy of each technique is compared with the Cramer-Rao Lower Bound (CRLB)

[61] commonly used for calculation of bounds for the performance of localization techniques and the effects of human body movements.

1.4 Summary of Chapters in this Thesis:

In Chapter 2, we first present reasons why localization can be challenging and what solutions have been used in the past to counter these challenges. We also discuss previous work done on BAN modeling and analysis. In Chapter 3, we introduce computational techniques used to simulate wireless channels and present simulations and results used for path-loss modeling in and around the human body. In Chapter 4, we use the software to simulate the RSS and TOA of the wideband signals propagated inside the human body for RF localization to compare the accuracies of the two methods. The accuracy of each technique is compared with the Cramer-Rao Lower Bound (CRLB). The last chapter presents the conclusions of this research.

Chapter 2: Body Area Networks and Localization

Body Area Networks (BAN) are defined to consist of a set of portable sensors that communicate wirelessly with each other. These sensors are either worn on, or implanted in, the human body to monitor essential parameters or movements of the body.

Localization is defined to be the process of accurately pin-pointing the position of an electronic object in a given area. Since conventional methods used in outdoor positioning cannot be used for indoor geo-location or localization in the human body, they are treated as separate areas of interest.

2.1 Challenges in localization techniques

Real-time locating is affected by a variety of errors. The major reasons physical and may not be reduced by improving the technical equipment. The only solution is for the mathematical intelligence to improve.

Despite advertisement with several vendors, RTLS has a very mundane requirement: RTLS requires direct and clear wireless visibility. Where there is no visibility on the path from mobile tags to resident nodes there will be no result or a non valid result from locating engine. This applies to satellite locating as to terrestrial locating. RTLS was invented, to provide an escape, when roofs do not allow the passage of satellite signals. The quality of wireless visibility, however, is much more tolerant than optical visibility, but it still remains a direct viewing quality. All measured, but deviated paths deliver false distances.

The measured location may appear entirely faulty. This is a generally result of simple operational models to compensate for the plurality of error sources. It proves impossible to serve proper location after ignoring the errors.

Real time is no registered branding and has no inherent quality. A variety of offers sails under this term. As motion causes location changes, inevitably the latency time to compute a new location may be dominant with regard to motion. Either an RTLS system that requires waiting for new results is not worth the money or the operational concept that asks for faster location updates does not comply with the chosen systems approach.

Location will never be reported *exactly*, as the term *real-time* and the term *precision* directly contradict in aspects of measurement theory as well as the term *precision* and the term *cost* contradict in aspects of economy. That is no exclusion of precision, but the limitations with higher speed are inevitable.

Recognizing a reported location steadily apart from physical presence generally indicates the problem of insufficient over-determination and missing of visibility along at least one link from resident anchors to mobile transponders. Such effect is caused also by insufficient concepts to compensate for calibration needs.

Noise from various sources has an erratic influence on stability of results. The aim to provide a steady appearance increases the latency contradicting to real time requirements.

As objects containing mass have limitations to jump, such effects are mostly beyond physical reality. Jumps of reported location not visible with the object itself generally

indicate improper modeling with the location engine. Such effect is caused by changing dominance of various secondary responses.

Location of residing objects gets reported moving, as soon as the measures taken are biased by secondary path reflections with increasing weight over time. Such effect is caused by simple averaging and the effect indicates insufficient discrimination of first echoes.

In statistical measurement and modeling of the radio propagation, the radio channel between a wireless transmitter and receiver can be described by

$$h(d, t, \beta, \phi, \tau, \theta) = \sum_{i=1}^L \beta_i^d(t) e^{j\phi_i^d(t)} \delta[\tau - \tau_i^d(t)] \delta[\theta - \theta_i^d(t)] \quad (2.1)$$

where $h(d, t, \beta, \phi, \tau, \theta)$ is the overall channel impulse response at time t between the transmitter and receiver, which are at distance d from one another; and β, ϕ, τ , and θ are the amplitude, phase, delay of arrival, and angle of arrival of multiple arrivals paths of the transmitted signal. Since in wireless applications either terminal can be mobile or people may move around or between transmitter and receiver, these paths and the channel impulse response are also function of time and space. Using (1.1), the average received power for a given distance between the transmitter and the receiver corresponds to [1]:

$$P_d = \sum_{i=1}^L \overline{|\beta_i^d(t)|^2} \quad (2.2)$$

Here, the received signal power is the sum of squares of all path amplitudes. In the case of narrowband signaling [1],

$$P_d = \left| \sum_{i=1}^L \beta_i^d(t) e^{j\theta_i^d(t)} \right|^2 \quad (2.3)$$

where the amplitudes added vectorially and the overall power was the square of the resulting vector. As a result, the normalized received power of a narrowband signal is less than or equal to that of a wideband signal.

To calculate the distance between the transmitter and the receiver, we use the average RSS and a distance-power relationship to determine d' . If we define the distance measurement error as the difference between the measured and actual values of distance, $\varepsilon_d = d' - d$, this error in RSS systems would be independent of the bandwidth of the system. The power is calculated by a common principle behind all statistical models for the calculation of RSS that corresponds to:

$$RSS_d = 10 \log_{10} P_r = 10 \log_{10} P_t - 10\alpha \log_{10} d + X \quad (2.4)$$

In this model, called the lognormal model, P_t is the transmitted power, d is the distance between the transmitter and the receiver, and α is the distance-power gradient of the environment. The random variable X is a lognormal distributed random variable representing shadowing effects.

In the case of propagation around a human body, environmental variations and body movements will cause path loss to be different from the mean value for a given distance.

This phenomenon is called shadowing, and it represents the path loss variation around the mean.

In TOA systems, TOA measurement requires more complex receivers, and measurement accuracy depends on system bandwidth. A TOA sensor estimates the distance from $d'_w = c\tau_{1,w}$, where c is the speed of light and $\tau_{1,w}$ is an estimate of the TOA of the direct path. Estimates of TOA are obtained by detecting the first peak of the received signal, and this value is a function of bandwidth and the occurrence of UDP conditions. The distance error is defined as

$$\varepsilon_{d,w} = d'_w - d \quad (2.5)$$

where d is the actual distance between the sensor and target object. This model uses the results of measurement-calibrated ray-tracing software to develop a statistical model for the distance measurement error and to relate that to the bandwidth of the sensor.

For communication applications, we need a convenient numerical measure of the time dispersion or multipath delay spread of the channel. A popular measure of delay spread is the root mean square (rms) delay spread, τ_{rms} , which is the second central moment of the channel impulse response. It is given mathematically by

$$\tau_{rms} = \sqrt{\overline{\tau^2} - (\overline{\tau})^2} \quad (2.6)$$

where, given L propagation paths,

$$\frac{1}{\tau^n} = \frac{\sum_{i=1}^L \tau_i^n |\beta_i|^2}{\sum_{i=1}^L |\beta_i|^2} \quad (2.7)$$

These equations are the basis of delay spread calculations for the current 2D and 3D RT applications, discussed in later sections.

In 1966 Yee [31] proposed a technique to solve Maxwell's curl equations using the finite-difference time-domain (FDTD) technique. Yee's method has been used to solve numerous scattering problems for microwave circuits, dielectrics, and electromagnetic absorption in biological tissue at microwave frequencies. Since it is a time-domain method, solutions can cover a wide frequency range with a single simulation run. The FDTD method belongs to the general class of grid-based differential time-domain numerical modeling methods. The time-dependent Maxwell's equations are discretized using central-difference approximations to the space and time partial derivatives. The resulting finite-difference equations are solved in either software or hardware in a leapfrog manner: the electric field vector components in a volume of space are solved at a given instant in time; then the magnetic field vector components in the same spatial volume are solved at the next instant in time; and the process is repeated over and over again until the desired transient or steady-state electromagnetic field behavior is fully evolved.

Let us consider a two-dimensional *transverse magnetic* (TM)-to-z field (Electric and Magnetic fields are perpendicular to the Z-axis) as depicted in Figure 1. This figure presents a classic scattering/radiation problem where both the radiating and receiving

antennas (dipole or monopole) are vertical. The TM to z field can be illustrated by Maxwell's equations, (2.8-2.10):

$$\frac{\partial E_z}{\partial t} = \frac{1}{\epsilon} \frac{\partial H_y}{\partial x} - \frac{1}{\epsilon} \frac{\partial H_x}{\partial y} - \frac{\sigma}{\epsilon} E_z \quad (2.8)$$

$$\frac{\partial H_x}{\partial t} = -\frac{1}{\mu} \frac{\partial E_z}{\partial y} - \frac{\sigma^*}{\mu} H_x \quad (2.9)$$

$$\frac{\partial H_y}{\partial t} = \frac{1}{\mu} \frac{\partial E_z}{\partial x} - \frac{\sigma^*}{\mu} H_y \quad (2.10)$$

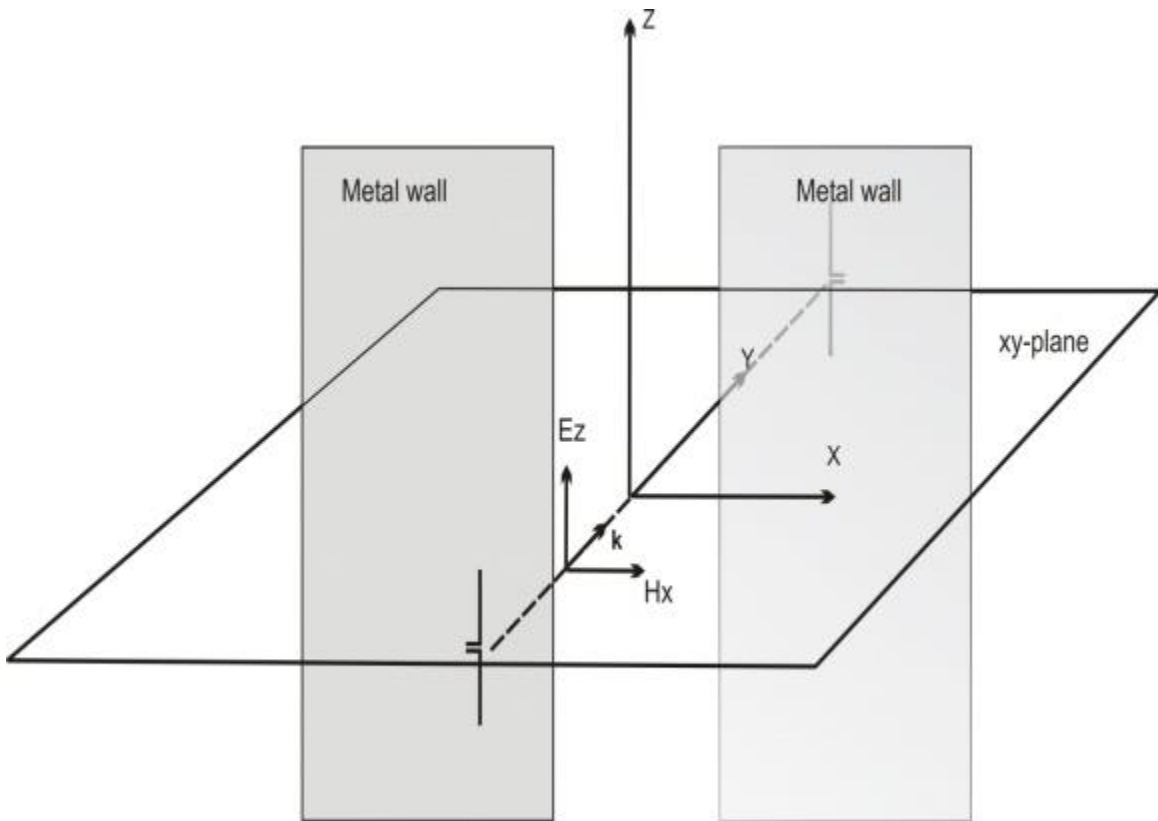


Figure 1: Two-dimensional traverse magnetic to Z-field

Here E and H are electric and magnetic fields, respectively; σ and σ^* are the electric and magnetic conductivities (losses), real or artificial. The standard Yee 2-2 FDTD scheme represented in (2.11) can be implemented [31] to operate on a staggered grid that is shown in Figure 2. In (2.11), E and H are discretized in time and space as the initial excitation travels through the computational area.

$$\begin{aligned}
E_z(t, z) &\rightarrow E_z((n-1) \cdot \Delta t, (k-1) \cdot \Delta x, (m-1) \cdot \Delta y) = E_{zk,m}^n \\
H_x(t, z) &\rightarrow H_x\left(\left(n - \frac{1}{2}\right) \cdot \Delta t, (k-1) \cdot \Delta x, \left(m - \frac{1}{2}\right) \cdot \Delta y\right) = H_{xk,m+1/2}^{n+1/2} \\
H_y(t, z) &\rightarrow H_y\left(\left(n - \frac{1}{2}\right) \cdot \Delta t, \left(k - \frac{1}{2}\right) \cdot \Delta x, (m-1) \cdot \Delta y\right) = H_{yk+1/2,m}^{n+1/2} \\
n &= 1, 2, \dots, N_t - 1 \quad k = 1, 2, \dots, N_x + 1 \quad m = 1, 2, \dots, N_y + 1
\end{aligned} \tag{2.11}$$

$$\frac{E_{zk,m}^{n+1} - E_{zk,m}^n}{\Delta t} = \frac{1}{\varepsilon_{k,m}} \frac{H_{yk+1/2,m}^{n+1/2} - H_{yk-1/2,m}^{n+1/2}}{\Delta x} - \frac{1}{\varepsilon_{k,m}} \frac{H_{xk,m+1/2}^{n+1/2} - H_{xk,m-1/2}^{n+1/2}}{\Delta y} - \frac{\sigma}{2\varepsilon_{k,m}} (E_{zk,m}^{n+1} + E_{zk,m}^n) \tag{2.12}$$

$$\frac{H_{xk,m+1/2}^{n+3/2} - H_{xk,m+1/2}^{n+1/2}}{\Delta t} = -\frac{1}{\mu_{k,m+1/2}} \frac{E_{zk,m+1}^{n+1} - E_{zk,m}^{n+1}}{\Delta y} - \frac{\sigma^*}{2\mu_{k,m+1/2}} (H_{xk,m+1/2}^{n+3/2} + H_{xk,m+1/2}^{n+1/2}) \tag{2.13}$$

$$\frac{H_{yk+1/2,m}^{n+3/2} - H_{yk+1/2,m}^{n+1/2}}{\Delta t} = +\frac{1}{\mu_{k+1/2,m}} \frac{E_{zk+1,m}^{n+1} - E_{zk,m}^{n+1}}{\Delta x} - \frac{\sigma^*}{2\mu_{k+1/2,m}} (H_{yk+1/2,m}^{n+3/2} + H_{yk+1/2,m}^{n+1/2}) \tag{2.14}$$

In (2.11), n represents the imaginary layer number that is calculated in the time domain and shown in Figure 5.9 as layer 0 and 1 (layers of electrical fields separated by Δt). The middle layer is represented as imaginary layer ($n = 0.5$). On the other hand, m and k represent the position of electrical or magnetic fields along the x or y axis of any of

imaginary time domain layers. For example, $(k = 1)$ represents the position of the second electrical field on $(n = 0)$ layer from the t axis and $(k = 0.5)$ represents the position of the first magnetic field on the $(n = 0.5)$ layer from the t axis. Substitution of (2.11) into the fundamental Maxwell equations that are shown in (2.8-2.10) results in discrete formulas of (2.12-2.14).

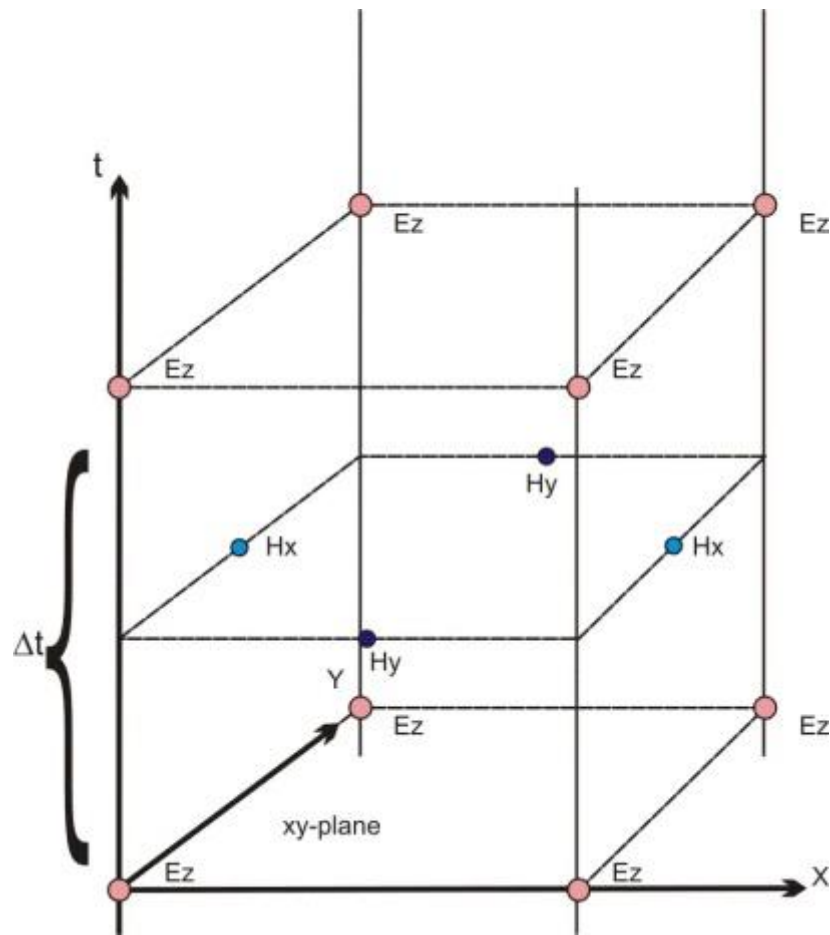


Figure 2: Scatter grids for TM to Z mode

Formulas given in (2.12-2.14) are basically the core engine of any FDTD simulation software. Once we initialize the emanating electric and magnetic fields with the appropriate excitation values, a recursive call to these formulas, in time-domain, will predict electric and magnetic fields at any point within our computation space. From (2.12-2.14) we can clearly see that a 2D version of such a simulation would only calculate electric and magnetic fields for two specific dimensions. To better understand a 2D FDTD simulation, one can visualize the simulation space as an imaginary plane. We can calculate fields, in time-domain, for any points located on this plane from the time an excitation emanates from the transmitter until it impinges upon the edges of the plane and the receiver point.

The indoor radio channel suffers from severe multipath propagation and heavy shadow fading conditions so that measurements for localization are far from accurate in many instances. In general, measurements of Phase of Arrival (POA) and DOA in large indoor and urban areas provide very unreliable measurements. TOA and RSS estimation are also susceptible to large errors due to undesirable multipath conditions. To accurately estimate TOA in indoor areas, we need to resort to different frequencies of operation and more complex signaling formats and signal processing techniques that can resolve the problems. The behavior of a TOA sensor in indoor multipath propagation is highly sensitive to the bandwidth of the sensor. The UWB systems, which exploit bandwidths in excess of 1GHz, have attracted considerable attentions as a means of measuring accurate TOA for indoor geolocation applications. However, as in other TOA systems, UWB

systems cannot completely avoid UDP problems. Figure 3 shows the basic concepts involved in wideband TOA measurements using the arrival time of the first path in a typical indoor multipath environment. In this figure, the direct path (DP) is represented by the first path, which is also the strongest path. Location of this path is the expected value of the TOA. Other paths with a number of reflections and transitions arrive after the DP with lower amplitudes. These paths would have been observed at the receiver if the bandwidth of the system were infinite. In practice, bandwidth is limited, and the received signal comprise a number of pulses whose amplitudes and arrival times are the same as impulses but they are shaped pulse. The superposition of all these pulse shapes forms the received signal, which we refer to as the channel profile. A common practice is to estimate the location of the DP as the location of the peak of the first path that, is the estimated TOA. In a single path environment, the actual expected and the estimated direct paths are the same. In multipath conditions, however, as shown in Figure 3, the peak of the channel profile gets shifted from the expected TOA, resulting in a TOA estimation error caused by the multipath condition. We refer to the distance error caused by erroneous estimate of the TOA as the *distance measurement error*, which can be calculated using $\varepsilon_{d,w} = \hat{d}_w - d$. For a given multipath condition we expect that as we increase the bandwidth the distance measurement error becomes smaller.

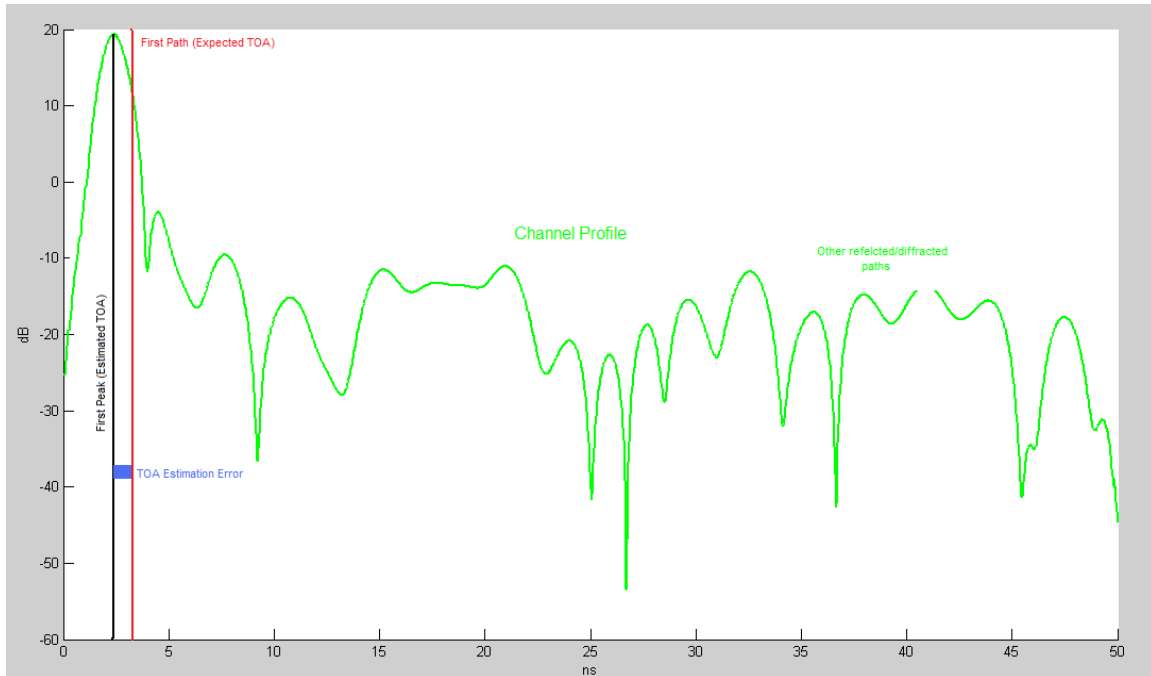


Figure 3: Parameters involved in wideband TOA measurement using arrival of the first path directly connecting the transmitter and the receiver.

As a mobile terminal moves away from a base station the strength of the DP and the total received signal power decay exponentially. In an OLOS environment when the DP falls below the threshold while other paths are still detectable, the receiver assumes the first path in the profile to be the DP. This mis-identification causes a substantial error in wideband TOA measurements. We refer to this situation the UDP condition **0**. Figure 4 depicts the occurrence of the UDP scenario using the results of ray-tracing for a transmitted pulse with a bandwidth of 1.2 GHz. Since the difference between the strength of the strongest path and the first path is more than the dynamic range (the range of detectable signal level below the strongest path) of the receiver, we have a clear UDP condition in which the first path is detected and declared as the DP resulting in a 3 cm distance measurement error. With the release of UWB bands, the main challenge for the implementation of accurate wideband TOA systems is to find a remedy for UDP conditions.

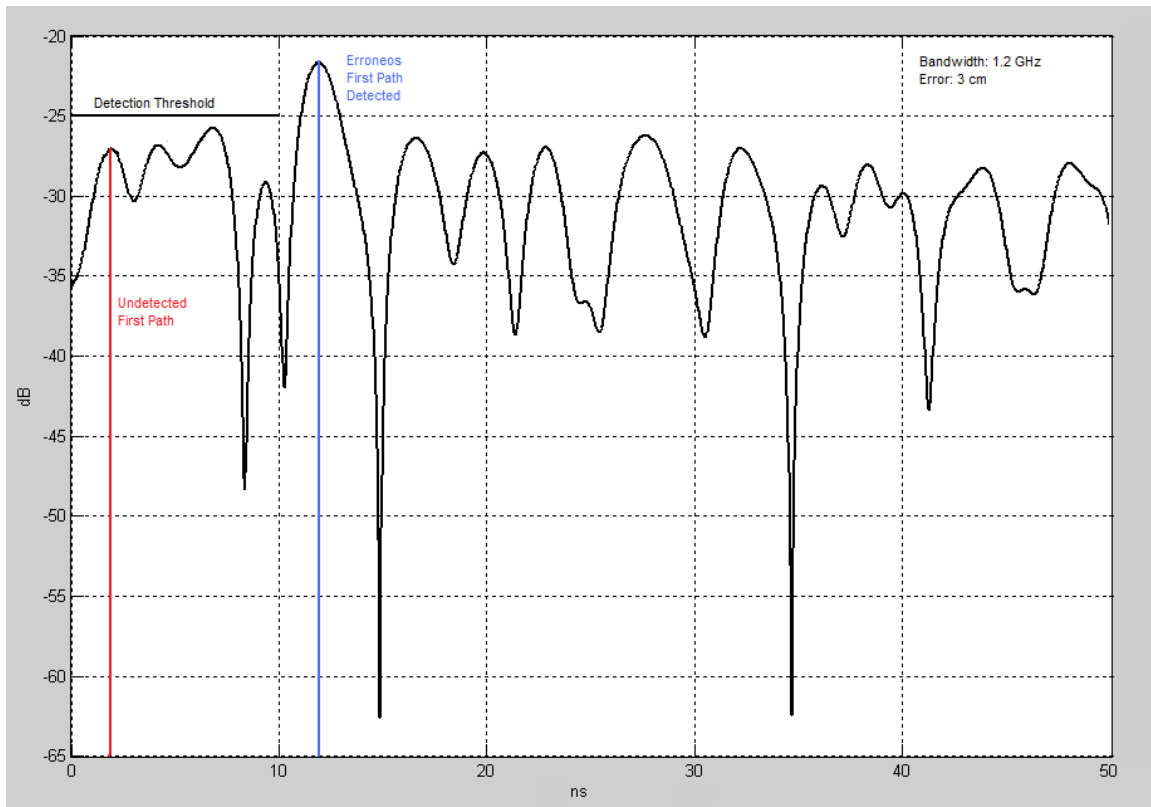


Figure 4: The UDP multipath condition from results of Ray tracing simulation and a channel profile with 200MHz

2.2 Earlier work in Body Area Network channel modeling

Body Area Networks (BAN) are defined to consist of a set of portable sensors that communicate wirelessly with each other. These sensors are either worn on, or implanted in, the human body to monitor essential parameters or movements of the body.

There are several channel models available for BAN communication. This research would work mostly on the ideas put forward by Kamyazandoost and Kamran Sayrafian-Pour in their paper [39]. This paper presented a detailed evaluation of all the factors that might affect communication between the BAN nodes. Some of them are described below:

2.2.1 Antenna Effect

An antenna placed on the surface or inside a body will be heavily influenced by its surroundings. The consequent changes in antenna pattern and other characteristics need to be understood and accounted for during any propagation measurement campaign. The form factor of an antenna will be highly dependent on the requirements of the application. For Medical Implant Communication Service (MICS) applications, for example, a circular antenna may be suitable for a pacemaker implant, while a helix antenna may be required for a stent or urinary implant. The form factor will affect the performance of the antenna and, the antenna performance will be very important to the overall system performance. Therefore, an antenna which has been designed with respect to the body tissues (or considered the effect of human body) shall be used for the channel model measurements. [39]

The BAN antennas may be classified into two main groups:

- **Electrical antennas, such as dipole:** Electrical antenna typically generates large components of E-field normal to the tissue interface, which overheat the fat tissue. This is because boundary conditions require the normal E-field at the interface to be discontinuous by the ratio of the permittivities, and since fat has a lower permittivity than muscle, the E-field in the fat tissue is higher.
- **Magnetic antennas, such as loop:** Magnetic antenna produces an E-field mostly tangential to the tissue interface, which seem not to couple as strongly to the body as electrical antennas. Therefore, it does not overheat the fat.

There are antennas same as helical-coil, which is similar to a magnetic antenna in some respect, but its heating characteristics appear to be more like an electrical antenna. The strong E-field generated between the turns of coil is mainly responsible for tissue heating.

It should be noted that the specific absorption rate (SAR) in the near field of the transmitting antenna depends mainly on the H-field; however, SAR in the far field of the transmitting antenna depends mainly on the E-field.

2.2.2 Electrical Properties of Body Tissues

The human body is not an ideal medium for radio frequency wave transmission. It is partially conductive and consists of materials of different dielectric constants, thickness, and characteristic impedance. Therefore depending on the frequency of operation, the human body can lead to high losses caused by power absorption, central frequency shift, and radiation pattern destruction. The absorption effects vary in magnitude with both frequency of applied field and the characteristics of the tissue.

2.2.3 Shadowing

Due to the variation in the environment surrounding of body or even movement of the body parts, path loss will be different from the mean value for a given distance. This phenomenon is called shadowing, and it reflects the path loss variation around the mean. The shadowing should be considered for stationary and non-stationary position of body.

2.2.4 Power Delay Profile

Because of multipath reflections, the channel response of a BAN channel looks like a series of pulses. In practice the number of pulses that can be distinguished is very large,

and depends on the time resolution of the measurement system. The power delay profile of the channel is an average power of the signal as a function of the delay with respect to the first arrival path.

There are several channel models available for body area networks, but the most popular one is also described in Yazandoost and Sayrafian-Pour's paper. The following is a brief summary of their modeling procedures. Note that their paper used Ultra Wideband (UWB) as their air interface while this research will use ZigBee for the same purpose.

2.2.5 Model Summary

Due to the extreme close range and the fact that the antennas are worn on the body, the BAN channel model has different path loss, amplitude distribution, clustering, and inter-arrival time characteristics compared with the other application scenarios within the 802.15.4a context. Analysis of the electromagnetic field near the body using a finite difference time domain (FDTD) simulator indicated that in the 2-6 GHz range, no energy is penetrating through the body. Rather, pulses transmitted from an antenna diffract around the body and can reflect off of arms and shoulders. Thus, distances between the transmitter and receiver in our path loss model are defined as the distance *around* the perimeter of the body, rather than the straight-line distance *through* the body. In addition, the path loss mechanisms near the body are probably dominated by energy absorption from human tissue which results in an exponential decay of power versus distance. The amplitude distributions measured near the body are also different from traditional communication environments. Since there were only a small number of multipath components that we could not resolve in our measurement, traditional Rayleigh and

Ricean models are not justified and showed a very poor fit. Rather, the lognormal distribution was clearly superior. While the Nakagami-distribution proposed for 802.15.4a can well-approximate lognormal distributions under some limited circumstances, this was not the case for the lognormal distributions observed near the body. In addition, the uncorrelated scattering assumption assumed in other models is violated for systems where both the transmitter and receiver are placed on the same body. This is not at all surprising since the multi-path components have overlapping path trajectories especially in the vicinity of the transmitter and receiver, all multipath component path lengths are very short, and there is a natural symmetry of the body. Their measurements indicate that there are always two clusters of multi path components due to the initial wave diffracting around the body, and a reflection off of the ground. Thus, the number of clusters is always two and does not need to be defined as a stochastic process as in the other scenarios. Furthermore, the inter-cluster arrival time is also deterministic and depending on the exact position of the transmitters on the body. To simplify this, we have assumed a fixed average inter-cluster arrival time depending on the specified scenario. The very short transmission distances result in small inter-ray arrival times within a cluster which are difficult to estimate without a very fine measurement resolution. Furthermore, we could not confirm if the Poisson model proposed here is valid for use around the body. Thus, these parameters are not included in our model. Finally, the extracted channel parameters depended on the position of the receiver on the body. To incorporate this effect easily without having to perform a large number of simulations, only three scenarios are defined corresponding to a receiver placed on the ‘front’, ‘side’, and ‘back’ of the body. In conclusion, the recommended a body area

channel model for comparing system performance for BAN scenarios consisting of the following features:

- Exponential path loss around the body
- Correlated log normal amplitude distributions
- A fixed two-cluster model
- Fixed inter-cluster arrival time
- Fixed inter-ray arrival time
- Three scenarios corresponding to the front, side and back of the body [39]

2.2.6 Channel Implementation

Implementing this model on a computer involves generating N correlated lognormal variables representing the N different bins, and then applying an appropriate path loss based on the distance between the antennas around the body. This can be accomplished by generating N correlated normal variables, adding the pathloss, and then converting from a dB to linear scale as follows:

$$Y_{dB} = \mathbf{X} \cdot chol(\mathbf{C}) - \mathbf{M} - P_{dB}/2 \quad (2.15)$$

\mathbf{X} is a vector of N uncorrelated unit mean, unit variance, normal variables that can be generated easily in MATLAB. To introduce the appropriate variances and cross-correlation coefficients, this vector is multiplied by the upper triangular Cholesky factorization of the desired covariance matrix \mathbf{C} . Cholesky factorization functions are provided by MATLAB and most mathematical software packages. The means (a vector \mathbf{M}) of each different bin and the large scale path loss (P_{dB}) are subtracted. The resulting vector Y_{dB} now consists of N correlated normal variables. This can be converted into the

desired N correlated lognormal variables easily by transforming Y_{dB} into the linear domain. The path loss can be calculated according to the following formula:

$$P_{dB} = \gamma(d - d_0) + P_{0,dB} \quad (2.16)$$

γ is in units of dB/meter, d is the distance between antennas, d_0 is the reference distance, and P_0 is the power at the reference distance.

2.2.7 Evaluation Procedure:

To minimize the amount of simulations that need to be performed in comparing system proposals, a simplified BAN evaluation procedure was agreed upon by the channel sub-group.

Rather than evaluating the system at all of the different distances, typical transmission distances corresponding to the ‘front’, ‘side’, and ‘back’ scenarios are generated using a uniform distribution. These distances were extracted from the body used in the simulator and are summarized below:

- Front: 0.04 – 0.17 m
- Side: 0.17 – 0.38 m
- Back: 0.38 – 0.64 m

Analysis of the cluster due to the ground reflection indicated that its amplitude depended on the type of floor material. Rather than simulating for each material individually, typical floor materials (corresponding to metal, concrete, and average ground) are generated at random with equal probability in evaluating systems.

2.3 Analytical Techniques used in literature

The Center for Wireless Information Network Studies (CWINS) at Worcester Polytechnic Institute (WPI) has written a paper on the performance bounds for RF positioning of Endoscopy Camera Capsules. In their paper, they evaluated the factors affecting the accuracy achievable in localization of a wireless endoscopy capsule as it passes through the digestive system of the human body. Using a three-dimension full electromagnetic wave simulation model, we obtain bounds on the capsule location estimation errors when the capsule is in each of three individual organs: stomach, small intestine and large intestine. The simulations assume two different external sensor arrays topologies. They compared these performance bounds and draw the conclusion that location-estimation errors are different for different organs and for various topologies of the external sensor arrays. In this section we talk about the details of performance bounds for RF localization.

2.3.1 Applications for Analytical Techniques

Recently, Wireless Capsule Endoscopy (WCE) has become the preferred method for diagnosis of the human gastrointestinal (GI) tract. The technique is non-invasive and more precise, portable and personal as compared with traditional scope-based endoscopy [1]. The Given Imaging company (first commercial producer of camera pills) announced in May 2009 that over 1 million of their PillCam capsules have been used clinically. Capsule Localization plays a crucial role in the process of diagnosis and follow up

interventions since doctors need to know the position and orientation of the capsule when images are collected. Various technologies for localization of the capsule have been explored in feasibility studies, including ultrasound [31], magnetic tracking [32], RF signal triangulation or fingerprinting [33], [34] and computer vision [35]. Among these technologies, RF signal based localization systems have the advantage of application-non-specific, relatively inexpensive hardware implementation. Therefore, it has been chosen for use with the Smartpill capsule [36] in the USA and the M2A capsule [37] in Israel as the technique for localization. RF capsule localization systems usually use an external sensor array (which can be fixed on a special jacket) that measures the RF signal metrics of capsule transmissions at multiple points and uses this information to estimate the distance or uses fingerprinting algorithms to estimate the location of the capsule [38].

The RF localization technique based on time or angle measurement methods, i.e., Time of Arrival (TOA), Time Difference of Arrival (TDOA) and Angle of Arrival (AOA) are not feasible. The strong absorption of human tissue causes large ranging errors and the limited bandwidth (402-405MHz) of the Medical Implant Communication Services (MICS) band make high resolution TOA estimation difficult. The problem is made even worse by the gastrointestinal movement, and the filling and emptying cycle, resulting in unpredictable ranging error [39]. Thus the Received Signal Strength (RSS) based method is more suitable for capsule localization. The RSS based method is less sensitive to the bandwidth limitation and performs consistently when a line of sight transmission path is not available. There are basically two ways to use the RSS information at an external sensor array for localization, triangulation and fingerprinting. Triangulation is based on the path loss model from body surface to the implant-site tissues. The model is used to

calculate the distance between each reference point (external sensor) and the capsule, then to triangulate the location of the capsule.

The Fingerprinting method is based on the assumption that the strongest signal is received by the closest reference point and that approximately equal strength signals in two adjacent reference points result from capsule locations, which are between the adjacent reference points. This is similar to an algorithm used in indoor localization [40].

Currently, most of the researches on RSS based capsule localization has focused on developing the algorithms and mathematical models for solving the triangulation problem [33], [34]. However, in our investigations, we have not found research work in the literature on accuracy limits for RSS based capsule localization. In this paper, we take a different approach. Based on the statistical implant path loss model developed in [41], we focus on calculating the localization bounds for a capsule in the GI tract using the RF triangulation method. We evaluate the factors affecting localization accuracy, namely, reference-points topology and implant path loss model parameters in different organs and tissues throughout the digestive tract. Then we calculate the localization bounds in different organs with various topologies of the external sensor array. Our aim is to discover the localization accuracy achievable at various organs and how the topology of the external sensor array influences this accuracy.

2.3.2 Performance Evaluation Methodology

In order to evaluate the localization bound for endoscopic wireless capsule as it travels through the human digestive system, as show in fig 1(a), we use the three dimensional full-wave electromagnetic field simulation system. The 3D human body model has a spatial resolution of 2 millimeters and includes frequency dependent dielectric properties of 300+ parts in a male human body.

When a capsule is swallowed, it goes through the mouth, esophagus, stomach, small intestine, large intestine and anus. We can obtain the exact coordinates of these organs from this simulation system. Fig 1(b) shows the side view of the external sensor array.

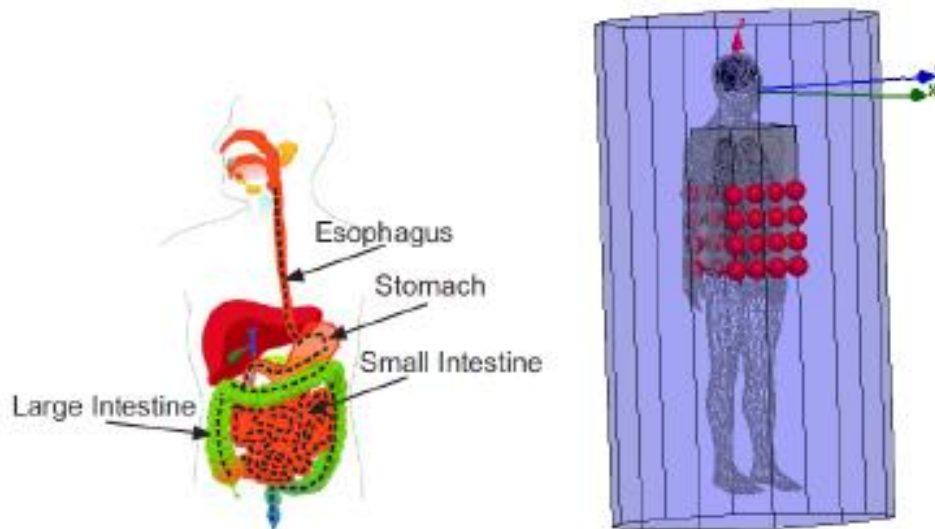


Figure 5: Human Body Model with (a) Map of Digestive System, and (b) Side View of External Sensor Array

In order to investigate the limit for RSS based capsule localization, we need to know the path loss model for the body area network system. The path loss model is not simple for BAN because of the complexity of the human tissue structure and body shape. BAN for medical and nonmedical devices that could be placed inside or on the body surface are considered in [42]. Some studies of the channel between the sensor nodes in the human body are based on FDTD numerical analysis methods, which have been used often in the investigation of the UWB channel close to the human body [43].

If the signal propagates in free space, the path loss model in dB between the transmitter and the receiver is related only to the distance d , and this relationship is given by [42],

$$PL(d) = PL_0 + 10n\log(d/d_0) \quad (2.17)$$

where PL_0 is the path loss at a reference distance r_0 . The parameter, n is the path loss exponent value, indicating the rate at which the path loss increases as distance d increases. The variation in the environment surrounding the body, or even movement of the body parts, will impact the received signal strength and this phenomenon is called shadowing. Thus, there is a random variable S to be added in Equation 1 and the resulting statistical implant path loss is given by [42],

$$PL(d) = PL_0 + 10n\log(d/d_0) + S \quad (2.18)$$

where S is the random variable around the mean and represents deviation caused by shadowing phenomenon.

As noted earlier, the Federal Communication Commission (FCC) has allocated the frequencies in the 402-405MHz range to be used for MICS. At 402-405MH, there are two scenarios based on location of the communicating nodes, implant to implant, called

CM1, and implant to body surface, called CM2 [42]. Different models and scenarios in body area networks have different parameters.

All parameters of the CM2 scenario are shown in Table I [42].

TABLE 2.1: MODEL OF IMPLANT TO BODY SURFACE CM2 FOR 402-405MHZ

Implant to Body Surface	$PL(d_0)(dB)$	α	$\sigma_s(dB)$
Deep Tissue	47.14	4.26	7.85
Near Surface	49.81	4.22	6.81

Because we assume the capsule travels in the digestive system of the human body, the parameters shown as Deep Tissue in this table correspond to our simulation.

In order to investigate the achievable accuracy limits for RSS based capsule localization, we need to determine the relationship between the error in signal strength estimation and the error in estimating the capsule position using our localization method. This relationship in two dimensions has already been derived in [44]. Here we derive the relationship in three dimensions between the error in signal strength and error in capsule localization by extending the result obtained for two dimensions.

If we assume that the signal strength estimation error has zero mean and variance σ_p^2 , and these errors for different Access Points (APs) are independent of each other, the covariance matrix of the location error estimate is given by

$$\text{cov}(d\hat{r}) = \sigma_p^2 (H' H)^{-1} = \begin{bmatrix} \sigma_x^2 & \sigma_{xy}^2 & \sigma_{xz}^2 \\ \sigma_{yx}^2 & \sigma_y^2 & \sigma_{yz}^2 \\ \sigma_{zx}^2 & \sigma_{zy}^2 & \sigma_z^2 \end{bmatrix} \quad (2.19)$$

where

$$H = \begin{bmatrix} \frac{-10\alpha_1}{\ln 10} \frac{x-x_1}{r_1^2} & \frac{-10\alpha_1}{\ln 10} \frac{y-y_1}{r_1^2} & \frac{-10\alpha_1}{\ln 10} \frac{z-z_1}{r_1^2} \\ \vdots & \vdots & \vdots \\ \frac{-10\alpha_N}{\ln 10} \frac{x-x_N}{r_N^2} & \frac{-10\alpha_N}{\ln 10} \frac{y-y_N}{r_N^2} & \frac{-10\alpha_N}{\ln 10} \frac{z-z_N}{r_N^2} \end{bmatrix} \quad (2.20)$$

where $(x_i; y_i; z_i)$ is the coordinate of the i -th sensor; α_i is the exponent value of path loss for the signal coming from the i -th sensor; $r_i = \sqrt{(x - x_i)^2 + (y - y_i)^2 + (z - z_i)^2}$ is the distance between the capsule inside the body and the i -th sensor; and N is the number of sensors.

The standard deviation of location error is estimated as

$$\sigma_r = \sqrt{\sigma_x^2 + \sigma_y^2 + \sigma_z^2} \quad (2.21)$$

Where, $\sigma_x, \sigma_y, \sigma_z$ represent the standard deviation of location errors in X,Y,Z direction, respectively.

2.3.3 Results and Discussions

The simulations of deviation of location error are carried out in three main organs of digestive system, which are stomach, small intestine and large intestine, as shown in Figures 2(a), 2(b) and 2(c).

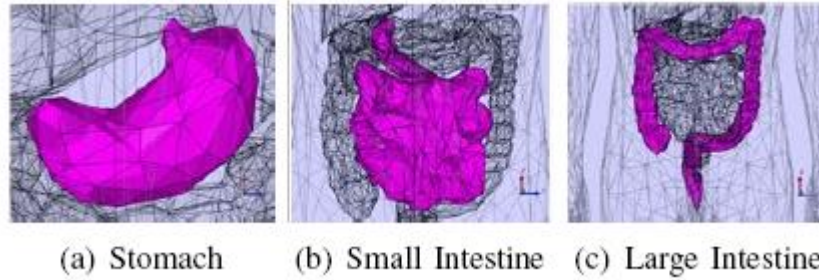
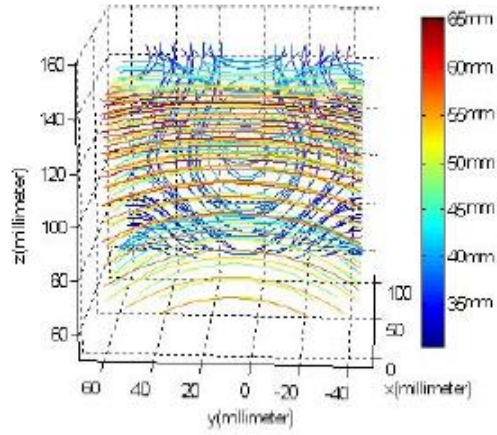


Figure 6: Primary organs of the human digestive system

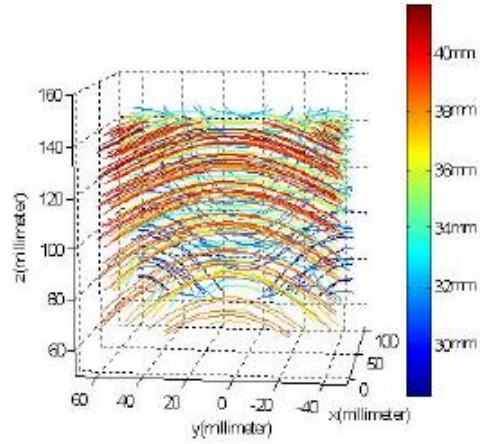
The ranges of stomach, small intestine and large intestine in x, y, z dimensions are 109x106x80 millimeters, 70x170x231 millimeters, and 136x239x358 millimeters, respectively. We calculate the deviation of location error every 5 millimeters in these organs and the parameters in our simulation are as follows: $\alpha = 4.26$ and $\sigma_s(dB) = 7.85$

Figures 3(a) and 3(b) show the contours of σ_r^2 of the stomach in three dimensions when one and two 4x4 sensor arrays are deployed, respectively. A line of a given color in the figure represents the same value in location error. The location error in the stomach is up to 65 millimeters when there is one 4x4 array and up to 42 millimeters when there are two 4x4 sensor arrays.

Figures 7(a) and 7(b) show the contours of σ_r^2 of the small intestine in three dimensions when one and two 4x4 sensor arrays are deployed, respectively. The location error in the small intestine is up to 52 millimeters when there is one 4x4 sensor array available; however the error is about 40 millimeters when there are two 4x4 sensor arrays available.

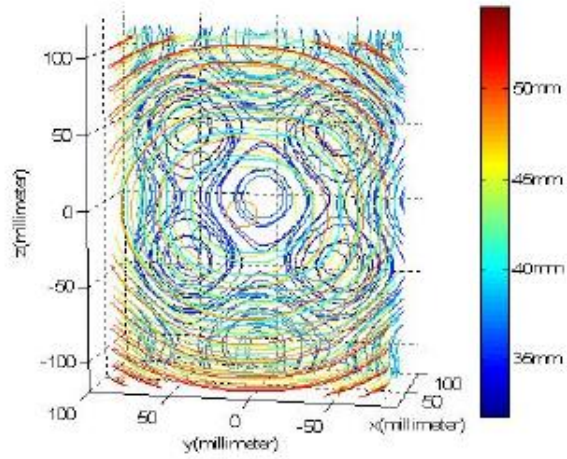


(a) One Sensor Array

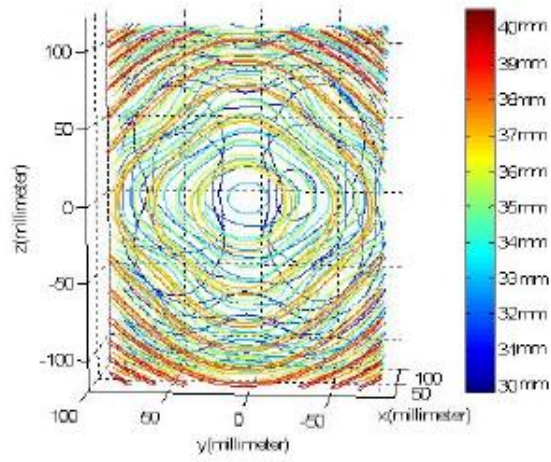


(b) Two Sensor Array

Figure 7: Geometrical Distribution of Location Error in Stomach



(a) One Sensor Array



(b) Two Sensor Array

Figure 8: Geometrical Distribution of Location Error in Small Intestine

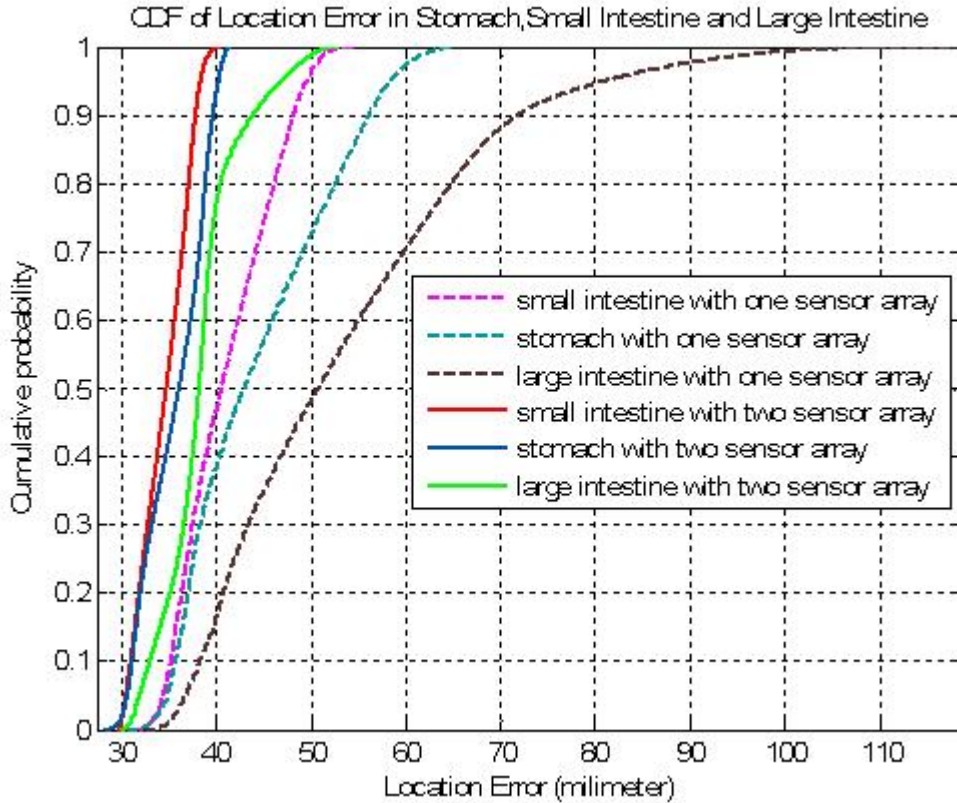


Figure 9: CDF of location error in stomach, small intestine and large intestine

Figure 9 shows the CDF distribution of location error in the stomach, small intestine and large intestine when there are one and two sensor arrays. When there are one 4x4 sensor array, 90% location errors in the small intestine are below 48 millimeters and only 42% location error are lower than 48 millimeters in the large intestine. When two 4x4 sensor arrays are available, performance improves significantly especially in the large intestine; 50% of location errors in the stomach, small intestine and large intestine are below 38 millimeters.

From the results of our simulations, they concluded: (1) The large intestine exhibits greater location error than the stomach and the small intestine when the same numbers of sensors are available. They conjectured that these differences in location error

performance are due to the fact that the stomach, the small intestine and the large intestine have different shapes and are at different positions in human body. Most of the sensors are at much closer distance to the small intestine than to the stomach and large intestine, so that the received signal strength from the capsule suffers less attenuation in the small intestine and thus has less signal strength error. (2) The location errors in the large intestine decrease faster than both in the stomach and the small intestine when more sensors are available. (3) The location accuracy is improved if more sensors are deployed.

Chapter 3: Computational Techniques for Radio Propagation Inside the Human Body

Conducting physical measurements for localization can involve substantial effort to collect accurate databases for different environments of interest. This is more obvious in the case of the human body, where communication involving implants also has to be considered. In principle, employing computational methods does not require that any measurements be made; but some measurements are needed to check the accuracy of the computational methods and to determine the values of model parameters such as conductivity and permittivity of structural materials. The implementation of FDTD methods, however, always requires extensive computational resources.

Computation time for the FDTD technique is proportional to the size of the area, and the addition of structural details does not affect the computation significantly. However, the number of nodes used for computation is related exponentially to the size of the area and the frequency of operation. The computational methods can provide the relationship between the layout of a building or an outdoor area and the detailed channel response in a specific location. Therefore, they can provide realistic estimates of the azimuthal distribution of rays received in a multipath environment. In this chapter we discuss FDTD as a possible computational method to analyze the different characteristics of a channel.

3.1 Analysis of Path-Loss Models

This section compares a basic, MATLAB coded, time-domain FDTD formulation for the path loss around the human body with accurate Finite Element Method (FEM) modeling

in ANSYS HFSS. We show that the time domain FDTD analysis yields comparable results even though it uses a homogeneous body model and simple boundary conditions. Reasons for this important observation are investigated. The present study only considers the exterior TX and RX antennas, which are located close to the body. A more detailed FDTD simulation of on-body antennas is currently underway.

3.1.1 Circuit Model of Path-loss

When time-domain and frequency-domain models are to be compared with each other, adequate source modeling is a critical issue. Figure 10 shows the simple TX/RX model used in this study to estimate the path loss and antenna-to-antenna transfer function for FDTD and FEM models. The generator is an ideal voltage source, V_g , in series with a generator resistance, R_g , connected to a TX antenna. The receiver is an RX antenna connected to a load resistance, R_L . All voltages and currents in Figure 10 are either real quantities (time domain FDTD) or complex phasors (frequency-domain FEM). Of primary interest is the received load voltage, V_L , as a function of the generator voltage V_G . This approach gives us the voltage transfer function T_V in phasor form.

$$T_V = \frac{V_L}{V_g} \quad (3.1a)$$

The voltage transfer function depends on the values of the series resistors, the antenna impedances, and the associated path loss. Alternatively, one may be interested in the power transfer function, T_p which in phasor form is given by

$$T_P = \frac{P_L}{P_g} = \frac{|V_L|^2 / (2R_L)}{|V_g I_g^*| / 2} \quad (3.1b)$$

The transfer functions are determined using the simulation data as described below.

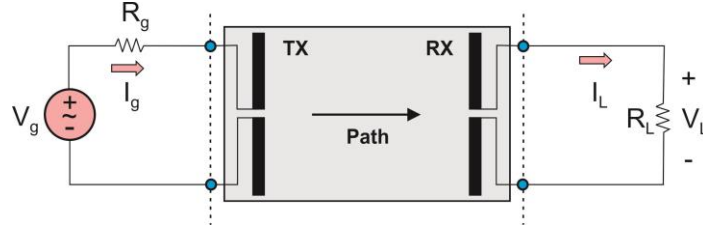


Figure 10: Circuit model of antenna-to-antenna TX/RX link.

3.1.2 Transfer Functions in Frequency Domain

When using the FDTD simulations, both transfer functions in Equations (3.1) are found directly in the time domain using the proper excitation models. This method is explained in Section 3 below. For the FEM frequency-domain ANSYS HFSS analysis we use a lumped-circuit approach as shown in Figure 11. For a system with two lumped ports (TX and RX antennas), this approach employs the impedance matrix \hat{Z} of size 2×2 , which is readily available as “solution data” in HFSS for a particular frequency. The impedance matrix is invariant to specified port impedances. The TX-RX antenna network shown in Figure 10 can thus be replaced by an equivalent two-port microwave network described by the impedance matrix \hat{Z} depicted in Figure 11b

$$\hat{Z} = \begin{bmatrix} Z_{11} & Z_{12} \\ Z_{21} & Z_{22} \end{bmatrix} \quad (3.2)$$

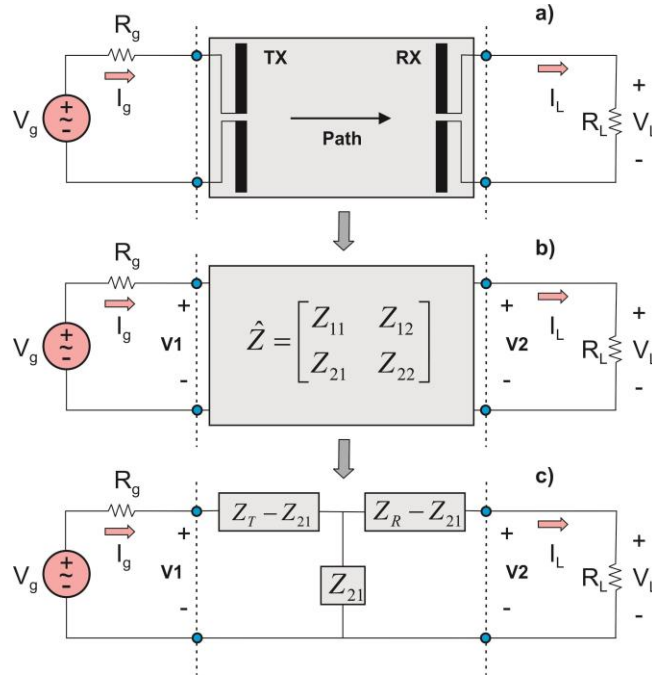


Figure 11: Network transformations of the antenna-to-antenna link; a) original TX/RX network; b) microwave impedance matrix approach; and c) equivalent T-network of lumped impedances.

The impedance approach is more appealing for this problem than the scattering S- matrix approach, since the S parameters always require an extra transmission line section at each port. Furthermore, the impedance approach explicitly relates the antenna link to the circuit parameters, and thus allows us to directly employ the well-known analytical results for small dipole and loop antennas. For reciprocal antennas, the mutual impedances are identical, i.e. $Z_{12} = Z_{21}$. When the antennas are located far way from each other, the self-impedances Z_{11} , Z_{22} are not affected by the presence of the second antenna as a scatterer, and are reduced exact antenna impedances in free space, i.e.

$$Z_{11} = Z_T, Z_{22} = Z_R \quad (3.3)$$

Thus, the two-port network in Figure 11b, with the impedance matrix given by Equation (3.1), is replaced by an equivalent T-network (a Π -equivalent network is also possible, but it is not considered). The resulting circuit is depicted in Figure 11c. The solution for the receiver voltage then becomes a straight-forward circuit analysis with the final result

$$V_L(\omega) = \frac{R_L Z_{21}}{(Z_R + R_L)(Z_T + R_g) - Z_{21} Z_{12}} V_g(\omega) \quad (3.4)$$

for the voltage transfer function known as the forward voltage gain. An equation for the power transfer could be obtained in a similar way.

3.1.3 Transfer Functions in Time Domain

The lumped port model in FDTD follows reference and is shown in Figure 12. It occupies one unit cell. The generator circuit includes the open gap antenna feed with the electric field $E_z(t, x_e, y_e, z_e)$, which is updated based on the Maxwell equations in free space. We apply Kirchhoff's Voltage Law (KVL) to loop 1 as indicated in Figure 12. This yield:

$$-V_g(t) + R_g I_g(t) - \Delta z E_z(t, x_e, y_e, z_e) = 0 \quad (3.5)$$

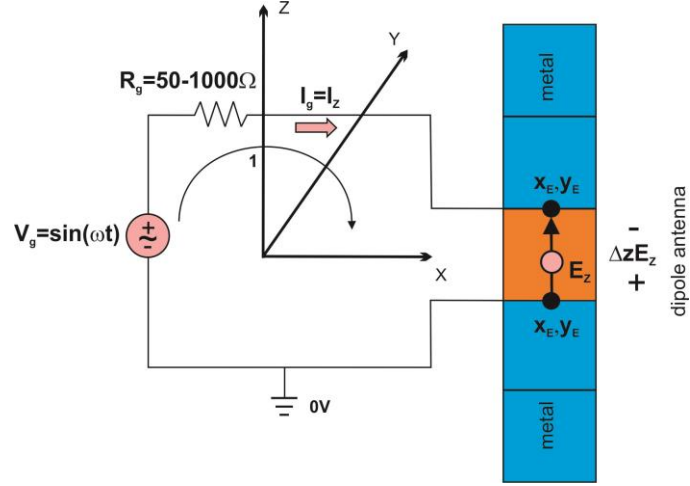


Figure 12: FDTD port model corresponding to the excitation source in Figure 10.

Solving Equation (3.5) for the current results in

$$I_g(t) = \frac{1}{R_g} V_g(t) + \frac{\Delta z}{R_g} E_z(t, x_e, y_e, z_e) \quad (3.6)$$

The FDTD version of Equation (3.6) becomes

$$I_{z,k,m,p+1/2}^n = \frac{\Delta z}{R_g} E_{z,k,m,p+1/2}^n + \frac{1}{R_G} V^n \quad (3.7)$$

where k, m, p are grid-related integers and n is discrete time. According to reference, this is the “semi-implicit formulation” for the conduction current in the sense that this current relies in part upon the updated electric field to be determined as a result of the time stepping; and it does not result in a system of simultaneous equations. This yields a numerically stable algorithm for arbitrary positive resistance values. Using Ampere's law with an impressed current source from Equation (3.7) one has the fully explicit formulation for the source

$$E_z^{n+1} = e_{s1} E_z^n + e_{s2} \Delta_x H_y^{n+1/2} - e_{s2} \Delta_y H_x^{n+1/2} - e_{s3} \frac{1}{2} (V^{n+1} + V^n) \quad (3.8)$$

Where

$$\sigma = \frac{\Delta z}{R_g \Delta x \Delta y} = \frac{1}{R_g \Delta}, \quad e_{S1} = \frac{1 - \frac{\Delta t \sigma}{2\varepsilon_{k,m}}}{1 + \frac{\Delta t \sigma}{2\varepsilon_{k,m}}}, \quad e_{S2} = \frac{\frac{\Delta t}{\varepsilon_{k,m} \Delta}}{1 + \frac{\Delta t \sigma}{2\varepsilon_{k,m}}}, \quad e_{S3} = \frac{\frac{\Delta t \sigma}{\varepsilon_{k,m} \Delta}}{1 + \frac{\Delta t \sigma}{2\varepsilon_{k,m}}} \quad (3.9)$$

with $\Delta = \Delta x = \Delta y = \Delta z$ being the unit cell size. Equations (3.7) gives us the generator current in the time domain, see Figure 10. For the receiver in Figure 10, Equations (3.7) – (3.9) again apply, but with the voltage source set equal to zero. The receiver voltage is thus given by

$$V_L(t) = R_L I_L(t) \quad (3.10)$$

The transmitted and received powers are found in the same fashion.

3.1.4 Comparison Between FDTD and FEM in Free Space

We consider two electrically small dipole antennas at 402 MHz, shown in Figure 13. Both antennas have a total length of 11.25 cm, which is considerably less than the half wavelength of 37.3cm. Therefore, both of them have a large capacitive reactance and a small radiation resistance. The antennas are assumed to consist of thin metal strips with width of 1.25cm. The antenna separation distance (from center to center) is 41.3cm, which implies a near-field link. The FDTD method uses the Yee second- order differences on a staggered grid

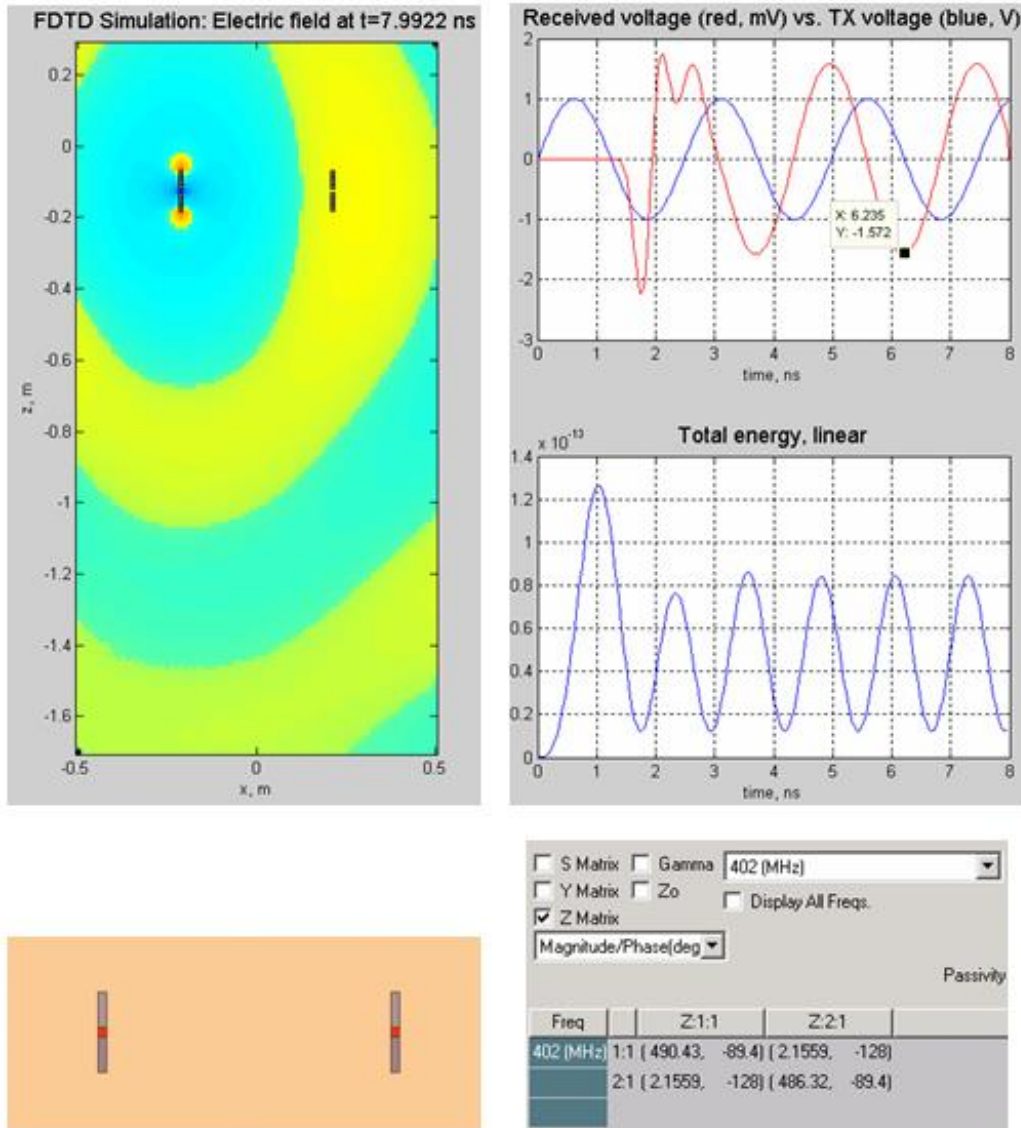


Figure 13: Top: FDTD simulations of the dipole-to-dipole link in free space; Bottom: corresponding ANSYS HFSS simulations with resulting impedance matrix. The transition region of the FDTD solution is clearly seen; it averages about 4 ns

For simplicity, we only use the first-order Mur's ABCs augmented with the superabsorption update for the magnetic field. The FDTD domain shown in Figure 13-top is larger than required; it is set up for the prospective human body modeling. Figure 13-top also shows the received voltage as a function of time versus the transmitted voltage. The entire FDTD algorithm is implemented in MATLAB. The total energy plot

in Figure 13 indicates a large reactive energy component that is typical for the near field of non-resonant antennas. The equivalent ANSYS HFSS simulation is performed using a perfectly matched layer (PML) absorbing boundary condition and a large number of tetrahedra in the FEM mesh (about 50,000). We calculate the receiver voltage in ANSYS using Equation (4) and the receiver voltage in FDTD using Equation (3.10).

Table 3.1 provides the received voltage amplitude for different values of generator/load resistances. We assume $R_g = R_L$. The source has the amplitude of 1V in all cases. One can see that the difference between the two approaches does not exceed 9%. This is generally of sufficient accuracy for path loss modeling.

TABLE 3.1. RECEIVED VOLTAGE AMPLITUDE FOR DIFFERENT VALUES OF $R_g = R_L$. THE SOURCE HAS AN AMPLITUDE OF 1 V.

$R_g = R_L$	ANSYS HFSS data for the received voltage amplitude	FDTD data for the received voltage amplitude
50Ω	0.44mV	0.45mV
1000Ω	1.57mV	1.72mV

3.1.5 Comparison between FDTD and FEM for Human Body Model

The ANSYS human body model has frequently been used in FEM simulations. This highly accurate model includes more than 20 internal meshes separately modeling heart, kidney, liver, blood, etc. After six iteration passes, we ended up with meshes on the order of 1,000,000 tetrahedra with execution times on the order of 24 hours. The corresponding geometry is shown in Figure 14. We consider the same two electrically small dipole antennas at 402 MHz. The antenna shift in Figure 14 along the z-axis in local ANSYS

HFSS coordinates is -130.5mm, -190.5mm, and -390.5mm. The antenna separation distance is the same as before.

We have exported the identical human body volume from ANSYS to MATLAB's FDTD mesh. In the FDTD model, we then assigned the average relative dielectric constant of 50 and the average body conductivity of 0.5S/m to the body volume with any large conductivity. The lungs, however, remain as air. All antenna parameters stay the same. The execution times in MATLAB are about 7 minutes for a FDTD mesh of about 800,000 individual bricks.

Table 3.2 reports the received voltage amplitude obtained using the two methods for different values of $R_g = R_L$, and different antenna positions. The source always has the amplitude of 1V. One can see that the agreement between the two data sets is excellent; the error does not exceed 12% in every case. Such an observation is important since it allows us to use the much faster (by the factor of ~100) FDTD model for obtaining accurate results.

TABLE 3.2. RECEIVED VOLTAGE AMPLITUDE FOR DIFFERENT VALUES OF $R_g = R_L$ AND DIFFERENT ANTENNA POSITIONS. THE SOURCE HAS AN AMPLITUDE OF 1 V.

$R_g = R_L$	Antenna shift in the vertical direction	ANSYS HFSS data for the received voltage amplitude	FDTD data for the received voltage amplitude
1000 Ω	-130.5mm	0.37mV	0.38mV
50 Ω	-130.5mm	0.10mV	0.12mV
1000 Ω	-190.5mm	0.28mV	0.29mV
50 Ω	-190.5mm	0.077mV	0.86mV
1000 Ω	-390.5mm	0.025mV	0.024mV
50 Ω	-390.5mm	0.007mV	Noise floor

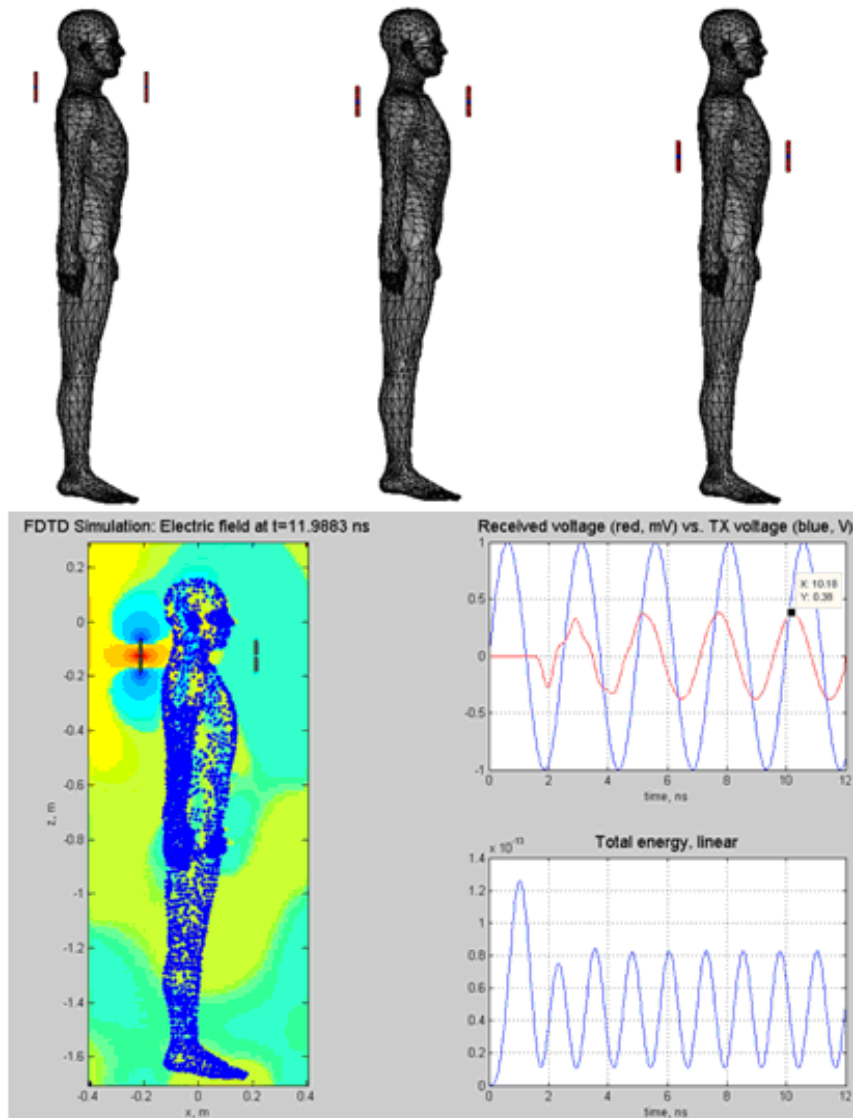


Figure 14: Antenna locations positioned around the human body. The antenna separation distance is fixed at 41.3cm. Top: FEM ANSYS mesh; Bottom: FDTD mesh; simulation results corresponding to the first case, and electric field distributions. The electric field is

3.1.6 Preliminary Results

Why does the coarse homogeneous body model in FDTD operate almost identically to the accurate FEM model? We believe that the major reason lies in the reflection of the RF signal directly from the body surface and its further diffraction around the body. When

the two antennas are located outside the body, the near-field diffraction path is the dominant path of the wireless link.

Furthermore, the EM field that enters the body is very weak due to the large impedance difference. It undergoes path loss within the body and an additional reflection loss before it leaves the body. Consequently, its contribution is insignificant, at least in this present study.

In this paper we have compared a basic time-domain FDTD simulation for the path loss around the human body in MATLAB with accurate FEM modeling of the human body in ANSYS HFSS. We have shown that the time domain FDTD analysis yields comparable results even when it uses a homogeneous body model and simple boundary conditions. The reason for this important observation is that the diffraction path around the human body is the major propagation path between transmitter and receiver. This study only considers the exterior TX and RX antennas, which are located close to the body. Two key questions need to be addressed as we continue this study:

1. How close to the body surface can the antennas be positioned in order for this observation to remain true?
2. What happens for two on-body antennas? Is the diffraction (surface wave) path still dominant?

Chapter 4: Wideband Characteristics of Radio Propagation Inside the Human Body

Wideband measurements can be performed either in the time domain by direct measurement of the impulse response of the channel, or in the frequency domain by direct measurement of the frequency response of the channel. In theory, using Fourier transform techniques, the measured time and frequency responses should provide identical results. However there are some shortcomings in using the Fourier transform of the results of measurements, particularly if the measurement system does not provide both the magnitude and the phase of the measured characteristics.

The most intuitive measurement analysis for the human body would be to use people with different weights between the same transmitter and receiver. Figure 15 shows the measurement setup with a sample human subject of weight 156 lbs, which will also be used for the FEM simulations in section 3.3. Figure 16 shows the impulse response of the channels with human subjects having different weights, each positioned between two 900 MHz dipoles. The bandwidth for this setup is 100 MHz. From Figure 16 we can see that as the weight increases, the first path power diminishes.

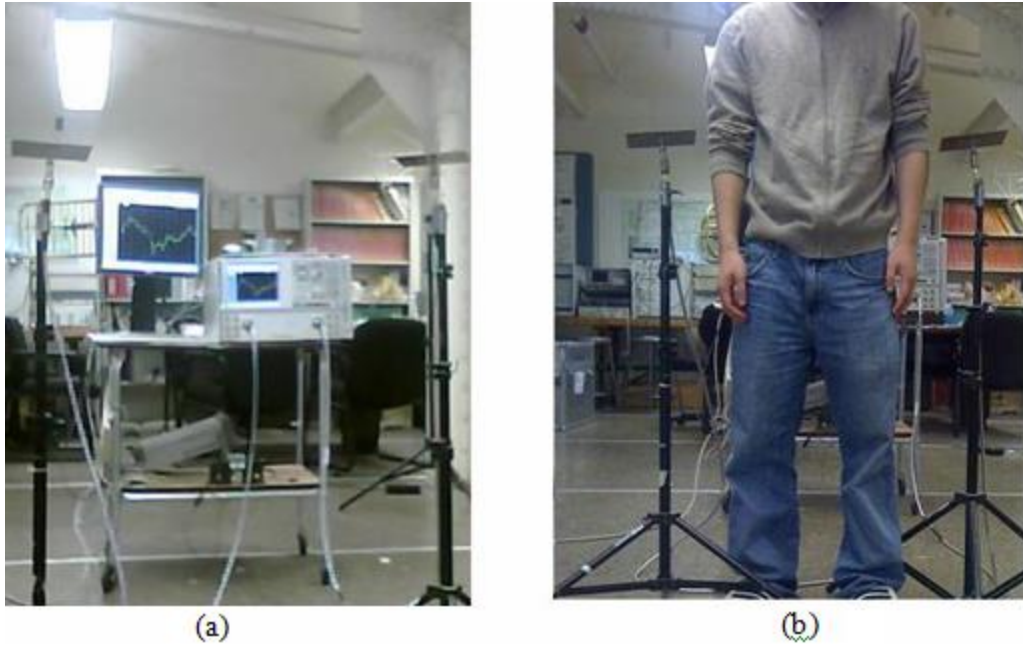


Figure 15: Measurement setup (a) without body (b) with body

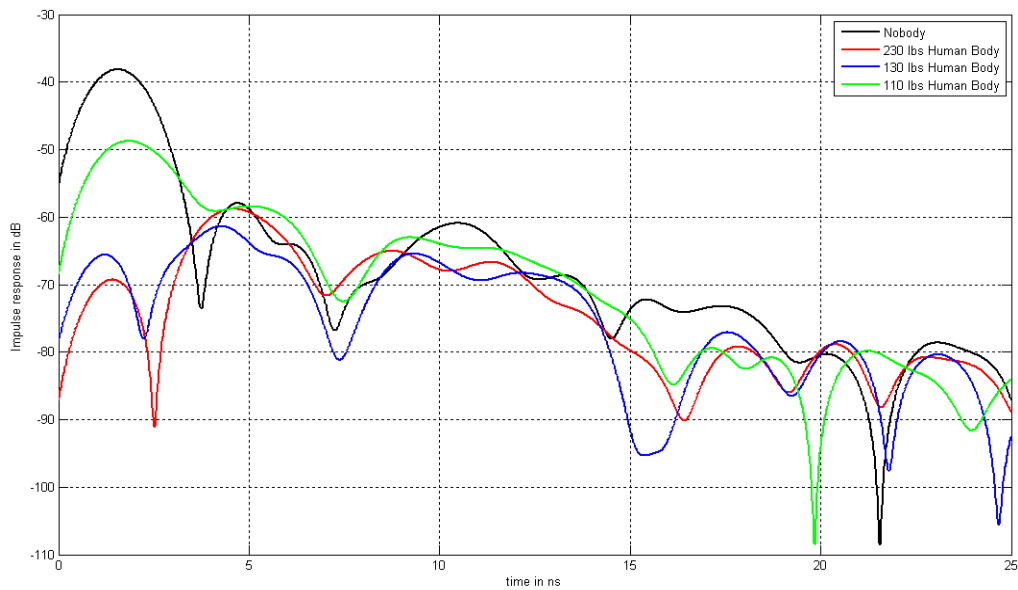


Figure 16: Impulse response obtained from measurements with human subjects of different weights

Channel measurement and modeling for body surface mounted sensors is divided into Body-to-Body and Body-to-External experiments, which are further divided into LOS and Non-LOS (NLOS) scenarios. In LOS scenarios there is a direct unobstructed path

between the transmitter and the receiver. In NLOS scenarios the body blocks the signal from direct connection path between the transmitter and the receiver. Figure 17 shows the results of two measurement experiments for body surface to body surface for LOS and body obstructed NLOS conditions, using Ultra Wideband (UWB) frequencies. In LOS experiments, we can clearly see the direct path which is also the strongest path. Considerable changes in multipath profiles suggest needs for separating LOS and NLOS channel models for these scenarios application.

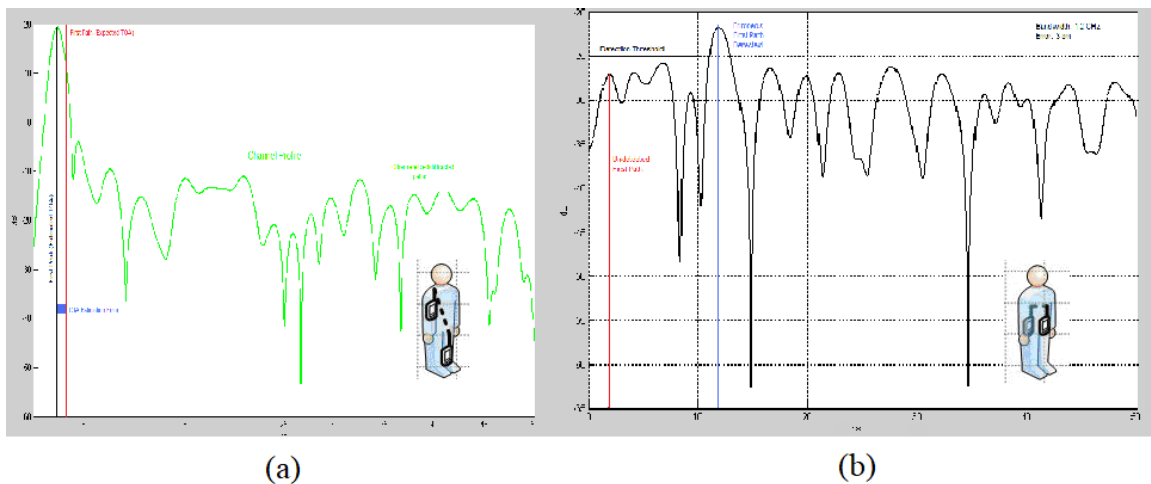


Figure 17: Channel impulse response in four different orientations of the body at Ultra Wideband (UWB) Frequencies – (a) LOS – Body-to-Body, (b) NLOS – Body-to-Body

4.1 Simulation of Wideband Characteristics using ANSYS HFSS

Conducting physical measurements for localization can involve substantial effort to collect accurate databases for different environments of interest. This is more obvious in the case of the human body, where communication involving implants also has to be considered. In principle, employing computational methods does not require that any measurements be made; but some measurements are needed to check the accuracy of the computational methods and to determine the values of model parameters such as conductivity and permittivity of structural materials. The implementation of FEM methods, however, always requires extensive computational resources.

Computation time for the FEM technique is proportional to the size of the area, and the addition of structural details does not affect the computation significantly. However, the number of nodes used for computation is related exponentially to the size of the area and the frequency of operation. The computational methods can provide the relationship between the layout of a building or an outdoor area and the detailed channel response in a specific location. Therefore, they can provide realistic estimates of the azimuthal distribution of rays received in a multipath environment. In this section we discuss FEM as a possible computational method to analyze the different characteristics of a channel.

4.1.1 An Overview of ANSYS HFSS

HFSS is a high-performance full-wave electromagnetic (EM) field simulator for arbitrary 3D volumetric passive device modeling that takes advantage of the familiar Microsoft Windows graphical user interface. It integrates simulation, visualization, solid modeling, and automation in an easy-to-learn environment where solutions to your 3D EM problems are quickly and accurately obtained. ANSYS HFSS basically employs the Finite Difference Time Domain (FEM) methodology, adaptive meshing, and brilliant graphics to give you unparalleled performance and insight to all of your 3D EM problems. ANSYS HFSS can be used to calculate parameters such as S-Parameters, Resonant Frequency, and Fields.

HFSS is an interactive simulation system whose basic mesh element is a tetrahedron. This allows you to solve any arbitrary 3D geometry, especially those with complex curves and shapes, in a fraction of the time it would take using other techniques. The name HFSS stands for High Frequency Structure Simulator. ANSYS pioneered the use of the Finite Difference Time Domain (FDTD) for EM simulation by developing/implementing technologies such as tangential vector finite elements, adaptive meshing, and Adaptive Lanczos-Pade Sweep (ALPS).

The human body model in HFSS has a millimeter level accuracy with 300+ objects including bones, muscle and organs. All frequency dependant material parameters are

included. The following sections will show that the use of this software is a valid technique to analyze the multipath characteristics of the human body channel for wideband communication and TOA-based localization. Moreover, as already established in existing literature, we can also use it to analyze Received Signal Strength (RSS) based communication and studying path-loss models. Figure 18 (b) shows the electric field plot obtained from an HFSS[™] simulation that will also be used to analyze the wideband characteristics of a wireless channel with a human body. This plot shows how the electric field, and hence normalized power, decays from the transmitter to the receiver.

4.1.2 Experimental Procedure using the ANSYS HFSS suite

The research being carried out by the Center for Wireless Information Networks (CWINS) at WPI is based on the application of localization and hence, the results are more concentrated towards the multipath characteristics of the channels. At the moment, only surface to surface measurements have been taken and have been compared with the FDTD simulation using ANSYS HFSS[™].

Both in the actual measurements and the software simulation, two dipoles in the 900 MHz band were placed 50 cm apart (Figure 15 (a) represents a similar scenario with antennas further apart) and their S21 parameter was plotted over a bandwidth of 100 MHz. This plot was then used to find the impulse response using the chirp z-transform function in MATLAB[™]. After this a person with height 172 cm and weight 156 lbs was made to stand between the two antennas (Figure 15 (b) represents a similar scenario with antennas further apart) and a human body model with similar characteristics was placed in the HFSS[™] simulation, between the two antennas (Figure 16). The impulse response

for this new channel was also plotted much in the same way as before and the comparative results are shown in Figure 19. The side faces of the radiation box in the HFSS simulations were assigned concrete as their material and the front and back faces were assigned the radiation boundary to imitate the environment of the lab.

From the measurement taken without the body, the TOA of the first path was calculated to be 1.70 ns, which roughly translates to about 51 cm - an error of 1 cm from the actual distance. The same value from the HFSS TM simulation came out to be 1.95 ns, which roughly translates to 58 cm, indicating an error of about 7 cm from the measurement. The TOA of the first path from measurements taken with the body came out to be 2.00 ns, translating into 60 cm, which means the human body added an error of 9 cm in the measurements. But the simulation with the body showed the TOA of the first path to be 1.70 ns, again an error of 9 cm from the measurements but in the other direction.

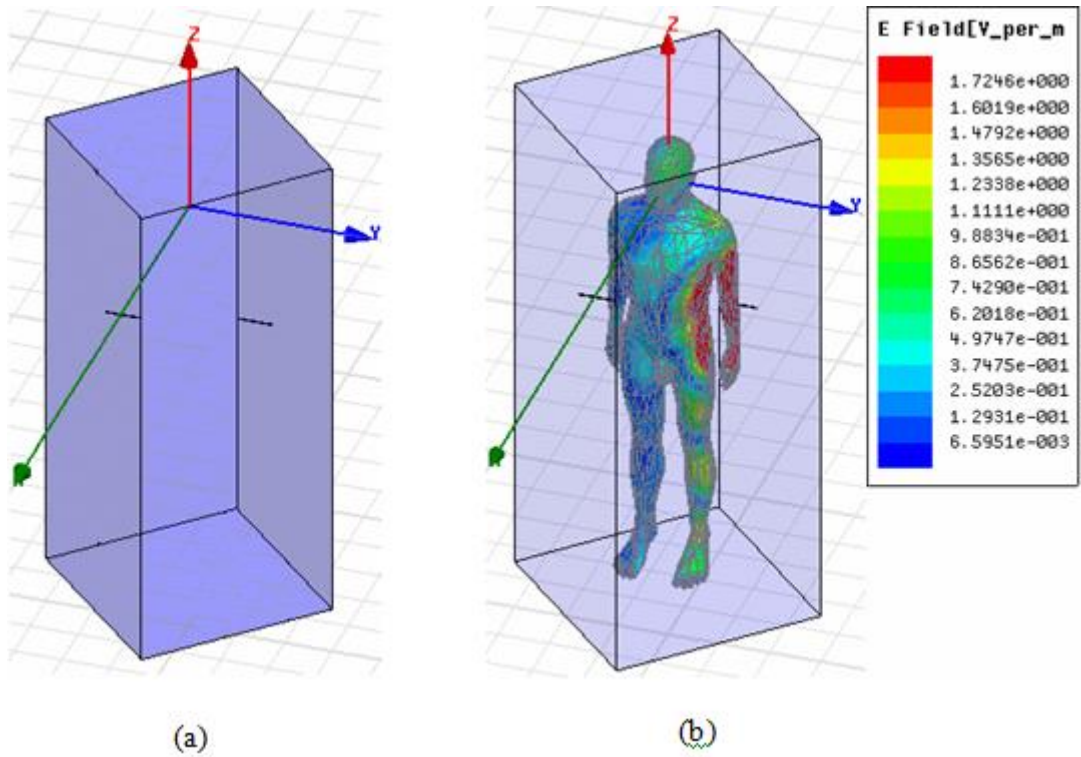


Figure 18: ANSYS HFSS TM simulation setup (a) without body (b) with body and electric field plot. The two horizontal black lines represent the dipoles

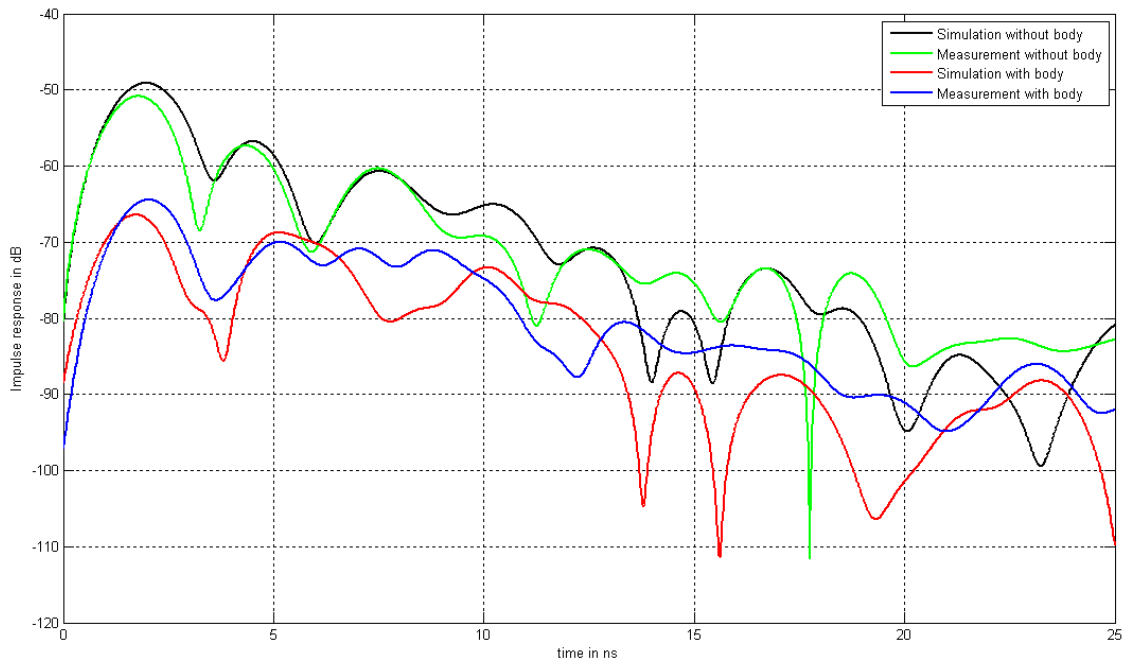


Figure 19: Impulse response obtained from the two simulated and measured channels

From Figure 19, the rms delay spread of the first three paths for the measurements without the body came out to be 4.12 ns and that of the simulation without the body came out to be 3.97 ns; a difference of just 0.15 ns. When the body was added to the measurement setup, the rms delay spread was calculated to be 3.79 ns, the same value for the simulation with the body came out to be 3.32 ns; an error of about 0.47 ns. Hence even the rms delay spread of the HFSS™ simulation was very close to that of the actual measurements, rendering little doubt that it is a valid mean to simulate the wideband profile of a channel.

As promising as these results seem, there is a need to continue with more measurements with absorbing boundaries. Also with the addition of a phantom, implant to implant measurements can also be taken and compared to their respective simulation results.

4.2 Comparison of TOA and RSS for Localization inside the Body

The human body channel suffers from severe multipath propagation and heavy shadow fading conditions so that measurements for localization are far from accurate in many instances. TOA and received signal strength (RSS) estimation are therefore susceptible to large errors due to undesirable multipath conditions. To accurately estimate TOA in indoor areas, we need to resort to different frequencies of operation and more complex signaling formats and signal processing techniques that can resolve the problems. The behavior of a TOA sensor in human body multipath propagation is highly sensitive to the bandwidth of the sensor [45]. In practice, bandwidth is limited, and the received signal

comprise a number of pulses whose amplitudes and arrival times are the same as impulses but they are shaped pulse. The superposition of all these pulse shapes forms the received signal, which we refer to as the channel profile. A common practice is to estimate the location of the direct path (DP) as the location of the peak of the first path that is the estimated TOA. In a single path environment, the actual expected and the estimated direct paths are the same. In multipath conditions, however, the peak of the channel profile gets shifted from the expected TOA, resulting in a TOA estimation error caused by the multipath condition. We refer to the distance error caused by erroneous estimate of the TOA as the *distance measurement error*. For a given multipath condition we expect that as we increase the bandwidth the distance measurement error becomes smaller. The UWB systems, which exploit bandwidths in excess of 1GHz, have attracted considerable attentions in indoor areas as a means of simulating accurate TOA for indoor geolocation applications cannot be used around the human body due to the FCC frequency limitations mentioned in the first section. However for the sake of research, we have used higher bandwidth pulses which may have higher frequency content. This is just to check whether TOA can be used as a good measure for distances between two sensors in and around the human body. The input pulse used is a Hanning pulse to match it with the window used in the Inverse Fourier Transform of the data taken from the network analyzer being used in the lab for real measurements.

Figure 20 shows an FDTD simulation in MATLAB. This figure shows electric field distribution around the human body model with the transmitter and receiver sensors at positions and **a** and **b** respectively, which are 5 cm apart. As shown in the figure (right

bottom), the TOA of the “first path” arrives at 0.2277 ns, which roughly translates to 6.83 cm, i.e. a distance measurement error of 1.83 cm. Notice, also, on the right side that the actual sensors for the simulation are not visible. This is because we tried to model a point source (with one FDTD cell) instead of a dipole antenna to eliminate the effects that maybe caused by impedance matching. However, it is not possible to model a perfect point (soft) source in MATLAB using FDTD, and that is why we can see the dip after the pulse is received. But if we plot the normalized power received, the negative region of that plot will be eliminated when the voltage is squared.

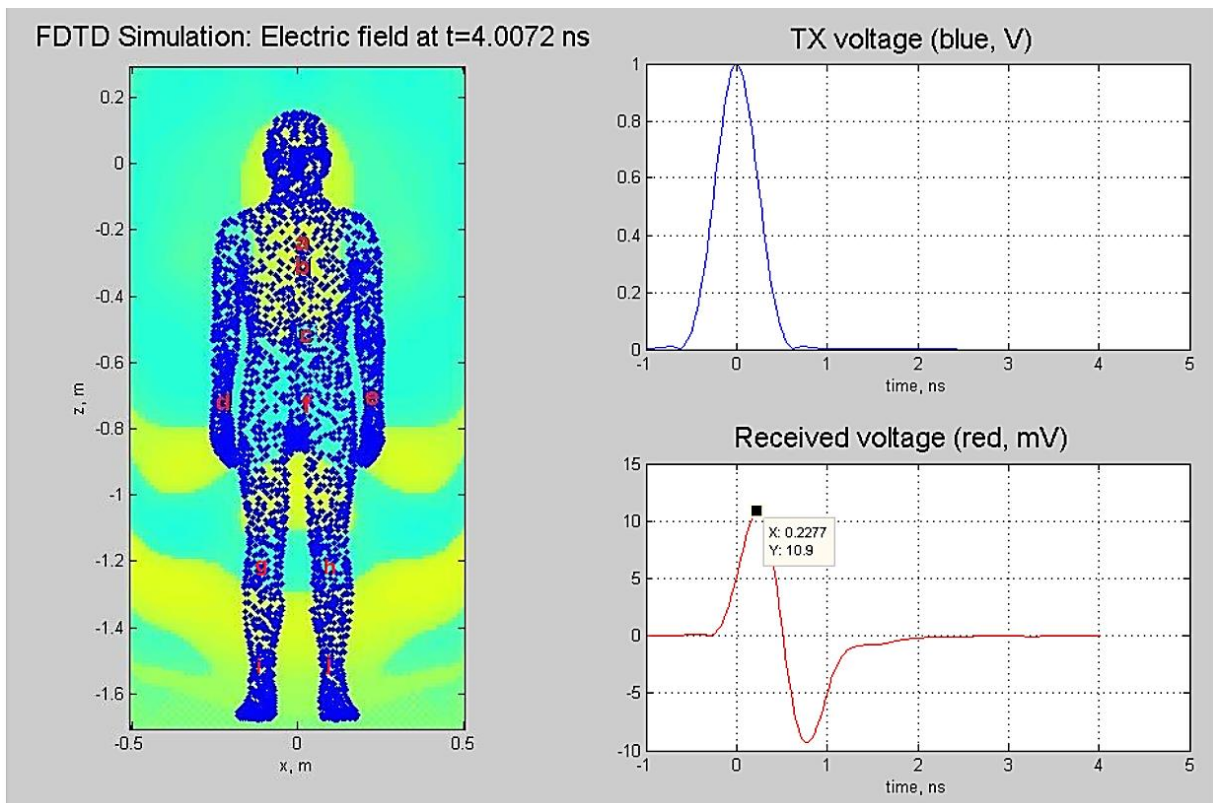


Figure 20: Left: Map of where the sensors were placed; Right: Transmitted (top) and received (bottom) voltages vs. time

4.2.1 Comparison between TOA Results and Published Path-Loss Models

A number of such simulations were carried out with the transmitter kept at position **a** and the position of the receiver was varied from positions **b** to **j**. One such simulation was run where the position of the transmitter was at **d** and the receiver was kept at position **e**. The received pulse from this simulation is shown in Figure 21. This verifies the multipath effect due to the waves traveling in different media. This is because while the other simulations were performed with both the sensors inside the homogenous body model and the waves did not have to travel outside that body, there weren't any detected second or third paths, but since in this simulation there was a change of mediums between the sensors, we can see more than one paths at the receiver.

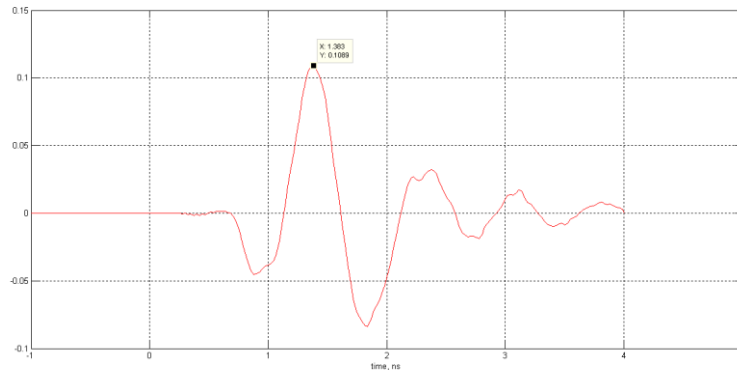


Figure 21: Received pulse (V) with transmitter and receiver sensors at positions d and e respectively

All these simulations were then used to plot a distance vs. TOA plot to assess deviations of the plotted points from a straight line representing the ideal TOA for each distance.

Figure 22 shows this plot.

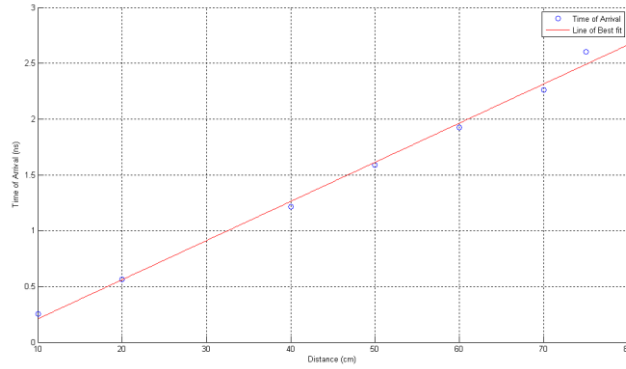


Figure 22: Time of Arrival vs. distance for various sensor positions

This plot was then compared to a plot of the same distance range obtained from the channel model described by the NIST in one of their papers that used FEM for path-loss modeling [57]. The model as shown in the paper is shown in Equation (2.24) and Table 2.1, where σ_s is the variance of the normal random variable S.

The plot obtained from this model is shown in Figure 23.

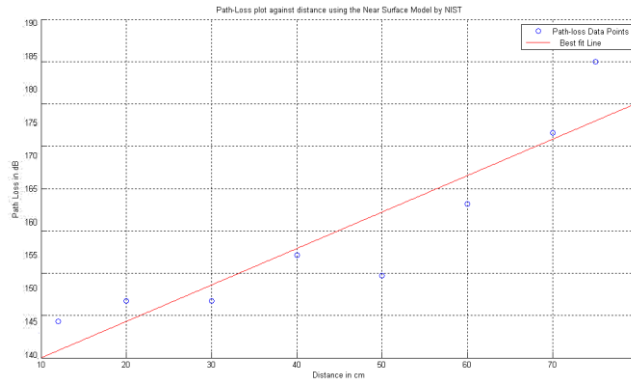


Figure 23: Plot obtained from the path-loss model in [57]

The standard deviation per dB of the Path-loss model came out to be $15.575/50 = 0.3115$.

While, the standard deviation per ns of the TOA model came out to be $0.361004/1.4 =$

0.25786 . Hence, for now, the Path-loss model seems to be more accurate. More detailed

simulations are underway to improve the accuracy of the TOA model.

To estimate the distance from the TOA plot shown in Figure 22, we used Equation (4.1) [58].

$$v(\omega) = \frac{c}{\sqrt{\varepsilon_r(\omega)}}, \quad (4.1)$$

From the slope of the TOA vs. distance line, the ε_r came out to be 1.336. This value was also used to estimate the measured value for a distance of 5 cm between the sensors, mentioned in section II. Figure 24 shows the distance measurement error plot obtained from the simulations carried out. It can be seen that the distance measurement error (given in millimeters) increases linearly with distance.

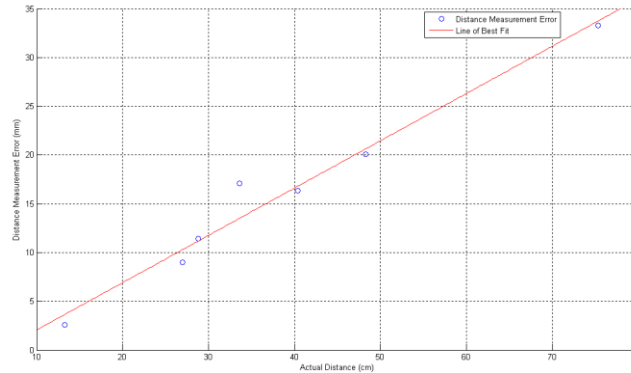


Figure 24: Distance Measurement Error from TOA for each sensor position

4.2.1 CRLB and Ranging Accuracy of TOA vs. RSS

Another metric to compare the accuracy of TOA and RSS based localization methods is their respective Cramer-Rao Lower Bounds (CRLB) [59]. The CRLB of a deterministic parameter expresses a lower bound on the variance of its estimators. The CRLB on the variance of the ranging error for TOA systems is given by:

$$\sigma_D^2 \geq \frac{1}{8\pi^2} \frac{1}{SNR} \frac{1}{TW} \frac{1}{f_0^2} \frac{1}{1 + \frac{W^2}{12f_0^2}} \quad (4.2)$$

where T is the observation time, SNR is the Signal-To-Noise-Ratio, f_0 is the center frequency of operation and W is the bandwidth of the system. For the operating frequency, bandwidth and SNR used in GPS systems this bound shows us that accuracies around several meters is achievable if we can wait for a few minutes. If we want to extend this technology to the human body we have three challenges (1) we need more precision to identify objects inside the body (2) we need to cope with the additional path loss to into the tissue within reasonable measurement times (3) we need algorithms to cope with possible multipath conditions.

In the case of RSS, the CRLB of the ranging error, using Equation (7) to relate the distance to the power, is given by:

$$\sigma_D^2 \geq \frac{(\ln 10)^2}{100} \frac{\sigma_{sh}^2}{\alpha} d \quad (4.3)$$

in which σ_{sh} is the standard deviation of the shadow fading. The distance power gradient (α) would greatly vary for different parts of the human tissue as already shown in Figure 24. Also, using Equation 10, the distance measurement error for RSS comes to the order of the distance between the transmitter and receiver, which would not be acceptable for the millimeter level accuracy required inside the human body.

To check this claim, we plotted the RSS from our simulations for each of the sensor positions shown in Figure 21. This plot is shown in Figure 25, and the α obtained from this plot came out to be 4.59, which is comparable to the model in Table I.

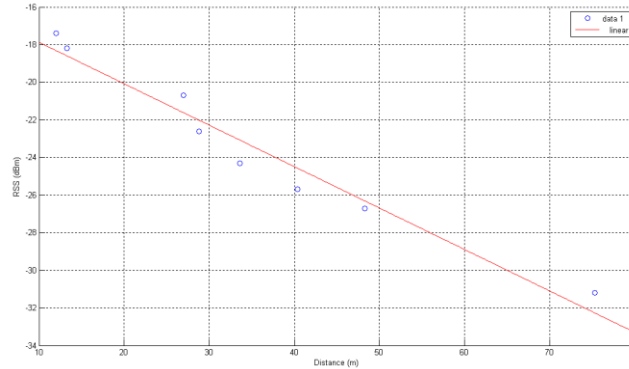


Figure 25: RSS vs. Distance plot for each sensor position

The values plotted in Figure 25 were then plugged into Equation (2.24) and the distance measurement error for RSS was plotted. This plot is shown in Figure 26. Notice that the errors obtained from TOA, shown in Figure 24, are in the millimeter range and the highest value is 3.5 cm, while the ones shown in Figure 26 are in cm, with the highest value being 5.1 cm. This confirms that ranging using RSS has larger errors than its TOA counterpart. To further confirm this, if we plug in the values given in TABLE I into Equation (10), at a distance of 40 cm, we can find the CRLB of RSS for the variance was in the range of 0.0699 and 0.427 m; while the CRLB for TOA using Equation (9) came out to be 1.1388×10^{-12} m.

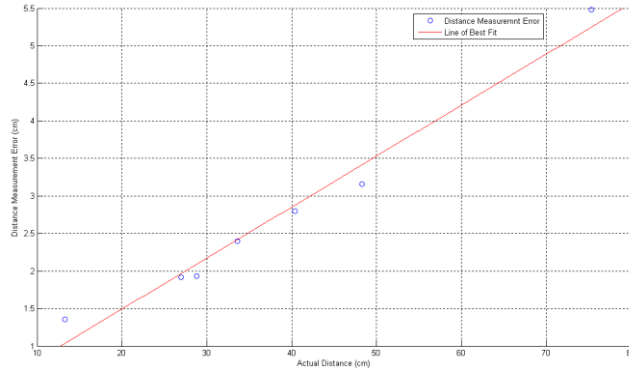


Figure 26: Distance Measurement Error from RSS for each sensor position

4.2.3 Sources of Error in Localization

The CRLB provides the ultimate measure of accuracy for ranging, but for digital systems inside the body, we get sampling and quantization errors. It may be of some interest as to why the standard deviation for TOA that was calculated experimentally in Section IV is about 10^{12} times larger than the CRLB calculated in Section V. One of the reasons for this could be that the multipath characteristics of the human body can only be truly modeled with a non-homogenous body model. Work is being done in order to import individual organs to the MATLAB FDTD solver developed by the research team. Once this is achieved and all the organs have been assigned different values of dielectric constants and conductivity, can we see the true multipath effects of the human body. Another reason for an error in TOA in real measurements could be the movement in the human body. This can change the distance between the two sensors. Figure 27 shows that, if sensor a is located on the chest and sensor b on the belt, the simple movement of raising both hands can cause a change of 3.2 cm (from 31 cm to 34.2 cm) and in the distance between them. The change in distance between these same sensors when the body is in the running position is 2.1 cm (from 31 cm to 28.9 cm). So if the position of

the surface sensor changes with simple bodily movements, there will be much larger errors in measuring the distance between these sensors and an endoscopy capsule traveling inside the GI tract. Further results that may eliminate these problems will be presented at the conference.

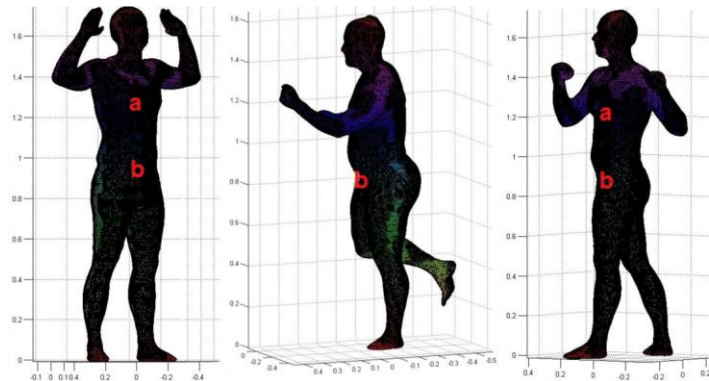


Figure 27: Change in distance of two sensors due to the movement of the body

Chapter 5: Precision of EM Simulation based Wireless Location Estimation in Multi-Sensor Capsule Endoscopy

In this chapter, we compute and examine two-way localization limits for an RF endoscopy pill as it passes through an individual's gastrointestinal (GI) tract. We obtain FDTD and FEM based simulation results position assessment employing time of arrival (TOA). By means of a three-dimension human body representation from a full wave simulation software and log-normal models for TOA propagation from implant organs to body surface, we calculate bounds on location estimators in three digestive organs: stomach, small intestine and large intestine. We present an investigation of the causes influencing localization precision, consisting of a range of organ properties; peripheral sensor array arrangements, number of pills in cooperation and the random variations in transmit power of sensor nodes. We also perform a localization precision investigation for the scenario where the transmission signal of the antenna is arbitrary with a known probability distribution. The computational solver outcome shows that the number of receiver antennas on the exterior of the body has higher impact on the precision of the location than the amount of capsules in collaboration within the GI region. The large intestine is influenced the most by the transmitter power probability distribution.

We start in Secion. 2 by detailing the computer aided FEM simulations describe the environment and the device to exterior impulse response model for the human body. After that, employing the exact position obtained form the CAD design and the mathematical model, we obtain the CRB for multiple pill positioning and the positioning bound with arbitrariness in the signal timing in Section. 3. In Section 4, we present

outcomes of the model that emphasize the sensor and tissue position factors that influence the precision of positioning. In the end, we offer our conclusions in Section 5.

5.1 Functionality and Assessment Approach

A human digestive system is made up of an intestines, a stomach and an esophagus, as illustrated in Figure 28. To effectively construct a model setup to compute the CRB of an RF endoscopy pill as it moves down the GI tract, we employ a three-dimensional body simulation from the 3D FEM based high-frequency solver (HFSS [81]). We establish the accuracy of this solver by comparing basic field measurements with their corresponding simulation models in HFSS. For research purposes we use a center frequency of 900MHz with a bandwidth of 100MHz. Each simulation run took about 4-6 hours to complete. Further details of these scenarios are presented in Section V.

5.1.1 Functionality Assessment Setup

This simulation has a 2mm 3-D resolution and comprises of radio-wave permeability characteristics of over 175 organs of a female human body. From this we obtain_spatial positions of the GI tract, as shown in Figure 29.

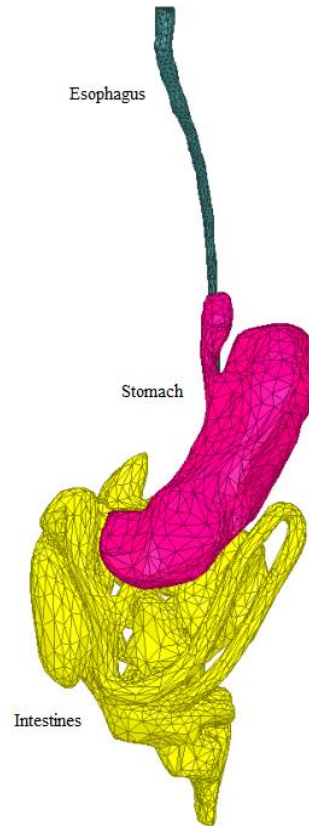


Figure 28 An illustration of the human digestive system – the typical path of an endoscopy pill

For the positioning of the external antennas, we implemented the scenario in [67], with the assumption that these antennas are positioned on a vest worn by the subject for the duration of the investigation. Matching quantities of sensors are placed in the anterior and on the posterior of the vest. We computed the CRB for 8, 16, 32 and 64 external antennas with a spatial position of $268 \ 9 \ 323 \ 9 \ 312$ mm, a representative arrangement for 32 external antennas is demonstrated in Figure 30.

5.1.2 TOA Model for the Digestive System

In this section, we outline the internal sensor to external sensor mathematical TOA model that is employed to compute the CRB of endoscopy pill positioning. This model makes use of the signal velocity model in different dielectric materials and described in [81], [102]. The key elements employed to establish this model comprise the FEM based simulation engine and human body model from ANSYS.

In our simulations, we employ a 100 mm displacement between external and internal sensors as the limit for selecting the dielectric constant. If the displacement is lower than 100 mm, we pick the near surface dielectric constant, in other cases deep tissue dielectric constants are used. An example of surface-to-surface communication can be seen in can be seen in Figure 31.

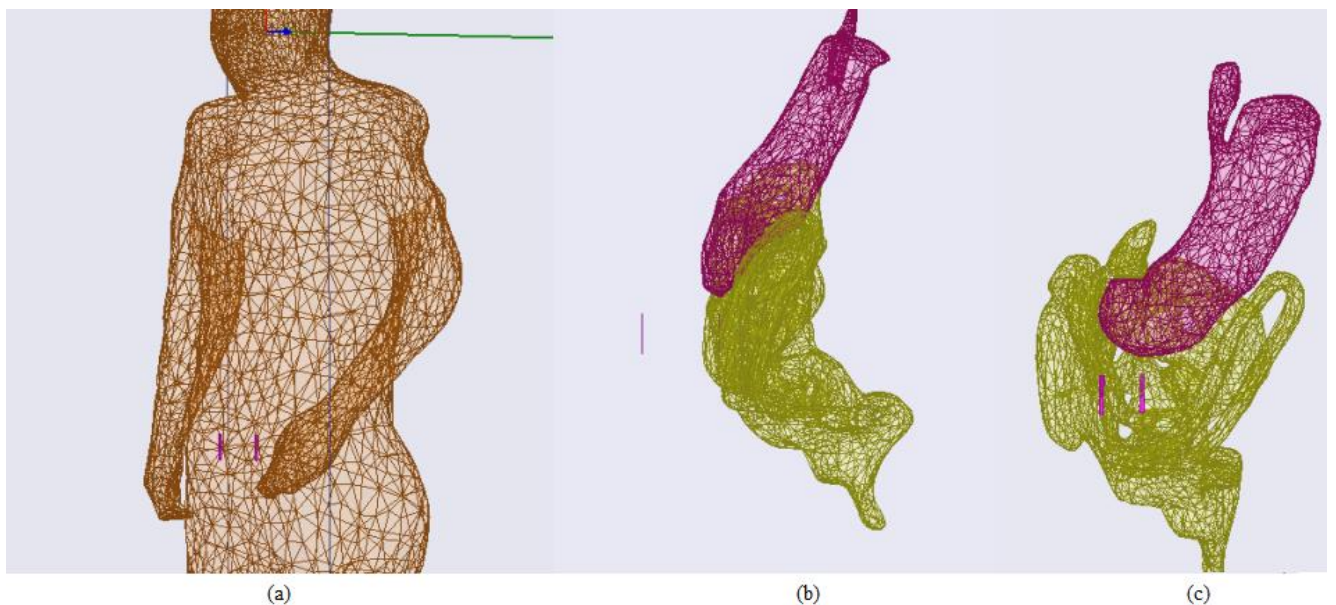


Figure 29 Positions of one internal and one external sensor as seen from (a) slightly turned outside the body (b) side of the stomach and intestines (c) slightly turned stomach and intestine

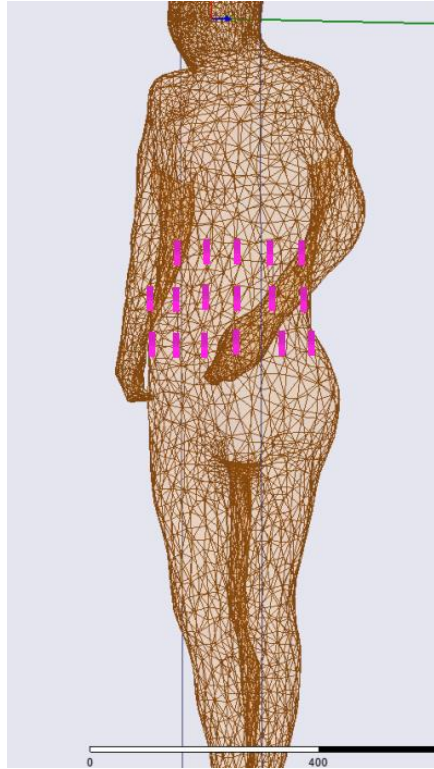


Figure 30 External Sensor Distribution (note: an equal number of sensors would be placed on the opposite side of the model)

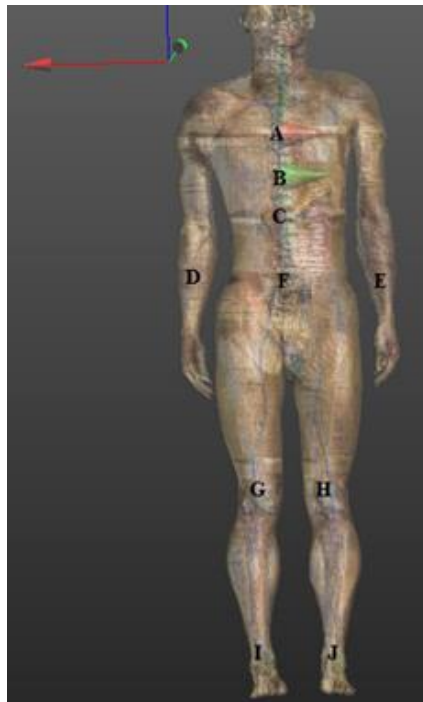


Figure 31 An example of surface-surface communication

5.1.3 Unpredictability of Impulse Time Arrival

In real-life wireless system scenarios, the antennas cannot predict an accurate time of arrival of the pulse because of the price of the standard calibration of the apparatus. While, the measured time of arrival may be a particular nanosecond value, the arrival time fluctuates by a small number of nanoseconds around this mean [84], [105]. The chief elements that affect time of arrival deviation for networks in and around the human body are enumerated thus: (a) apparatus assembly disparity and differences in battery levels from one node to the other, (b) motion of the patient subject because of movements and variations in the directions of the sensors, (c) the node devices may not be located at the exact height above from the body exterior at the same time. Some sensors could be in contact with the exterior while some may be a little ways above the surface. As stated in [83] and [104], a sensor in contact with tissue will have a slower rise time than the sensor not in contact with human tissue. All these elements add to the uncertainty in the time of arrival of the pulse, which in turn has an impact on the precision of positioning.

5.2 TOA Simulations and Observations

Figure 2 shows an FEM simulation in HFSS and Figure 32 shows the waveform received at the sensor on the surface of the belly with the transmitter positioned inside the small intestine. The transmitter and receiver are about 11 cm apart. As shown in the time domain response (TDR) plot in Figure 32, the pulse is received at 0.48 ns, which roughly translates to 14.4 cm, i.e. a distance measurement error of 3.4 cm. Notice, also, in Figure 2 that the dipoles are modeled to act as both the pill and surface sensors for the simulation. This is for simplicity of design, and to reduce simulation time and

computational resources needed. The downside of using these dipoles to represent the sensors is the capacitive dip we see before and after the received pulse in the waveform. But if we plot the normalized power received, the negative region of that plot will be eliminated when the voltage is squared.

A number of such simulations were carried out with the transmitter kept in the intestine and the position of the receiver was rotated around the body at 10 different positions at the same horizontal level, to account for different distances. One such simulation was run where the position of the transmitter was in the intestine and the receiver was kept at the same horizontal position but at the model's back, to see what happens when the waveform travels through bones and other tissue on its way from one sensor to another. This verifies the shadow-fading effect due to the higher density of organs between the two sensors. Figure 33 illustrates what the waveform looks like after passing through these denser tissue.

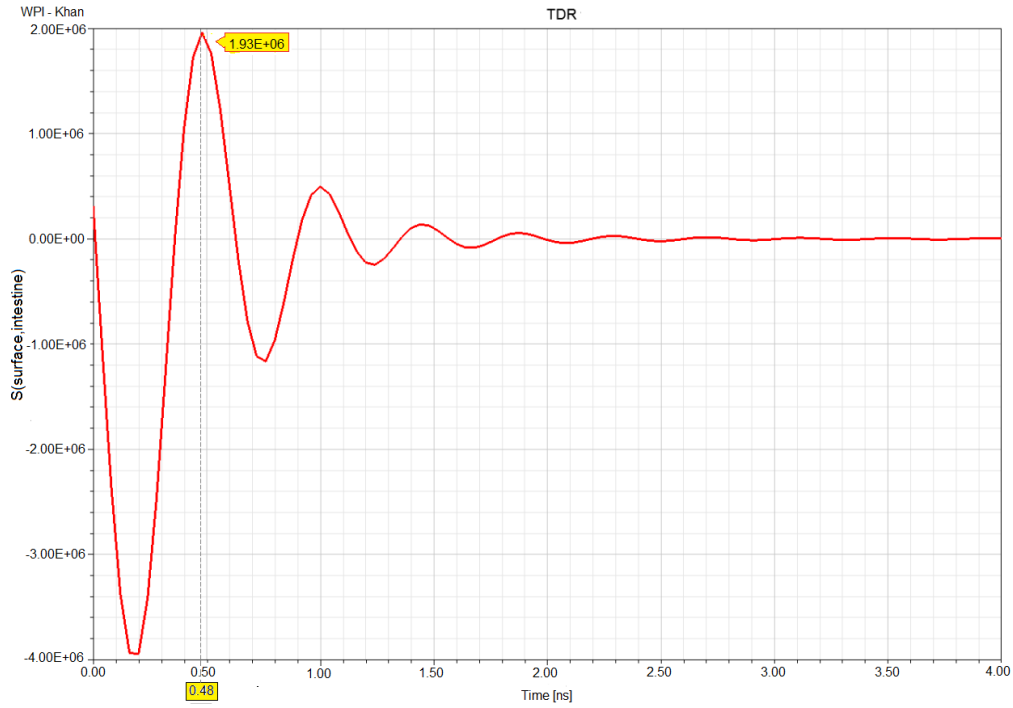


Figure 32 Impulse response between pill inside intestine and sensor on the surface of the belly

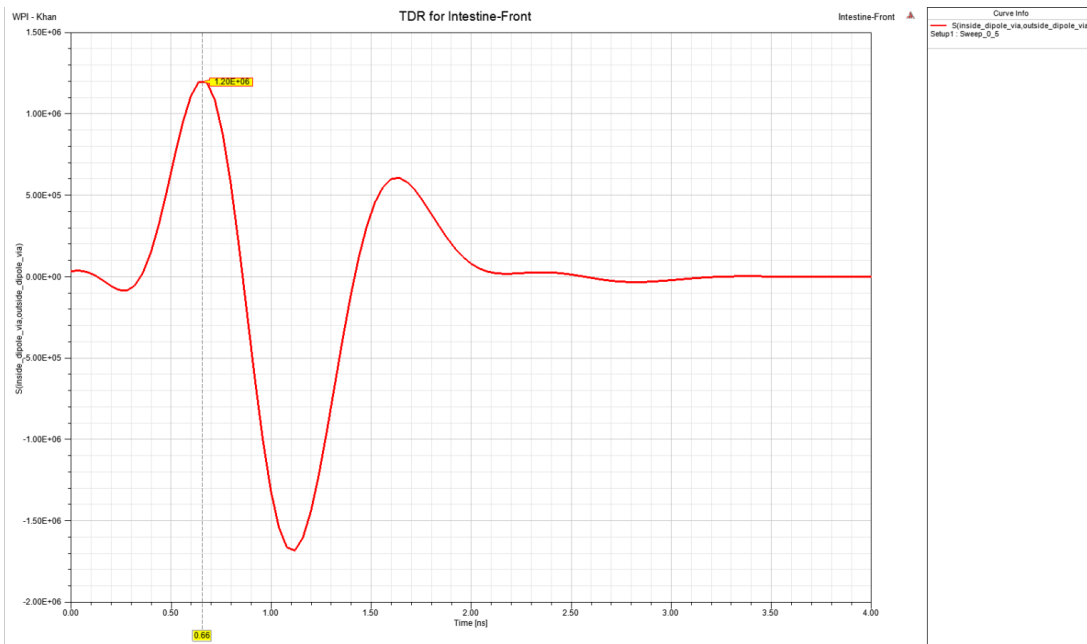


Figure 33 Impulse response between pill inside intestine and sensor on the back

All these simulations were then used to plot a distance vs. TOA plot to assess deviations of the plotted points from a straight line representing the ideal TOA for each distance.

Figure 34 shows this plot.

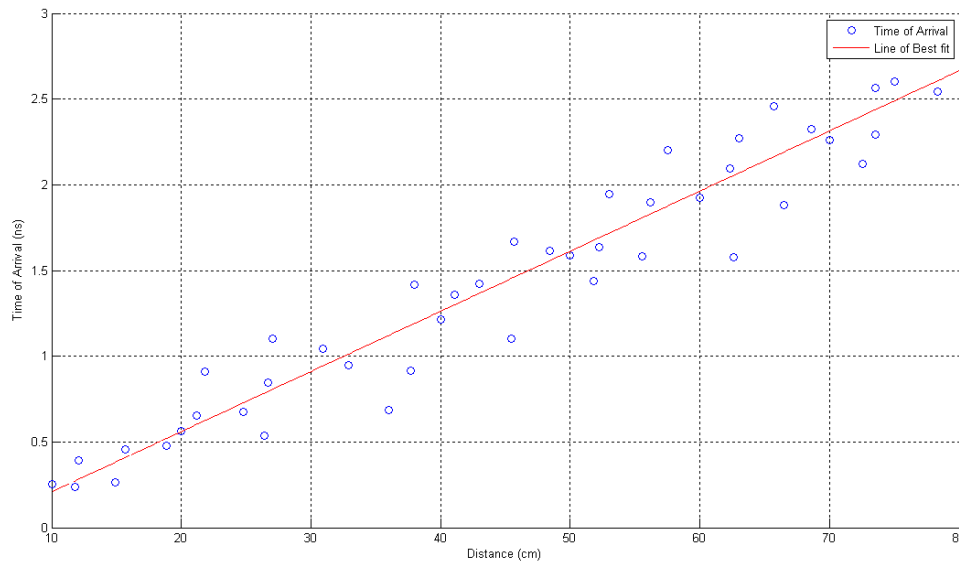


Figure 34 Time of Arrival vs. distance for various sensor positions

The standard deviation per dB of the Path-loss model, from the PDF shown in Figure 12, came out to be $15.575/50 = 0.3115$. While, the standard deviation per ns of the TOA model, from the PDF shown in Figure 36, came out to be $0.361004/1.4 = 0.25786$. Hence, the TOA model seems to be more accurate. More detailed simulations are underway to improve the accuracy of the TOA model. To estimate the distance from the TOA plot shown in Figure 34, we used Equation (1).

From the slope of the TOA vs. distance line, the ϵ_r came out to be 1.336. This value was also used to estimate the measured value for a distance of 5 cm between the sensors, mentioned in section IV. Figure 35 shows the distance measurement error plot obtained

from the simulations carried out. It can be seen that the distance measurement error (given in millimeters) increases linearly with distance.

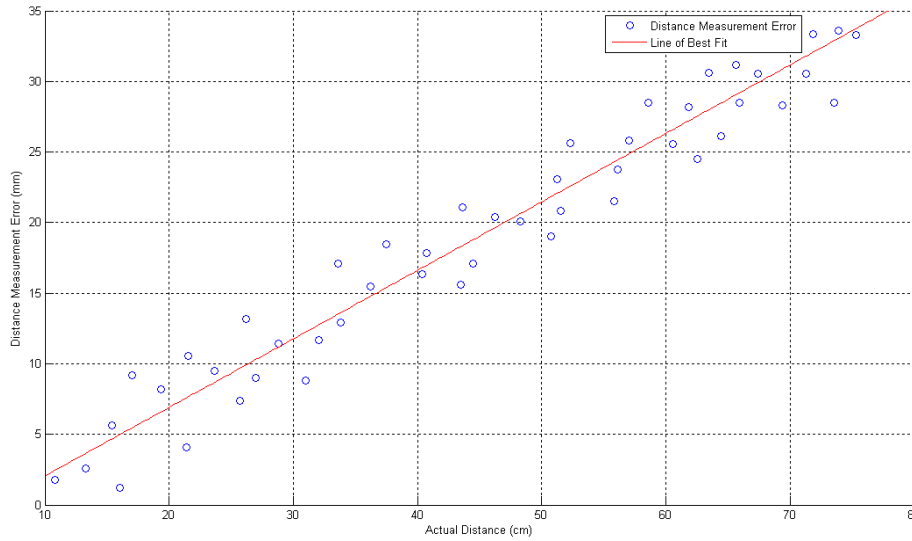


Figure 35 Distance Measurement Error from TOA for each sensor position

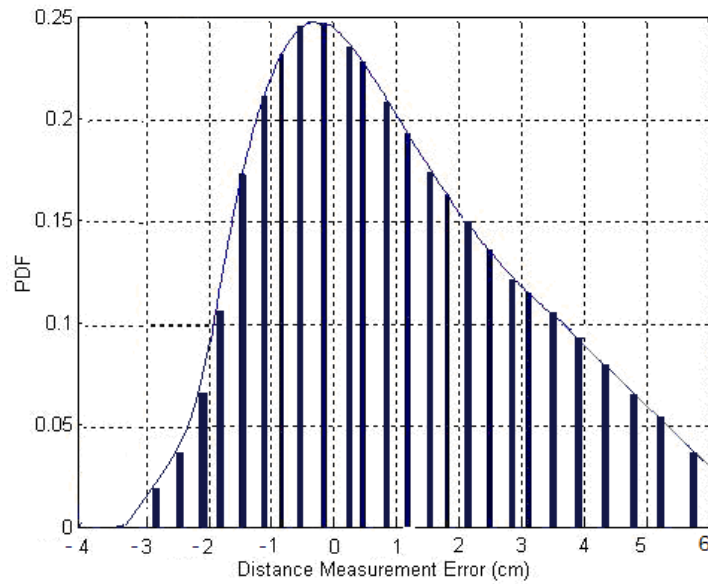


Figure 36 PDF of the Distance Measurement Error from TOA for each sensor position

5.3 CRB for TOA Based Spatial Endoscopy Pill Positioning

In this section, we develop the spatial CRB established on the TOA models described in the preceding section. We take into account both scenarios with multiple sensors are in working together and where there is variations in pulse arrival times. The CRB for 2D positioning limits has been discussed in [86]. Here, we describe the limits in all three spatial dimensions by working on the calculations done in two dimensions.

5.3.1 CRB for Multi-sensor Collaborative Positioning

Extending on the TOA models in Sect. 2, we will perform derivations for the spatial CRB for collaborative positioning of an endoscopy pill. We study the following setup: N RF sensor nodes are positioned on the surface of the human body using the vest with the position of each represented by $\theta_c = [p_1, \dots, p_N]$. The path of these sensors from the capsule could be blocked but they can quantify the TOA their adjacent nodes and the most visible sensor can receive the TOA data from the capsule and perform additional computation in collaboration with the other sensors. M number of capsules could be swallowed by the patient subject with their positions represented by $\theta_r = [p_{N+1}, \dots, p_{N+M}]$. The vector of sensor factors is $\theta = [\theta_c \theta_r]$. For this spatial scenario, $p_i = [x_i, y_i, z_i]^T$, where $i \in [1, N+M]$ and T is the transpose action. The unidentified elements to be calculated may be denoted by a $3 \times N$ matrix.

$$\begin{aligned} \theta_c &= [p_1, p_2, \dots, p_N], \\ &= \begin{bmatrix} x_1 & x_2 & \dots & x_N \\ y_1 & y_2 & \dots & y_N \\ z_1 & z_2 & \dots & z_N \end{bmatrix} \end{aligned} \quad (5.1)$$

Take the sensors into consideration (sensors comprise the pill and surface antennas). i and j receive paired-up signals X_{ij} . We make the assumption that all surface antennas can detect the TOA from the pill travelling through the GI tract, but the multi-path characteristics for the various transmission paths change as the number of different media between the surface antenna and the pill travelling down the GI tract varies. Hence, we take $H(i) = \{j; \text{sensor } j \text{ receives linked-up signals from sensor } i\}$. $H\{i\} = \{1, \dots, i-1, i+1, \dots, N+M\}$ for $i \in [1, N]$ and $H\{i\} = \{1, \dots, N\}$ for $i \in [N+1, N+M]$, since a sensor is not able to receive a linked signal from itself and the surface antennas will not receive signals from other receivers either. Thus, the size of the received vector X is $N \times (N+M-1) + M \times N$.

Using mutuality, we make the assumption $X_{ij} = X_{ji}$, therefore, it is enough to study just the lower vertex of the receiver matrix X when expressing the combined probability function [86]. The CRB on the covariance matrix of any unbiased estimator θ is given by [86]:

$$\text{cov}(\hat{\theta}) = E[(\hat{\theta} - \theta)(\hat{\theta} - \theta)^T] \geq F_{\theta}^{-1} \quad (5.2)$$

where $E[.]$ is the expectation operation and F is the Fisher information matrix (FIM) defined as:

$$\begin{aligned} F_{\theta} &= -E \nabla_{\theta} (\nabla_{\theta} \ln f(X|\theta))^T \\ &= E_{\theta} \left[\frac{\partial}{\partial \theta} \ln f(X|\theta) \left(\frac{\partial}{\partial \theta} \ln f(X|\theta) \right)^T \right] \\ &= \begin{bmatrix} F_{R_{XX}} & F_{R_{XY}} & F_{R_{XZ}} \\ F_{R_{XY}}^T & F_{R_{YY}} & F_{R_{YZ}} \\ F_{R_{XZ}}^T & F_{R_{YZ}}^T & F_{R_{ZZ}} \end{bmatrix} \end{aligned} \quad (5.3)$$

where $f(X|\theta)$ is the joint PDF of the observation vector X conditioned on θ . For the RSS measurements case, the $X_{i,j}$ are log-normal random variables, and the density is given by [86]

$$\begin{aligned}
f(X_{i,j}|p_i, p_j) &= \frac{\frac{10}{\log 10}}{\sqrt{2\pi\sigma_{dB}^2}} \frac{1}{X_{i,j}} \exp \left[-\frac{b}{8} \left(\log \frac{d_{i,j}^2}{\tilde{d}_{i,j}^2} \right)^2 \right] \\
b &= \left(\frac{10\alpha}{\sigma_{dB}} \right)^2, \\
\tilde{d}_{i,j} &= d_0 \left(\frac{X_0}{X_{i,j}} \right)^{\frac{1}{\alpha}}, \\
d_{i,j} &= \sqrt{(x_i - x_j)^2 + (y_i - y_j)^2 + (z_i - z_j)^2}
\end{aligned} \tag{5.4}$$

for $i = 1, 2, \dots, N + M$ and $j \in H(i)$, $\tilde{d}(i,j)$ is the MLE of range $d_{i,j}$ given received power $X_{i,j}$.

Then the logarithm of the joint condition pdf is:

$$l(X|\theta) = \sum_{i=1}^{M+N} \sum_{j \in H_{i,j} < i} \log f_{X|\theta}(X_{i,j}|p_i, p_j) \tag{5.5}$$

It is mentioned in [85], [106] that the second-order partial differential of (7) w.r.t θ_r and θ_s is going to be a total of terms if θ_r and θ_s are coordinates of the same sensor k , but will be only one term if θ_r and θ_s are coordinates of separate sensors k and l , $k \neq l$. For example:

$$\begin{aligned}
\frac{\partial^2 l(X|\theta)}{\partial x_k \partial z_k} &= -b \sum_{i \in H(k)} \frac{(x_i - x_k)(z_i - z_k)}{d_{i,k}^4} \left[-\log \frac{d_{i,k}^2}{\tilde{d}_{i,k}^2} - 1 \right] \\
\frac{\partial^2 l(X|\theta)}{\partial x_k \partial z_l} &= -b I_{H(k)}(l) \frac{(x_i - x_k)(z_i - z_k)}{d_{i,k}^4} \left[\log \frac{d_{i,k}^2}{\tilde{d}_{i,k}^2} - 1 \right]
\end{aligned} \tag{5.6}$$

where $I_{H(k)}(l) = 1$ if $l \in H(k)$ and 0 otherwise. Since $E\left(\frac{d_{i,k}^2}{\tilde{d}_{i,k}^2}\right) = 0$ Thus, the elements of F_θ

are:

$$\begin{aligned}
[F_{R_{XX}}]_{k,l} &= \begin{cases} b \sum_{i \in H(k)} \frac{(x_k - x_i)^2}{\sigma_{kl}^4} & k = l \\ -b I_{H(k)}(l) \frac{(x_k - x_i)^2}{\sigma_{kl}^4} & k \neq l \end{cases} \\
[F_{R_{XY}}]_{k,l} &= \begin{cases} b \sum_{i \in H(k)} \frac{(x_k - x_i)(y_k - y_i)}{\sigma_{kl}^4} & k = l \\ -b I_{H(k)}(l) \frac{(x_k - x_i)(y_k - y_i)}{\sigma_{kl}^4} & k \neq l \end{cases} \\
[F_{R_{XZ}}]_{k,l} &= \begin{cases} b \sum_{i \in H(k)} \frac{(x_k - x_i)(x_k - z_i)}{\sigma_{kl}^4} & k = l \\ -b I_{H(k)}(l) \frac{(x_k - x_i)(z_k - z_i)}{\sigma_{kl}^4} & k \neq l \end{cases} \\
[F_{R_{YY}}]_{k,l} &= \begin{cases} b \sum_{i \in H(k)} \frac{(y_k - y_i)^2}{\sigma_{kl}^4} & k = l \\ -b I_{H(k)}(l) \frac{(y_k - y_i)^2}{\sigma_{kl}^4} & k \neq l \end{cases} \\
[F_{R_{YZ}}]_{k,l} &= \begin{cases} b \sum_{i \in H(k)} \frac{(y_k - y_i)(z_k - z_i)}{\sigma_{kl}^4} & k = l \\ -b I_{H(k)}(l) \frac{(y_k - y_i)(z_k - z_i)}{\sigma_{kl}^4} & k \neq l \end{cases}
\end{aligned} \tag{5.7}$$

Let \hat{x}_i ; \hat{y}_i ; \hat{z}_i be the unbiased estimation of x_i , y_i , z_i , the trace of the covariance of the i th location estimate is given by:

$$\begin{aligned}
\sigma_i^2 &= \text{tr}\{\text{cov}_\theta(\hat{x}_i, \hat{y}_i, \hat{z}_i)\} \\
&= \text{Var}_\theta(\hat{x}_i) + \text{Var}_\theta(\hat{y}_i) + \text{Var}_\theta(\hat{z}_i), \\
&\geq \left[F_{R_{XX}} - (F_{R_{XY}} F_{R_{XZ}}) \begin{pmatrix} F_{R_{YY}} & F_{R_{YZ}} \\ F_{R_{YZ}} & F_{R_{ZZ}} \end{pmatrix}_{i,i}^{-1} \begin{pmatrix} F_{R_{XY}} \\ F_{R_{XZ}} \end{pmatrix} \right] \\
&+ \left[F_{R_{XY}} - (F_{R_{XY}} F_{R_{YZ}}) \begin{pmatrix} F_{R_{XX}} & F_{R_{XZ}} \\ F_{R_{XZ}} & F_{R_{ZZ}} \end{pmatrix}_{i,i}^{-1} \begin{pmatrix} F_{R_{XY}} \\ F_{R_{YZ}} \end{pmatrix} \right]_{i,i}^{-1} \\
&+ \left[F_{R_{ZZ}} - (F_{R_{XZ}} F_{R_{YZ}}) \begin{pmatrix} F_{R_{XX}} & F_{R_{XY}} \\ F_{R_{XY}} & F_{R_{YY}} \end{pmatrix}_{i,i}^{-1} \begin{pmatrix} F_{R_{XZ}} \\ F_{R_{YZ}} \end{pmatrix} \right]_{i,i}^{-1} \quad (5.8)
\end{aligned}$$

5.3.2 CRB for TOA Positioning with Sensor with Highest RSS (Path of Least Resistance)

One metric to relate the precision of TOA and RSS established positioning approaches is their corresponding Cramer-Rao Lower Bounds (CRLB) [71]. The CRLB of a deterministic factor states a lower bound on the variance of its estimators.

For the operational rate, bandwidth and SNR employed in GPS systems this limit demonstrates that precision of a few meters is attainable if we can wait for some minutes. If we want to expand this technology to include body area networks, we have three issues (1) we require more accuracy to pinpoint objects contained in the body (2) we need to handle the extra path loss suffered by the signal while traveling into the tissue within practical measurement periods (3) we require procedures to handle potential multipath environments.

The distance power slope would significantly vary for different portions of the human flesh as presented in Figure 39. Also, the distance measurement error for RSS comes to

the order of the space between the transmitter and receiver, which would not be satisfactory for the millimeter level precision requisite inside the human body.

To verify this statement, we plotted the RSS from our simulations for each of the surface antenna locations shown in Figure 20. This plot is shown in Figure 37, and the gradient obtained from this plot came out to be 4.59, which is analogous to the model in published by NIST [78],[98].

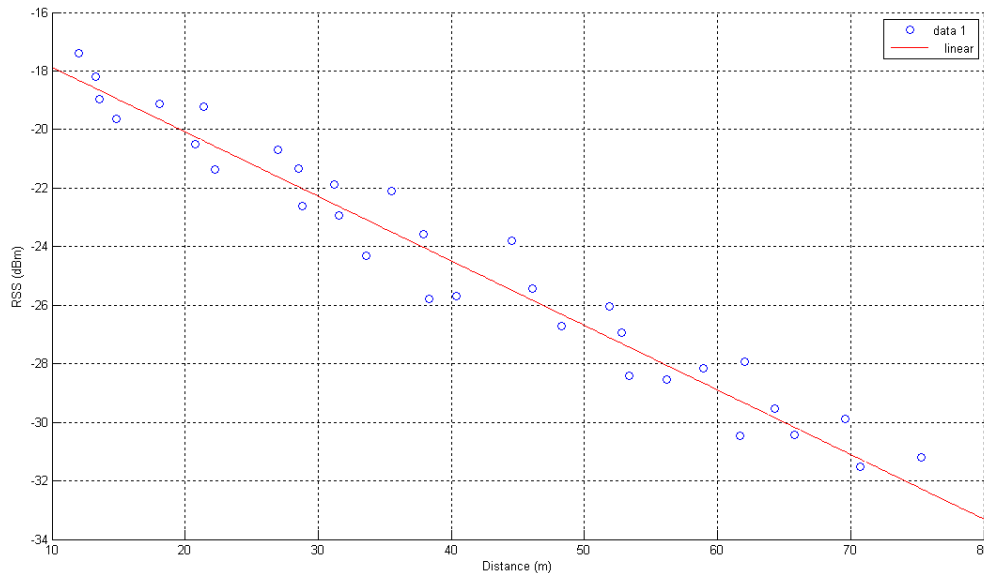


Figure 37 RSS vs. Distance plot for each sensor position

The values plotted in Figure 37 were then plugged into the NIST model and the distance measurement error for RSS was plotted. This plot is shown in Figure 28. Notice that the errors obtained from TOA, shown in Figure 35, are in the millimeter range and the highest value is 3.5 cm, while the ones shown in Figure 38 are in cm, with the highest value being 5.1 cm. This confirms that ranging using RSS has larger errors than its TOA counterpart. To further establish this, if we plug in the values given in Figure 38 into the

path-loss model defined by Sarafyan et al. [78], [98], at a distance of 50 cm, we can evaluate the CRLB on the variance of path-loss was in the range of 0.0699 and 0.427 dB; while the CRLB on the variance of TOA using Equation (9) at the same distance came out to be 0.011388ns.

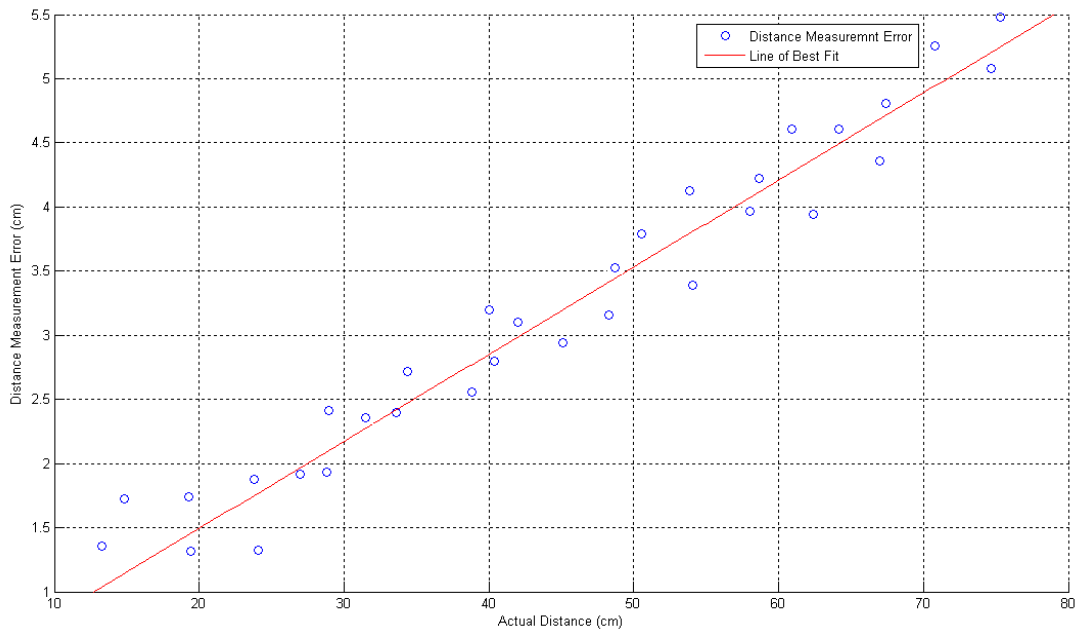


Figure 38 Distance Measurement Error from RSS for each sensor position

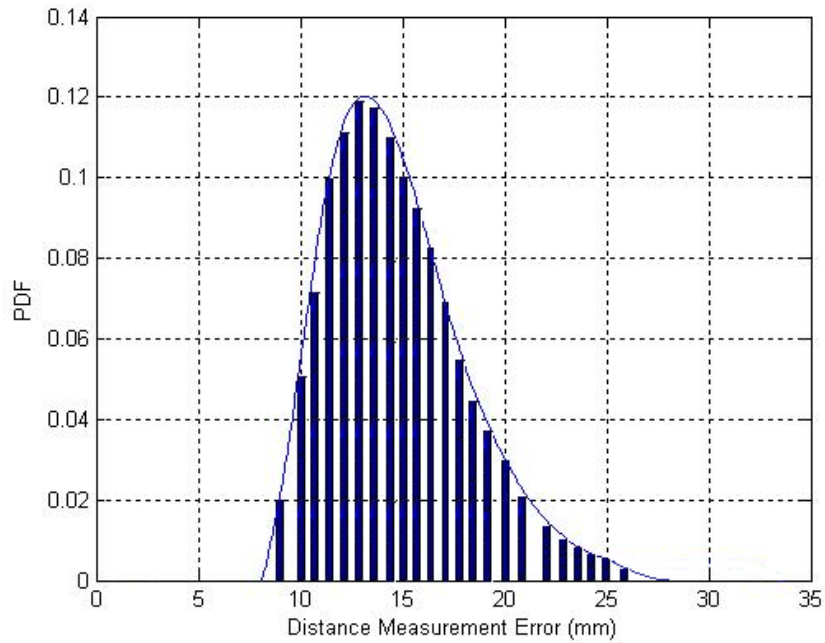


Figure 39 PDF of the Absolute Values of Distance Measurement Error from RSS for each sensor position

In this section, the variables to be calculated are the x , y and z positions of the pill, and a fresh array $\pi = [\pi_{01}, \dots, \pi_{0N}]$ because not any of the N surface antennas have precise information of the time of arrival of the pulse it transmits. The Bayesian CRB [86], [87] also known as Van trees inequality says that any approximation θ' must have an inaccuracy association matrix R_ϵ given by

$$R_\epsilon > F^{-1} = [F_\theta + F_P] \quad (5.9)$$

where $R_\epsilon = E[(\theta' - \theta) (\theta' - \theta)^T]$, and F_θ and F_P will be the FIM and the previous data matrix accordingly, given by eq. 5.10

$$\begin{aligned}
F_\theta &= -E[\nabla_\theta(\nabla)_\theta \ln f(p_{i,j}|\theta)^T] \\
F_p &= -E[\nabla_\theta(\nabla)_\theta \ln f(\theta)^T]
\end{aligned} \tag{5.10}$$

where $p_{i,j}$ would be the dual-directional impulse response array. The previous data matrix F_p is given in eq. 5.10

$$F_p = \text{diag}[0_n^T, 0_n^T, 0_n^T, \frac{1_N^T}{\sigma_n^2}] \tag{5.11}$$

where 0_n would be an n -length array of zeros and 1_N represents an array of length N consisting of ones, while σ_n^2 would be the variance of the random variable π_{0i} (the time of arrival 1 cm away from the pill i) that is supposed to have an i.i.d Gaussian probability distribution for each surface antenna i .

We represent the dual-directional measurements $P_{i,j}$ and $P_{j,i}$ by the array $p_{i,j} = [P_{i,j}P_{j,i}]$ as a dual-variable Gaussian with an average of $u_{i,j}$ and a variance of $C_{i,j}$, where

$$u_{i,j} = \begin{bmatrix} \pi_{0j} - 10x \log_{10} \frac{|r_i - r_j|^2}{\Delta_u^2} \\ \pi_{0i} - 10x \log_{10} \frac{|r_i - r_j|^2}{\Delta_u^2} \end{bmatrix} \tag{5.12}$$

$$C_{i,j} = \sigma_{dB}^2 \begin{bmatrix} 1 & \rho \\ \rho & 1 \end{bmatrix} \tag{5.13}$$

where α denotes the time of arrival exponent, and ρ would be the association constant among the dual-directional responses, $0 \leq \rho \leq 1$. For the sake of simplicity we convert the dual-directional response array $p_{i,j}$ to an orthogonal matrix A using the following derivation:

$$\begin{aligned}\tilde{\rho}_{i,j} &= Ap_{i,j}, \\ A &= \begin{bmatrix} 1 & 1 \\ 1 & -1 \end{bmatrix}\end{aligned}\quad (5.14)$$

Such a full rank transformation of measurement does not change the Fisher information. For simplicity of notation, we denote $\tilde{p}_{ij} = [\bar{p}_{ij} p_{ij}^\Delta]^T$ where \bar{p}_{ij} corresponds to the average of the two measurements and p_{ij}^Δ corresponds to the difference between the two measurements. After some mathematical analysis, it is seen that \bar{p}_{ij} has a mean \bar{u}_{ij} and covariance \bar{C} and p_{ij}^Δ has a mean u_{ij}^Δ and covariance C^Δ as given below:

$$\begin{aligned}\bar{u}_{ij} &= \pi_{0j} + \pi_{0i} - 10x \log_1 0 \frac{|r_i - r_j|^2}{\Delta_0 2} \\ \bar{C} &= \frac{(1 + \rho)\sigma_{dB}^2}{2} I_{3n+N}, \\ u_{ij}^\Delta &= \frac{\pi_{0j} - \pi_{0i}}{2}, \\ C^\Delta &= \frac{(1 - \rho)\sigma_{dB}^2}{2} I_{3n+N},\end{aligned}\quad (5.15)$$

where I_{3n+N} is $3n + N \times 3n + N$ identity matrix and \bar{u} and u^Δ are the mean values of the sum and difference of measurements respectively for all measurement pairs,

$$\begin{aligned}\bar{u} &= [\bar{u}_{i_1, j_1}, \dots, \bar{u}_{i_n, j_n}]^T \\ u^\Delta &= [u_{i_1, j_1}^\Delta, \dots, u_{i_n, j_n}^\Delta]\end{aligned}\quad (5.16)$$

where $i_1; j_1; \dots; i_s; j_s$ corresponds to each unique pair. A pair makes measurement if they are in the measurement range of each other. Here we assume that the measurement range is infinite (i.e., every sensor can do measurements with every other sensor). The Fisher information matrix F_θ given by eq 5.10 can be split into two sub matrices \bar{F}_θ and F_θ^Δ corresponding to sum and difference measurements due to their independence.

$$F_{\theta} = \bar{F}_{\theta} + F_{\theta}^{\Delta} \quad (5.17)$$

The FIM of a vector of multivariate Gaussian measurements with mean $l(\mathbf{h})$ and covariance C is given by [82], [103]

$$\begin{aligned} F_{\theta} &= [\nabla_{\theta}\mu(\theta)]^T C^{-1} [\nabla_{\theta}\mu(\theta)], \\ &= \begin{bmatrix} F_{R_{XX}} & F_{R_{XY}} & F_{R_{XZ}} & F_{R_{X\pi}} \\ F_{R_{YX}} & F_{R_{YY}} & F_{R_{YZ}} & F_{R_{Y\pi}} \\ F_{R_{ZX}} & F_{R_{ZY}} & F_{R_{ZZ}} & F_{R_{Z\pi}} \\ F_{R_{\pi X}} & F_{R_{\pi Y}} & F_{R_{\pi Z}} & F_{R_{\pi\pi}} \end{bmatrix} \end{aligned} \quad (5.18)$$

From eq. 5.17, we have,

$$\begin{aligned} \bar{F}_{\theta} &= [\nabla_{\theta}\bar{\mu}(\theta)]^T C^{-1} [\nabla_{\theta}\bar{\mu}(\theta)], \\ &= \begin{bmatrix} \bar{F}_{R_{XX}} & \bar{F}_{R_{XY}} & \bar{F}_{R_{XZ}} & \bar{F}_{R_{X\pi}} \\ \bar{F}_{R_{YX}} & \bar{F}_{R_{YY}} & \bar{F}_{R_{YZ}} & \bar{F}_{R_{Y\pi}} \\ \bar{F}_{R_{ZX}} & \bar{F}_{R_{ZY}} & \bar{F}_{R_{ZZ}} & \bar{F}_{R_{Z\pi}} \\ \bar{F}_{R_{\pi X}} & \bar{F}_{R_{\pi Y}} & \bar{F}_{R_{\pi Z}} & \bar{F}_{R_{\pi\pi}} \end{bmatrix} \end{aligned} \quad (5.19)$$

$$\begin{aligned} \bar{F}_{\theta}^{\Delta} &= [\nabla_{\theta}\mu^{\Delta}(\theta)]^T C^{-1} [\nabla_{\theta}\mu^{\Delta}(\theta)], \\ &= \begin{bmatrix} \bar{F}_{R_{XX}}^{\Delta} & \bar{F}_{R_{XY}}^{\Delta} & \bar{F}_{R_{XZ}}^{\Delta} & \bar{F}_{R_{X\pi}}^{\Delta} \\ \bar{F}_{R_{YX}}^{\Delta} & \bar{F}_{R_{YY}}^{\Delta} & \bar{F}_{R_{YZ}}^{\Delta} & \bar{F}_{R_{Y\pi}}^{\Delta} \\ \bar{F}_{R_{ZX}}^{\Delta} & \bar{F}_{R_{ZY}}^{\Delta} & \bar{F}_{R_{ZZ}}^{\Delta} & \bar{F}_{R_{Z\pi}}^{\Delta} \\ \bar{F}_{R_{\pi X}}^{\Delta} & \bar{F}_{R_{\pi Y}}^{\Delta} & \bar{F}_{R_{\pi Z}}^{\Delta} & \bar{F}_{R_{\pi\pi}}^{\Delta} \end{bmatrix} \end{aligned} \quad (5.20)$$

The calculations of the discrete components of the matrix are comparable to eq. 5.7, and presented in [88] and [89].

In this chapter, we examined the prospective precision constraints for TOA and cooperation based on path-of least resistance (received signal strength after shadow

fading) positioning of an endoscopy pill traveling down the human digestive system. We confirmed the likelihood of accomplishing a mean positioning error of 50 mm in the gastrointestinal system. We also confirmed that no more than 10 receivers on the surface of the human body are required to accomplish sufficient positioning precision for pill-based endoscopy. Software model results using Ansys HFSS revealed that accumulating the quantity of surface antennas on the body would have higher effect on the general positioning accuracy. This is also practical, as we only use one pill to perform capsule endoscopy, but we can put multiple sensors on the surface. We also studied the consequence of arbitrariness in impulse response on the positioning precision. In conclusion and keeping real-world concerns in consideration, we make the inference that cooperating surface sensors, using RSS to determine shadow fading, and then determining the location using time of arrival of a pulse transmitted from the capsule will give us the best chance of accurate localization.

Chapter 6: Conclusions and Future Work

In this research we first compared a basic time-domain FDTD simulation for the path loss around the human body in MATLAB with accurate FEM modeling of the human body in ANSYS HFSS. We have shown that the time domain FDTD analysis yields comparable results even when it uses a homogeneous body model and simple boundary conditions. The reason for this important observation is that the diffraction path around the human body is the major propagation path between transmitter and receiver. This study only considers the exterior TX and RX antennas, which are located close to the body. Two key questions needed to be addressed as we continued this study. How close to the body surface can the antennas be positioned in order for this observation to remain true? What happens for two on-body antennas? Is the diffraction (surface wave) path still dominant?

Having successfully verified the solver's accuracy with the narrowband characteristics of the human body channel, we proceeded to check its validity for the wideband characteristics. Hence, a few weeks were spent calibrating the simulation for a free space scenario so that it can be compared to actual measurements. The measurements are made on a network analyzer that makes frequency domain calculations, whose Inverse Fourier Transforms are used to plot the impulse response of the channel. Since the FDTD simulations are already in time domain, the transient effects of the antennas are reflected in the received signal (a problem not seen in the impulse response obtained from the network analyzer data). To try and get rid of these effects of the antenna, the current research involves trying to design a point source with perfect impedance matching so that the side-lobes are minimized.

This setup was used to run wideband simulations for the human body and the TOA results were compared with RSS results. The study conducted in this research verifies that Time of Arrival is a more accurate measure of distance between two sensors in a fading environment than the Received Signal Strength. We first demonstrated by comparing a plot obtained from a published RSS model with our TOA results gathered from simulations run on our proprietary FDTD algorithm, which requires less computational resources than commercially available FEM solvers used for similar simulations. We then verified this observation by using CRLB equations given in the literature and substituting the values obtained from the data of our own FDTD simulations for both RSS and TOA techniques. Finally we investigated possible reasons for the discrepancies between the simulated and calculated values of the variance for TOA and RSS techniques. As discussed in the last section of the previous chapter, the CRLB on the variance of RSS came out to be in the same range as that calculated from the simulations. However the CRLB on the variance TOA came out to be 10^{-12} times less than the standard deviation calculated from the simulations. Reasons for this and other possible causes of error have been examined.

The multipath characteristics of the human body can only be truly modeled with a non-homogenous body model. For future research purposes, work is being done in order to import individual organs to the MATLAB FDTD solver developed by the research team. Once this is achieved and all the organs have been assigned different values of dielectric constants and conductivity, can we see the true multipath effects of the human body.

Further work can be done in order to incorporate Direction of Arrival (DOA) techniques to the existing RSS and TOA algorithms to enhance the accuracy of the localization system. DOA denotes the direction from which usually a propagating wave arrives at a point, where usually a set of sensors are located. This set of sensors forms what is called a sensor array. Often there is the associated technique of beam-forming which estimates the signal from a given direction.

References

- [1] K. Pahlavan and A. H. Levesque, *Wireless Information Networks*, 2nd ed., New York: John Wiley and Sons, 2005.
- [2] T. Sexton, "Channel Modeling and High Speed Data Transmission Performance for the Indoor Radio Channel", PhD Dissertation, 1989
- [3] A. Falsafi, "Comparative Performance Evaluation of Transmission Techniques Applied to Wireless Local Area Networks", PhD Dissertation, 1996
- [4] M. Chase, "Performance of M-ARY CDMA Over Modelled and Measured Indoor Radio Channels", PhD Dissertation, 1993
- [5] Tim Holt, "A Computer Graphics Package for Indoor Radio Channel Simulation Using a 2D Ray Tracing Algorithm", MS Thesis, 1992
- [6] G. Yang, "Performance Evaluation of High Speed Wireless Data Systems Using a 3D Ray Tracing Algorithm", PhD Dissertation 1994
- [7] B. Alavi, "Distance Measurement Error Modeling for Time-of-Arrival Based Indoor Geolocation," Ph.D. Dissertation, Worcester Polytechnic Institute, 2006.
- [8] H. Hatami and K. Pahlavan, "Performance Comparison of RSS and TOA Indoor Geolocation Based on UWB Measurement of Channel Characteristics," *IEEE International Symposium on Personal, Indoor and Mobile Radio Communications*, September, 2006.
- [9] Catovic and Z. Sahinoglu, "The Cramer-Rao Bounds of Hybrid TOA/RSS and TDOA/RSS Location Estimation Schemes," *IEEE Communication Letters*, vol. 8, no. 10, pp 626-628, October, 2005.
- [10] Y. Qi, H. Kobayashi, and H. Suda, "Cramer-Rao Bound for Geolocation in non-line-of-sight Environment," *IEEE Transactions on Wireless Communications*, vol. 5, no. 3, pp 672-681, March 2006.
- [11] S. Gezici et al., "Localization via Ultra-Wideband Radios: A look at Positioning Aspects for Future Sensor Networks," *IEEE Signal Processing Magazine*, vol. 22, no. 4, pp 70-84, July 2005.
- [12] H. Sayed, N. Tarighat, and N. Khajehnouri, "Network-Based Wireless Location: Challenges faced in Developing Techniques Accurate Wireless Location Information," *IEEE Signal Processing Magazine*, vol. 22, no. 4, pp 24-40, July 2005.
- [13] N. Alsindi, X. Li, and K. Pahlavan, "Analysis of TOA Estimation using Wideband Measurements of Indoor Radio Propagations," *IEEE Transactions on Instrumentation and Measurement*, vol. 56, no. 5, pp 1537-1545, October 2007.

- [14] Kamyar Yekeh Yazdandoost, Kamran Sayrafian-Pour, Wen-Bin Yang, John Hagedorn and Judith Terrill, *A Statistical Path Loss Model for Medical Implant Communication Channels*, 2009
- [15] S. Howard and K. Pahlavan, "Measurement and Analysis of the Indoor Radio Channel in the Frequency Domain," *IEEE Transactions on Instrumentation and Measurement*, vol. 39, no. 5, pp 751-755, October 1990
- [16] Bardia Alavi, "Distance Measurement Error Modeling for Time-of-Arrival Based Indoor Geolocation", PhD 2006
- [17] T. Holt, K. Pahlavan, and J. F. Lee, "A Graphical Indoor Radio Channel Simulator using 2D Ray Tracing," *IEEE International Symposium on Personal, Indoor, and Mobile Radio Communications*, pp 411-416, October 1992
- [18] G. Yang, K. Pahlavan, and J. F. Lee, "A 3D Propagation Model with Polarization Characteristics, in Indoor Radio Channel," *IEEE Global Telecommunication conference*, vol. 2, pp 1252-1256, November-December 1993.
- [19] Fardad Askarzadeh, Mohammad Heidari, Sergery Makarov , Kaveh Pahlavan, "Analysis of Effect of Micro-Metal On Ranging Error Using Finite Difference Time Domain Method", 2008 IWCMC.
- [20] J. B. Keller, "Geometric Theory of Diffraction," *J. Opt. Soc. Am.*, vol. 52, pp. 116-130, 1962.
- [21] R. G. Kouyoumjian and P.H. Pathak, "High frequency diffraction, focus on ray methods," *2000 IEEE Antennas and Propagation Society International Symposium*, vol. 3, p. 1638, 16-21 July 2000.
- [22] Henry Bertoni, "08Diffraction.pdf" <http://eeweb.poly.edu/faculty/bertoni/docs/> September 2003
- [23] Henry Bertoni, "09MoreDiff.pdf" <http://eeweb.poly.edu/faculty/bertoni/docs/> September 2003
- [24] Takahiro Aoyagi, Jun-ichi Takada, Kenichi Takizawa, Norihiko Katayama, Takehiko Kobayashi, Kamyar Yekeh Yazdandoost, Huan-bang Li and Ryuji Kohno, *Channel models for wearable and implantable WBANs*, July 2008
- [25] L. Roelens, S. Van den Bulcke, W. Joseph, G. Vermeeren and L. Martens, *Path loss model for wireless narrowband communication above flat phantom*, August 2005
- [26] K. Pahlavan, Nonlinear quantization and multi-level/phase modulation and coding, *IEEE Trans. Commun.*, (1991).
- [27] K. Pahlavan, P. Krishnamurthy and J. Beneat, Wideband radio channel modeling for indoor geolocation applications, *IEEE Commun. Mag.*, 36(4), 60-65(1998).

- [28] B. Alavi, K. Pahlavan, N. Alsindi, and X. Li, "Using UWB Measurements for Statistical Analysis of the Ranging Error in Indoor Multipath Environment," accepted for publication in *International Journal of Wireless and Optical Communications (IJWOC)*, 2006.
- [29] B. Alavi and K. Pahlavan, Modeling of the TOA based Distance Measurement Error Using UWB Indoor Radio Measurements, *IEEE Communication Letters*, Vol. 10, No. 4, pp: 275-277, April 2006. X. Li and K. Pahlavan, Super-resolution TOA estimation with diversity for indoor geolocation, *IEEE Trans. Wireless Commun.*, December. 2003.
- [30] X. Li Super-resolution TOA estimation with diversity.
- [31] K. Yee, "Numerical solutions of initial boundary value problems involving Maxwell's equations in isotropic media," *IEEE Transactions on Antennas and Propagation*, vol. AP-14, pp. 302-307, 1966.
- [32] J. Beneat, K. Pahlavan, and P. Krishnamurthy, "Radio channel characterization for indoor and urban geolocation at different frequencies," in *Proc. IEEE PIMRC*, September 1999.
- [33] B. Alavi, K. Pahlavan, X. Li, and N. Alsindi, "Indoor geolocation distance error modeling with uwb technology," in *Proceedings of IASTED 2nd International Conference on Communication and computer networks CCN 2004*, November 2004.
- [34] A. Taflove, *Computational Electrodynamics, The Finite Difference Time Domain Approach*, Artech House, Norwood, MA, 2001, second ed.
- [35] "Fantastic journey. the economist report," pp. 11–13, 2009.
- [36] K. Arshak and F. Adepoju, "Capsule tracking in the gi tract: A novel microcontroller based solution," in *IEEE sensors applications symposium*, 2006, pp. 186–191.
- [37] X. Wang, M. Meng, M. Mandal, and C. Hu, "A localization method using 3-axis magnetic sensor array system for tracking wireless capsule endoscope," in *Proc. of IEEE/EMBS*, 2006, pp. 2522–2525.
- [38] D. Fischer, R. Schreiber, D. Levi, and R. Eliakim, "Capsule endoscopy: the localization system," *Gastrointestinal endoscopy clinics of north america*, vol. 14, pp. 25–31, 2004.
- [39] K. Arshak and F. Adepoju, "Adaptive linearized methods for tracking a moving telemetry capsule," in *IEEE international symposium on industrial electronics (ISIE)*, June 2007, pp. 4–7.
- [40] J. Bulat, K. Duda, M. Duplaga, R. Fraczek, A. Skalski, M. Socha, P. Turcza, and T. Zielinski, "Data processing tasks in wireless gi endoscopy: Image-based capsule localization and navigation with video compression," in *Proc. of IEEE/EMBS*, 2007, pp. 2815–2818.

- [41] T. S, "Smartpill redefines 'noninvasive'," in *Buffalo physician*, vol. 40, 2006, pp. 13–14.
- [42] J. H, D. Levy, R. Shreiber, A. Glukhovsky, and D. Fisher, "Localization of the given m2a ingestible capsule in the given diagnostic imaging system," in *Gastrointestinal Endoscopy*, vol. 55, 2002, p. AB135.
- [43] L. Wang, C. Hu, L. Tian, M. Li, and M. Q. H, "A novel radio propagation radiation model for localization of the capsule in gi tract," in *IEEE international conference on robotics and biomimetics*, December 19-23, 2009.
- [44] P. Bahl and V. N. Padmanabhan, "Radar: An in-building rf-based user location and tracking system," in *IEEE infocom 2000*, vol. 2, March 2000, pp. 75–84.
- [45] K. Sayrafian-Pour, W.-B. Yang, J. Hagedorn, J. Terrill, and K. Yazdandoost, "A statistical path loss model for medical implant communication channels," in *Personal, Indoor and Mobile Radio Communications, 2009 IEEE 20th International Symposium on*, 13-16 2009, pp. 2995 –2999.
- [46] Astrin and T. Kobayashi, "Channel model for body area network (ban)," April, 2009.
- [47] R. Tesi, A. Taparugssanagorn, and M. Humalainen, "Uwb channel measurement for wireless body area networks," 2008.
- [48] Y. Chen and H. Kobayashi, "Signal strength based indoor geolocation," in *Communications, 2002. ICC 2002. IEEE International Conference on*, vol. 1, 2002, pp. 436 –439.
- [49] H. Terchoune, D. Lautru, A. Gati, A. Cortel Carrasco, M. Fai Wong, J. Wiart, and V. F. Hanna, "On-body radio channel modeling for different human body models using FDTD techniques," vol. 51, no 10, Oct. 2009, pp. 2498-2501.
- [50] A. Taflove, *Computational Electrodynamics, The Finite Difference Time Domain Approach*, Artech House, Norwood, MA, 1995.
- [51] A. Bondeson, T. Rylander and P. Ingelström, *Computational Electromagnetics*, Springer, New York, 2005, Series: Texts in Applied Mathematics, Vol. 51. pp. 58-86.
- [52] C. A. Balanis, *Antenna Theory*, Wiley, New York, 2005, 3rd ed, pp. 468-470.
- [53] D. M. Pozar, *Microwave Engineering*, Wiley, New York, 2005, 3rd ed.
- [54] M. Piket-May, A. Taflove, and J. Baron, "FD-TD modeling of digital signal propagation in 3-D circuits with passive and active loads," *IEEE Trans. Microwave Theory and Techniques*, vol. 42, no. 8, Aug. 1994, pp. 1514 - 1523.

- [55] G. Mur, "Absorbing boundary conditions for the finite-difference approximation of the time-domain electromagnetic field equations," *IEEE Trans. Electromagn. Compat.*, vol. EMC-23, no. 4, pp. 377-382, Nov. 1981.
- [56] K. K. Mei and J. Fang, "Superabsorption – a method to improve absorbing boundary conditions," *IEEE Trans. Antennas and Propagation*, vol. 40, no. 9, Sep. 1992, pp. 1001- 1010.
- [57] J.-P. Bérenger, "A perfectly matched layer for the absorption of electromagnetic waves," *J. Comput. Phys.*, vol. 114, pp. 185–200, Oct. 1994.
- [58] D. S. Katz, E. T. Thiele, and A. Taflove, "Validation and extension to three dimensions of the Berenger PML absorbing boundary condition for FD-TD meshes," *IEEE Microwave and Guided Wave Letters*, vol. 4, no 8, Aug. 1994, pp. 268-270.
- [59] S. Makarov, U. Khan, M. Islam, R. Ludwig and K. Pahlavan "On Accuracy of Simple FDTD Models for the Simulation of Human Body Path Loss" in the *2011 IEEE Sensor Applications Symposium*.
- [60] Y. Wang, R. Fu, Y. Ye, U. Khan and K. Pahlavan "Performance Bounds for RF Positioning of Endoscopy Camera Capsules" in the *IEEE Radio Wireless Week 2011*
- [61] F. Askarzadeh, Y. Ye, U. Khan, F. Akgul, K. Pahlavan and S. Makarov "Computational Methods for Localization," Chapter for *Position Location – Theory, Practice and Advances: A handbook for Engineers and Academics By S. Zekavat and M. Beuhrer*.
- [62] H. Mahboubi, K. Moezzi, A. G. Aghdam, K. Sayrafian-Pour and V. Marbukh, "Distributed Deployment Algorithms for Improved Coverage in a Network of Wireless Mobile Sensors," in *IEEE Transactions on Industrial Informatics*, vol. 10, no. 1, pp. 163-174, Feb. 2014.
- [63] Makoto Kawasaki, Ryuji Kohno "A TOA based Positioning Technique of Medical Implanted Devices," *Third International Symposium on Medical Information & Communication Technology*. February 2009
- [64] K. Pahlavan, F. Akgul, Y. Ye, T. Morgan, F. A.-Shabdiz, M. Heidari, C. Steger, "Taking Positioning Indoors: Wi-Fi Localization and GNSS", *Inside GNSS*, vol. 5, no. 3, May, 2010
- [65] J. Oh, S. K. Shah, X. Yuan, and S. J. Tang, Automatic classification of digestive organs in wireless capsule endoscopy videos, In The 22nd Annual ACM Symposium on Applied Computing, SAC07, Soul, 2007.

- [66] Sae Hwang, JungHwan Oh, Jay Cox, Shou Jiang Tang, Harry F. Tibbals, "Blood detection in wireless capsule endoscopy using expectation maximization clustering," Proc. SPIE 6144, Medical Imaging 2006: Image Processing, 61441P (10 March 2006);
- [67] M. Frisch, A. Glukhovsky, and D. Levy, Array system and method for locating an in vivo signal source, Patent US2002/0 173 718, May 20, 2002.
- [68] Gralnek, I. M., Defranchis, R., Seidman, E., Leighton, J. A., Legnani, P. and Lewis, B. S. (2008), Development of a capsule endoscopy scoring index for small bowel mucosal inflammatory change. *Alimentary Pharmacology & Therapeutics*, 27: 146–154.
- [69] de Franchis, R., Eisen, G. M., Laine, L., Fernandez-Urien, I., Herrerias, J. M., Brown, R. D., Fisher, L., Vargas, H. E., Vargo, J., Thompson, J. and Eliakim, R. (2008), Esophageal capsule endoscopy for screening and surveillance of esophageal varices in patients with portal hypertension. *Hepatology*, 47: 1595–1603.
- [70] J. R. R. Kuth and R. Rockelein, Method for determining the position and orientation of an endoscopy capsule guided through an examination object by using a navigating magnetic field generated by means of a navigation device, Patent, February 15, 2007.
- [71] Koizuka, N., Imai, R., Fujimoto, H., Hayakawa, T., Kimura, Y., Kohno-Murase, J., Sakai, T., Kawasaki, S. and Imamura, J. (2003), Genetic characterization of a pentatricopeptide repeat protein gene, *orf687*, that restores fertility in the cytoplasmic male-sterile Kosena radish. *The Plant Journal*, 34: 407–415.
- [72] M. Q. M. Chao Hu and M. Mandal, Efficient magnetic localization and orientation technique for capsule endoscopy, In *Intelligent Robots and Systems*, 2005. (IROS 2005), 2005.
- [73] A. M. Gastone Ciutia, P. Valdastrina, and P. Darioa, Robotic magnetic steering and locomotion of microsystems for diagnostic and surgical endoluminal procedures, In *Robotica*, 2009.
- [74] S. Thomas, Smartpill redefines ‘noninvasive’, *Buffalo Physician*, Vol. 40, pp. 13–14, 2006.
- [75] M. Pourhomayoun, M. Fowler and Z. Jin, "A novel method for medical implant in-body localization," *2012 Annual International Conference of the IEEE Engineering in Medicine and Biology Society*, San Diego, CA, 2012, pp. 5757-5760
- [76] Guobing Pan and Litong Wang, "Swallowable Wireless Capsule Endoscopy: Progress and Technical Challenges," *Gastroenterology Research and Practice*, vol. 2012, Article ID 841691, 9 pages, 2012.

- [77] K. Arshak, E. Jafer, G. Lyons, D. Morris, O. Korostynska, (2004) "A review of low-power wireless sensor microsystems for biomedical capsule diagnosis", *Microelectronics International*, Vol. 21 Issue: 3, pp.8-19
- [78] W. B. Yang and K. Sayrafian-Pour, "Interference mitigation for body area networks," *2011 IEEE 22nd International Symposium on Personal, Indoor and Mobile Radio Communications*, Toronto, ON, 2011, pp. 2193-2197.Y.
- [79] N. Alsindi and K. Pahlavan, Cooperative localization bounds for indoor ultra-wideband wireless sensor networks, *EURASIP Journal on Advances in Signal Processing*, Vol. 2008, pp. 125:1–125:13, January 2008. doi:10.1155/2008/852509
- [80] N. Bargshady, K. Pahlavan, Y. Ye, F. Akgul, and N. Alsindi, Bounds on performance of hybrid WiFi-UWB cooperative localization for robotic applications, In *Proceedings of IEEE International Symposium on Personal, Indoor and Mobile Radio Communications (PIMRC10)*, 2010
- [81] ANSYS Full-wave electromagnetic field simulation, <http://www.ANSYS.com/products/hf/hfss/>, Online; accessed 27 September 2010
- [82] N. Patwari and A. Hero, Signal strength localization bounds in ad hoc and sensor networks when transmit powers are random, In *Fourth IEEE Workshop on Sensor Array and Multichannel Processing*, 2006, July 2006, pp. 299–303
- [83] K. Y. Y. H.-B. Li and B. Zhen, *Wireless body area network*. River Publishers, 2010
- [84] N. Patwari, I. Hero, A.O., M. Perkins, N. Correal, and R. O’Dea, Relative location estimation in wireless sensor networks, In *IEEE Transactions on Signal Processing*, August 2003, pp. 2137–2148
- [85] K. Duda, T. Zielinski, R. Fraczek, J. Bulat and M. Duplaga, "Localization of Endoscopic Capsule in the GI Tract Based on MPEG-7 Visual Descriptors," *2007 IEEE International Workshop on Imaging Systems and Techniques*, Krakow, 2007, pp. 1-4.
- [86] H. L. V. Trees, *Detection, Estimation, and Modulation Theory: Part I*, Wiley, New York, 1968
- [87] Y. Ephraim and H. L. Van Trees, "A signal subspace approach for speech enhancement," in *IEEE Transactions on Speech and Audio Processing*, vol. 3, no. 4, pp. 251-266, Jul 1995
- [88] K. G. P. Swar, Y. Ye, and K. Pahlavan, On effect of transmit power variance on localization accuracy in wireless capsule endoscopy, In *IEEE Wireless Communications and Networking Conference (WCNC 2012)*, Paris, 2012.

- [89] G. Bao, L. Mi, Y. Geng, M. Zhou and K. Pahlavan, "A video-based speed estimation technique for localizing the wireless capsule endoscope inside gastrointestinal tract," *2014 36th Annual International Conference of the IEEE Engineering in Medicine and Biology Society*, Chicago, IL, 2014, pp. 5615-5618.
- [90] Rondonotti, E., M. Pennazio, E. Toth, P. Menchen, M.E. Riccioni, G.D. De Palma, F. Scotto, et al. 2008. "Small-bowel Neoplasms in Patients Undergoing Video Capsule Endoscopy: a Multicenter European Study." *Endoscopy* 40 (6): 488–495.
- [91] H. Keller, "Method for navigation and control of a magnetically guided capsule endoscope in the human stomach," *2012 4th IEEE RAS & EMBS International Conference on Biomedical Robotics and Biomechatronics (BioRob)*, Rome, 2012, pp. 859-865.
- [92] C. Hu, M. Q. h. Meng and M. Mandal, "The Calibration of 3-Axis Magnetic Sensor Array System for Tracking Wireless Capsule Endoscope," *2006 IEEE/RSJ International Conference on Intelligent Robots and Systems*, Beijing, 2006, pp. 162-167.
- [93] G. Ciuti, A. Menciassi and P. Dario, "Capsule Endoscopy: From Current Achievements to Open Challenges," in *IEEE Reviews in Biomedical Engineering*, vol. 4, pp. 59-72, 2011.
- [94] Timm, D., Willis, H., Thomas, W., Sanders, L., Boileau, T., & Slavin, J. (2011). The use of a wireless motility device (SmartPill®) for the measurement of gastrointestinal transit time after a dietary fibre intervention. *British Journal of Nutrition*, 105(9), 1337-1342.
- [95] M. Pourhomayoun, Z. Jin and M. L. Fowler, "Accurate Localization of In-Body Medical Implants Based on Spatial Sparsity," in *IEEE Transactions on Biomedical Engineering*, vol. 61, no. 2, pp. 590-597, Feb. 2014.
- [96] Yinping Zhang, Guobing Zhou, Kunping Lin, Qunli Zhang, Hongfa Di, Application of latent heat thermal energy storage in buildings: State-of-the-art and outlook, *Building and Environment*, Volume 42, Issue 6, 2007, Pages 2197-2209
- [97] Khalil Arshak, Francis Adepoju & David Waldron (2013) A Review and Adaptation of Methods of Object Tracking to Telemetry Capsules, *International Journal of Intelligent Computing in Medical Sciences & Image Processing*, 1:1, 35-46
- [98] Yang WB., Sayrafian-Pour K. (2013) Theoretical Analysis and Modeling of Link Adaptation Schemes in Body Area Networks. In: Godara B., Nikita K.S. (eds) *Wireless Mobile Communication and Healthcare. MobiHealth 2012. Lecture Notes of the Institute for Computer Sciences, Social Informatics and Telecommunications Engineering*, vol 61.

- [99] Y. Ye, U. Khan, N. Alsindi, R. Fu and K. Pahlavan, "On the accuracy of RF positioning in multi-Capsule endoscopy," *2011 IEEE 22nd International Symposium on Personal, Indoor and Mobile Radio Communications*, Toronto, ON, 2011, pp. 2173-2177.
- [100] N. A. Alsindi, B. Alavi and K. Pahlavan, "Measurement and Modeling of Ultrawideband TOA-Based Ranging in Indoor Multipath Environments," in *IEEE Transactions on Vehicular Technology*, vol. 58, no. 3, pp. 1046-1058, March 2009.
- [101] N. Bargshady, K. Pahlavan and N. A. Alsindi, "Hybrid WiFi/UWB, cooperative localization using Particle Filter," *2015 International Conference on Computing, Networking and Communications (ICNC)*, Garden Grove, CA, 2015, pp. 1055-1060.
- [102] M. A. Ismail, D. Smith, A. Panariello, Ying Wang and Ming Yu, "EM-based design of large-scale dielectric-resonator filters and multiplexers by space mapping," in *IEEE Transactions on Microwave Theory and Techniques*, vol. 52, no. 1, pp. 386-392, Jan. 2004.
- [103] N. Patwari and A. O. Hero, "Signal Strength Localization Bounds in Ad Hoc and Sensor Networks when Transmit Powers are Random," *Fourth IEEE Workshop on Sensor Array and Multichannel Processing, 2006.*, Waltham, MA, 2006, pp. 299-303.
- [104] H. B. Li, K. i. Takizawa, B. Zhen and R. Kohno, "Body Area Network and Its Standardization at IEEE 802.15.MBAN," *2007 16th IST Mobile and Wireless Communications Summit*, Budapest, 2007, pp. 1-5.
- [105] N. Patwari, Yanwei Wang and R. J. O'Dea, "The importance of the multipoint-to-multipoint indoor radio channel in ad hoc networks," *2002 IEEE Wireless Communications and Networking Conference Record. WCNC 2002 (Cat. No.02TH8609)*, 2002, pp. 608-612 vol.2.
- [106] K. Duda, T. Zielinski and M. Duplaga, "Computationally simple Super-Resolution algorithm for video from endoscopic capsule," *2008 International Conference on Signals and Electronic Systems*, Krakow, 2008, pp. 197-200.

Appendix 1: MATLAB Code for FDTD in XZ Plane

```

% 3D FDTD - ECE539
% First-order ABCs
tic
clear all;
eps0      = 8.85418782e-012;      % ANSYS HFSS value
mu0       = 1.25663706e-006;     % ANSYS HFSS value
c0        = 1/sqrt(eps0*mu0);    % ANSYS HFSS value

scrsz     = get(0,'ScreenSize');
figure('Position',[0.05*scrsz(3) 0.05*scrsz(4) 0.8*scrsz(3)
0.8*scrsz(4)]);
colormap(jet(128));
load body;
load structure;
%-----
%-----
% 3D geometry definitions and magic time step
%-----
%-----
Nx  = length(x) - 1;  % Nx
Ny  = length(y) - 1;  % Ny
Nz  = length(z) - 1;  % Nz
dt  = 1/(c0*sqrt(1/d^2 + 1/d^2 + 1/d^2));% Magic time step
%-----
%-----
% Excitation - voltage(s)
%-----
%-----
f = 402e6;
% (to travel from feed to the
end)
T = 15e-9; % observation time
% Number of time steps and time vector
NT = round(T/dt); t = [0: dt: NT*dt];
% Excitation (generator) voltage
VG = sin(2*pi*f*t);
IG = zeros(size(VG));
RG = 50;
bound = 2*ones(1, NT+1); % graphics scale
%-----
%-----
% Allocate field matrices
%-----
%-----
Ex = zeros(Nx , Ny+1, Nz+1);
Ey = zeros(Nx+1, Ny , Nz+1);
Ez = zeros(Nx+1, Ny+1, Nz );
Hx = zeros(Nx+1, Ny , Nz );
Hy = zeros(Nx , Ny+1, Nz );
Hz = zeros(Nx , Ny , Nz+1);
% To distinguish between next and past updates (for BCs)
temp1 = Ey(2, :, :); temp2 = Ez(2, :, :);

```

```

temp3 = Ey(Nx, :, :);    temp4 = Ez(Nx, :, :);
temp5 = Ex(:, 2, :);    temp6 = Ez(:, 2, :);
temp7 = Ex(:, Ny, :);   temp8 = Ez(:, Ny, :);
temp9 = Ex(:, :, 2);    temp10 = Ey(:, :, 2);
temp11 = Ex(:, :, Nz);  temp12 = Ey(:, :, Nz);

%-----
% Position of the excitation source
%-----

XE = -0.2; YE = 0; ZE = -0.2; % coordinates
[dummy, k_e] = min(abs(x-XE)); % index of the excitation node (exp.
with Nx/2)
[dummy, m_e] = min(abs(y-YE)); % index of the excitation node (exp.
with Nx/2)
[dummy, p_e] = min(abs(z-ZE)); % index of the excitation node (exp.
with Nx/2)
%-----
% Position of the receiver source
%-----

XR = +0.2; YR = 0; ZR = -0.2; % coordinates
[dummy, k_e1] = min(abs(x-XR)); % index of the excitation node
(exp. with Nx/2)
[dummy, m_e1] = min(abs(y-YR)); % index of the excitation node
(exp. with Nx/2)
[dummy, p_e1] = min(abs(z-ZR)); % index of the excitation node
(exp. with Nx/2)
%-----

%-----
% Antenna metal boundaries
%-----

N = 4; % length of one wing (the length is N*d; the dipole
length is (2*N+1)*d)
% TX
MetalRectX = k_e*ones(1,2*N); % x-position of
metal rectangles
MetalRectZ = [p_e-N:p_e-1 p_e+1:p_e+N]; % z-position of
metal rectangles
XVR = [];
YVR = [];
for m = 1:length(MetalRectX)
    xmin_ = xmin + (MetalRectX(m)-1.5)*d;
    xmax_ = xmin_ + d;
    zmin_ = zmin + (MetalRectZ(m)-1.5)*d;
    zmax_ = zmin_ + d;
    XVR(:, m) = [xmin_ xmin_ xmax_ xmax_ xmin_];
    ZVR(:, m) = [zmin_ zmax_ zmax_ zmin_ zmin_];
end
% RX
MetalRectX1 = k_e1*ones(1,2*N); % x-positon of metal
rectangles
MetalRectZ1 = [p_e1-N:p_e1-1 p_e1+1:p_e+N]; % z-position of
metal rectangles
for m = 1:length(MetalRectX1)
    xmin_ = xmin + (MetalRectX1(m)-1.5)*d;

```

```

xmax_      = xmin_ + d;
zmin_      = zmin + (MetalRectZ1(m)-1.5)*d;
zmax_      = zmin_ + d;
XVR(:, m+length(MetalRectX)) = [xmin_ xmin_ xmax_ xmax_ xmin_];
ZVR(:, m+length(MetalRectX)) = [zmin_ zmax_ zmax_ zmin_ zmin_];
end

%-----
%-----
% Difference coefficients/dielectric boundaries - Matrix DIEEL
%-----
sigmae = SIGMA;
sigmah = 0;
eps     = eps0*EPS;
%-----
e1      = (1 - dt*sigmae./(2*eps))./(1 + dt*sigmae./(2*eps));
e2      = (dt./(d*eps))./(1 + dt*sigmae./(2*eps));
e3      = (dt./(d*eps))./(1 + dt*sigmae./(2*eps));
h1      = (1 - dt*sigmah/(2*mu0))./(1 + dt*sigmah/(2*mu0));
h2      = (dt/(d*mu0))./(1 + dt*sigmah/(2*mu0));

sigma   = d/(d*d*RG);
es1     = (1 - dt*sigma/(2*eps0))/(1 + dt*sigma/(2*eps0));
es2     = (dt/(d*eps0))/(1 + dt*sigma/(2*eps0));
es3     = (dt*sigma/(d*eps0))/(1 + dt*sigma/(2*eps0));

Ind     = SIGMA(2:Nx,2:Ny,1:Nz);

%-----
% Main loop - "bootstrapping" (initial conditions are zeros)
%-----
n = 2; hr = []; hrd = []; VLoad = zeros(size(t));
tic
while n < NT+1
    %-----
    % To distinguish between next and past updates (BCs and the
    source)
    temp1 = Ey(2, :, :);    temp2 = Ez(2, :, :);
    temp3 = Ey(Nx, :, :);   temp4 = Ez(Nx, :, :);
    temp5 = Ex(:, 2, :);    temp6 = Ez(:, 2, :);
    temp7 = Ex(:, Ny, :);   temp8 = Ez(:, Ny, :);
    temp9 = Ex(:, :, 2);    temp10 = Ey(:, :, 2);
    temp11 = Ex(:, :, Nz);  temp12 = Ey(:, :, Nz);
    temp   = Ez(k_e, m_e, p_e);
    temp1  = Ez(k_e1, m_e1, p_e1);
    %-----
    % E-update (everywhere except on boundary; (40% of time))
    Ex(:, 2:Ny, 2:Nz) = e1(1:Nx, 2:Ny, 2:Nz) .* Ex(:, 2:Ny, 2:Nz) +
e2(1:Nx, 2:Ny, 2:Nz) .* (diff(Hz(:, :, 2:Nz), 1, 2) - diff(Hy(:, 2:Ny, :), 1, 3));
    Ey(2:Nx, :, 2:Nz) = e1(2:Nx, 1:Ny, 2:Nz) .* Ey(2:Nx, :, 2:Nz) +
e2(2:Nx, 1:Ny, 2:Nz) .* (diff(Hx(2:Nx, :, :), 1, 3) - diff(Hz(:, :, 2:Nz), 1, 1));
    Ez(2:Nx, 2:Ny, :) = e1(2:Nx, 2:Ny, 1:Nz) .* Ez(2:Nx, 2:Ny, :) +
e2(2:Nx, 2:Ny, 1:Nz) .* (diff(Hy(:, 2:Ny, :), 1, 1) - diff(Hx(2:Nx, :, :), 1, 2));
    %-----

```

```

%-----
m1      = (c0*dt - d)/(c0*dt + d);
% Radiation BCs (Mur 1981, first order)
% Left
Ey(1, :, :) = temp1 + m1*(Ey(2, :, :) - Ey(1, :, :)); % left -
Ey;
Ez(1, :, :) = temp2 + m1*(Ez(2, :, :) - Ez(1, :, :)); % left -
Ez;
% Right
Ey(Nx+1, :, :) = temp3 + m1*(Ey(Nx, :, :) - Ey(Nx+1, :, :)); % right
- Ey;
Ez(Nx+1, :, :) = temp4 + m1*(Ez(Nx, :, :) - Ez(Nx+1, :, :)); % right
- Ez;
% Front
Ex(:, 1, :) = temp5 + m1*(Ex(:, 2, :) - Ex(:, 1, :)); %
front - Ex;
Ez(:, 1, :) = temp6 + m1*(Ez(:, 2, :) - Ez(:, 1, :)); %
front - Ez;
% Rear
Ex(:, Ny+1, :) = temp7 + m1*(Ex(:, Ny, :) - Ex(:, Ny+1, :)); % rear
- Ex;
Ez(:, Ny+1, :) = temp8 + m1*(Ez(:, Ny, :) - Ez(:, Ny+1, :)); % rear
- Ey;
% Bottom
Ex(:, :, 1) = temp9 + m1*(Ex(:, :, 2) - Ex(:, :, 1)); %
bottom - Ex;
Ey(:, :, 1) = temp10 + m1*(Ey(:, :, 2) - Ey(:, :, 1)); %
bottom - Ey;
% Top
Ex(:, :, Nz+1) = temp11 + m1*(Ex(:, :, Nz) - Ex(:, :, Nz+1)); %
top - Ex;
Ey(:, :, Nz+1) = temp12 + m1*(Ey(:, :, Nz) - Ey(:, :, Nz+1)); %
top - Ex;
%-----
% Feed model - TX -lumped port
% Voltage source
Ez(k_e, m_e, p_e) =          es1 * temp+...
                          es2 *(Hy(k_e, m_e, p_e) - Hy(k_e-1, m_e,
p_e) -...
                          Hx(k_e, m_e, p_e) + Hx(k_e, m_e-1,
p_e))-...
                          es3 *(VG(n) + VG(n-1))/2;
IG(n)                = (d/RG) * Ez(k_e, m_e, p_e) + VG(n)/RG ;

Ez(MetalRectX, m_e, MetalRectZ) = 0;          % top/bottom
wings

%-----
% Feed model - RX -lumped load
Ez(k_e1, m_e1, p_e1) =          es1 * temp1+...
                          es2 *(Hy(k_e1, m_e1, p_e1) - Hy(k_e1-
1, m_e1, p_e1) -...
                          Hx(k_e1, m_e1, p_e1) + Hx(k_e1,
m_e1-1, p_e1));
IG(n)                = (d/RG) * Ez(k_e1, m_e1, p_e1);
VLoad(n)              = RG*IG(n);

```



```

Ez(MetalRectX1, m_e, MetalRectZ) = 0; % top/bottom
wings

%-----
% H-update (40% of time)
Hx = h1*Hx + h2*diff(Ey,1,3)- h2*diff(Ez,1,2);
Hy = h1*Hy + h2*diff(Ez,1,1)- h2*diff(Ex,1,3);
Hz = h1*Hz + h2*diff(Ex,1,2)- h2*diff(Ey,1,1);
%-----
% Energy(n) = TotalEnergy3D(Ex, Ey, Ez, Hx, Hy, Hz, d, eps, mu);
n = n + 1;
%-----
% Scale/Plot fields
output = squeeze(Ez(:, m_e, :));
output = abs(output).^0.20.*sign(output);
output(1,1) = -bound(n);
output(end,end) = +bound(n);

if (~isempty(hr)) delete(hr); end;
if (~isempty(hrd)) delete(hrd); end;

subplot(2,2,[1 3])
imagesc( [x(1) x(end)], [z(1) z(end-1)], output'); %
main field
NN = 3; line(xb(1:NN:end), zb(1:NN:end), 'LineStyle','.') %
body shape
hr = patch(XVR, ZVR, [0.5 0.5 0.5]);
string = strcat(num2str(1e9*t(n)), ' ns');
axis 'equal'; axis 'tight', set(gca, 'YDir', 'normal');
xlabel('x, m'); ylabel('z, m');
title(strcat('FDTD Simulation: Electric field at t=', string),
'FontSize', 16);
subplot(2,2,2)
plot(t*1e9, VG, 'b', t(1:n)*1e9, VLoad(1:n)*1e3, 'r'); grid on;
title ('Received voltage (red, mV) vs. TX voltage (blue, V)',
'FontSize', 16);
xlabel('time, ns');
subplot(2,2,4)
plot(t*1e9, VG, 'b', t(1:n)*1e9, VLoad(1:n)*1e3, 'r'); grid on;
title ('Received voltage (red, mV) vs. TX voltage (blue, V)',
'FontSize', 16);
xlabel('time, ns');
drawnow;
%-----
end
toc

```

Appendix 2: MATLAB Code for FDTD in YZ Plane

```

% 3D FDTD - ECE539
% First-order ABCs
tic
clear all;
eps0      = 8.85418782e-012;      % ANSYS HFSS value
mu0       = 1.25663706e-006;     % ANSYS HFSS value
c0        = 1/sqrt(eps0*mu0);    % ANSYS HFSS value

scrsz      = get(0, 'ScreenSize');
figure('Position', [0.05*scrsz(3) 0.05*scrsz(4) 0.8*scrsz(3)
0.8*scrsz(4)]);
colormap(jet(128));
load body;
load structure;
%-----
%-----
% 3D geometry definitions and magic time step
%-----
%-----
Nx  = length(x) - 1; % Nx
Ny  = length(y) - 1; % Ny
Nz  = length(z) - 1; % Nz
dt  = 1/(c0*sqrt(1/d^2 + 1/d^2 + 1/d^2)); % Magic time step
%-----
%-----
% Excitation - voltage(s)
%-----
%-----
f = 402e6;
% (to travel from feed to the
end)
T      = 15e-9; % observation time
% Number of time steps and time vector
NT = round(T/dt); t = [0: dt: NT*dt];
% Excitation (generator) voltage
VG = sin(2*pi*f*t);
IG = zeros(size(VG));
RG = 50;
bound = 2*ones(1, NT+1); % graphics scale
%-----
%-----
% Allocate field matrices
%-----
%-----
Ex = zeros(Nx , Ny+1, Nz+1);
Ey = zeros(Nx+1, Ny , Nz+1);
Ez = zeros(Nx+1, Ny+1, Nz );
Hx = zeros(Nx+1, Ny , Nz );
Hy = zeros(Nx , Ny+1, Nz );
Hz = zeros(Nx , Ny , Nz+1);
% To distinguish between next and past updates (for BCs)

```

```

temp1 = Ey(2, :, :);      temp2 = Ez(2, :, :);
temp3 = Ey(Nx, :, :);    temp4 = Ez(Nx, :, :);
temp5 = Ex(:, 2, :);     temp6 = Ez(:, 2, :);
temp7 = Ex(:, Ny, :);    temp8 = Ez(:, Ny, :);
temp9 = Ex(:, :, 2);     temp10 = Ey(:, :, 2);
temp11 = Ex(:, :, Nz);   temp12 = Ey(:, :, Nz);

%-----
% Position of the excitation source
%-----

XE = 0.0; YE = -0.2; ZE = -0.2; % coordinates
[dummy, k_e] = min(abs(x-XE)); % index of the excitation node (exp.
with Nx/2)
[dummy, m_e] = min(abs(y-YE)); % index of the excitation node (exp.
with Nx/2)
[dummy, p_e] = min(abs(z-ZE)); % index of the excitation node (exp.
with Nx/2)
%-----
% Position of the receiver source
%-----

XR = 0.0; YR = +0.2; ZR = -0.2; % coordinates
[dummy, k_e1] = min(abs(x-XR)); % index of the excitation node
(exp. with Nx/2)
[dummy, m_e1] = min(abs(y-YR)); % index of the excitation node
(exp. with Nx/2)
[dummy, p_e1] = min(abs(z-ZR)); % index of the excitation node
(exp. with Nx/2)
%-----

%-----
% Antenna metal boundaries
%-----

N = 4; % length of one wing (the length is N*d; the dipole
length is (2*N+1)*d)
% TX
MetalRectX = m_e*ones(1,2*N); % y-position of
metal rectangles
MetalRectZ = [p_e-N:p_e-1 p_e+1:p_e+N]; % z-position of
metal rectangles
XVR = [];
YVR = [];
for m = 1:length(MetalRectX)
    xmin_ = xmin + (MetalRectX(m)-1.5)*d;
    xmax_ = xmin_ + d;
    zmin_ = zmin + (MetalRectZ(m)-1.5)*d;
    zmax_ = zmin_ + d;
    XVR(:, m) = [xmin_ xmin_ xmax_ xmax_ xmin_];
    ZVR(:, m) = [zmin_ zmax_ zmax_ zmin_ zmin_];
end
% RX
MetalRectX1 = m_e1*ones(1,2*N); % y-positon of metal
rectangles
MetalRectZ1 = [p_e1-N:p_e1-1 p_e1+1:p_e+N]; % z-position of
metal rectangles
for m = 1:length(MetalRectX1)

```

```

xmin_      = xmin + (MetalRectX1(m)-1.5)*d;
xmax_      = xmin_ + d;
zmin_      = zmin + (MetalRectZ1(m)-1.5)*d;
zmax_      = zmin_ + d;
XVR(:, m+length(MetalRectX)) = [xmin_ xmin_ xmax_ xmax_ xmin_];
ZVR(:, m+length(MetalRectX)) = [zmin_ zmax_ zmax_ zmin_ zmin_];
end

%-----
%
% Difference coefficients/dielectric boundaries - Matrix DIEL
%-----
sigmae = SIGMA;
sigmah = 0;
eps     = eps0*EPS;
%-----
e1      = (1 - dt*sigmae./(2*eps))./(1 + dt*sigmae./(2*eps));
e2      = (dt./(d*eps))./(1 + dt*sigmae./(2*eps));
e3      = (dt./(d*eps))./(1 + dt*sigmae./(2*eps));
h1      = (1 - dt*sigmah/(2*mu0))./(1 + dt*sigmah/(2*mu0));
h2      = (dt/(d*mu0))./(1 + dt*sigmah/(2*mu0));

sigma   = d/(d*d*RG);
es1     = (1 - dt*sigma/(2*eps0))/(1 + dt*sigma/(2*eps0));
es2     = (dt/(d*eps0))/(1 + dt*sigma/(2*eps0));
es3     = (dt*sigma/(d*eps0))/(1 + dt*sigma/(2*eps0));

Ind     = SIGMA(2:Nx, 2:Ny, 1:Nz);

%-----
% Main loop - "bootstrapping" (initial conditions are zeros)
%-----
n = 2; hr = []; hrd = []; VLoad = zeros(size(t));
tic
while n < NT+1
    %-----
    % To distinguish between next and past updates (BCs and the
    source)
    temp1 = Ey(2, :, :);    temp2 = Ez(2, :, :);
    temp3 = Ey(Nx, :, :);   temp4 = Ez(Nx, :, :);
    temp5 = Ex(:, 2, :);    temp6 = Ez(:, 2, :);
    temp7 = Ex(:, Ny, :);   temp8 = Ez(:, Ny, :);
    temp9 = Ex(:, :, 2);    temp10 = Ey(:, :, 2);
    temp11 = Ex(:, :, Nz);  temp12 = Ey(:, :, Nz);
    temp   = Ez(k_e, m_e, p_e);
    temp1  = Ez(k_e1, m_e1, p_e1);
    %-----
    % E-update (everywhere except on boundary; (40% of time))
    Ex(:, 2:Ny, 2:Nz) = e1(1:Nx, 2:Ny, 2:Nz).*Ex(:, 2:Ny, 2:Nz) +
e2(1:Nx, 2:Ny, 2:Nz).*(diff(Hz(:, :, 2:Nz), 1, 2) - diff(Hy(:, 2:Ny, :), 1, 3));
    Ey(2:Nx, :, 2:Nz) = e1(2:Nx, 1:Ny, 2:Nz).*Ey(2:Nx, :, 2:Nz) +
e2(2:Nx, 1:Ny, 2:Nz).*(diff(Hx(2:Nx, :, :), 1, 3) - diff(Hz(:, :, 2:Nz), 1, 1));
    Ez(2:Nx, 2:Ny, :) = e1(2:Nx, 2:Ny, 1:Nz).*Ez(2:Nx, 2:Ny, :) +
e2(2:Nx, 2:Ny, 1:Nz).*(diff(Hy(:, 2:Ny, :), 1, 1) - diff(Hx(2:Nx, :, :), 1, 2));

```

```

%-----
%
m1      = (c0*dt - d)/(c0*dt + d);
% Radiation BCs (Mur 1981, first order)
% Left
Ey(1, :, :) = temp1 + m1*(Ey(2, :, :) - Ey(1, :, :)); % left -
Ey;
Ez(1, :, :) = temp2 + m1*(Ez(2, :, :) - Ez(1, :, :)); % left -
Ez;
% Right
Ey(Nx+1, :, :) = temp3 + m1*(Ey(Nx, :, :) - Ey(Nx+1, :, :)); % right
- Ey;
Ez(Nx+1, :, :) = temp4 + m1*(Ez(Nx, :, :) - Ez(Nx+1, :, :)); % right
- Ez;
% Front
Ex(:, 1, :) = temp5 + m1*(Ex(:, 2, :) - Ex(:, 1, :)); %
front - Ex;
Ez(:, 1, :) = temp6 + m1*(Ez(:, 2, :) - Ez(:, 1, :)); %
front - Ez;
% Rear
Ex(:, Ny+1, :) = temp7 + m1*(Ex(:, Ny, :) - Ex(:, Ny+1, :)); % rear
- Ex;
Ez(:, Ny+1, :) = temp8 + m1*(Ez(:, Ny, :) - Ez(:, Ny+1, :)); % rear
- Ez;
% Bottom
Ex(:, :, 1) = temp9 + m1*(Ex(:, :, 2) - Ex(:, :, 1)); %
bottom - Ex;
Ey(:, :, 1) = temp10 + m1*(Ey(:, :, 2) - Ey(:, :, 1)); %
bottom - Ey;
% Top
Ex(:, :, Nz+1) = temp11 + m1*(Ex(:, :, Nz) - Ex(:, :, Nz+1)); %
top - Ex;
Ey(:, :, Nz+1) = temp12 + m1*(Ey(:, :, Nz) - Ey(:, :, Nz+1)); %
top - Ez;
%-----
% Feed model - TX -lumped port
% Voltage source
Ez(k_e, m_e, p_e) =          es1 * temp+...
                          es2 *(Hy(k_e, m_e, p_e) - Hy(k_e-1, m_e,
p_e) -...
                          Hx(k_e, m_e, p_e) + Hx(k_e, m_e-1,
p_e))-...
                          es3 *(VG(n) + VG(n-1))/2;
IG(n)          = (d/RG) * Ez(k_e, m_e, p_e) + VG(n)/RG ;

Ez(MetalRectX, m_e, MetalRectZ) = 0;          % top/bottom
wings

%-----
% Feed model - RX -lumped load
Ez(k_e1, m_e1, p_e1) =          es1 * temp1+...
                          es2 *(Hy(k_e1, m_e1, p_e1) - Hy(k_e1-
1, m_e1, p_e1) -...
                          Hx(k_e1, m_e1, p_e1) + Hx(k_e1,
m_e1-1, p_e1));
IG(n)          = (d/RG) * Ez(k_e1, m_e1, p_e1);

```

```

VLoad(n)          = RG*IG(n);

Ez(MetalRectX1, m_e, MetalRectZ) = 0;           % top/bottom
wings

%-----
% H-update (40% of time)
Hx = h1*Hx + h2*diff(Ey,1,3)- h2*diff(Ez,1,2);
Hy = h1*Hy + h2*diff(Ez,1,1)- h2*diff(Ex,1,3);
Hz = h1*Hz + h2*diff(Ex,1,2)- h2*diff(Ey,1,1);
%-----
% Energy(n) = TotalEnergy3D(Ex, Ey, Ez, Hx, Hy, Hz, d, eps, mu);
n = n + 1;
%-----
% Scale/Plot fields

output          = squeeze(Ez(k_e, :, :));
output          = abs(output).^0.20.*sign(output);
output(1,1)     = -bound(n);
output(end,end) = +bound(n);

if (~isempty(hr)) delete(hr); end;
if (~isempty(hrd)) delete(hrd); end;

subplot(2,2,[1 3])
imagec( [x(1) x(end)], [z(1) z(end-1)], output'); %
main field
NN = 3; line(yb(1:NN:end), zb(1:NN:end), 'LineStyle','.') %
body shape
hr = patch(XVR, ZVR, [0.5 0.5 0.5]);
string = strcat(num2str(1e9*t(n)), ' ns');
axis 'equal'; axis 'tight', set(gca, 'YDir', 'normal');
xlabel('x, m'); ylabel('z, m');
title(strcat('FDTD Simulation: Electric field at t=',string),
'FontSize', 16);
subplot(2,2,2)
plot(t*1e9, VG, 'b', t(1:n)*1e9, VLoad(1:n)*1e3, 'r'); grid on;
title ('Received voltage (red, mV) vs. TX voltage (blue, V)',
'FontSize', 16);
xlabel('time, ns');
subplot(2,2,4)
plot(t*1e9, VG, 'b', t(1:n)*1e9, VLoad(1:n)*1e3, 'r'); grid on;
title ('Received voltage (red, mV) vs. TX voltage (blue, V)',
'FontSize', 16);
xlabel('time, ns');
drawnow;
%-----
end
toc

```